University of Alberta

Transverse Cracking of $[\pm\theta/90_3]_s$ Composite Laminates

by

James W. Hoover

A thesis submitted to the Faculty of Graduate Studies and Research in partial fulfillment of the requirements for the degree of Master of Science

Department of Mechanical Engineering

Edmonton, Alberta

Spring 1999

National Library of Canada
Acquisitions and Bibliographic Services
395 Wellington Street
Ottawa ON K1A 0N4
Canada

Bibliothèque nationale du Canada
Acquisitions et services bibliographiques
395, rue Wellington
Ottawa ON K1A 0N4
Canada

Your file Votre référence

Our file Notre référence

The author has granted a non-exclusive licence allowing the National Library of Canada to reproduce, loan, distribute or sell copies of this thesis in microform, paper or electronic formats.

L'auteur a accordé une licence non exclusive permettant à la Bibliothèque nationale du Canada de reproduire, prêter, distribuer ou vendre des copies de cette thèse sous la forme de microfiche/film, de reproduction sur papier ou sur format électronique.

The author retains ownership of the copyright in this thesis. Neither the thesis nor substantial extracts from it may be printed or otherwise reproduced without the author's permission.

L'auteur conserve la propriété du droit d'auteur qui protège cette thèse. Ni la thèse ni des extraits substantiels de celle-ci ne doivent être imprimés ou autrement reproduits sans son autorisation.

0-612-40060-3

Canada

University of Alberta

Library Release Form

Name of Author: Jamieson Wesley Hoover

Title of Thesis: Transverse Cracking of $[\pm\theta/90_3]_s$ Composite Laminates

Degree: Master of Science

Year this Degree Granted: 1999

Permission is hereby granted to the University of Alberta Library to reproduce single copies of this thesis and lend or sell such copies for private, scholarly, or scientific research purposes only.

The author reserves all other publication and other rights in association with the copyright in the thesis, and except as hereinbefore provided, neither the thesis nor any substantial portion thereof may be printed or otherwise reproduced in any material form whatever without the author's prior written permission.

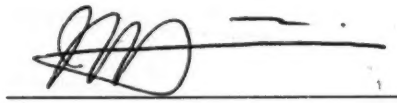

10968 73 Ave
Edmonton, AB
T6G 0C2
Canada

April 1, 1999

"You don't suppose, do you, that this discussion is degenerating into merely whisky-talk?"

"Very likely. But before we sink below the surface, let me tell you what twenty years of the cloth, as you so old-fashionedly put it, have taught me. Intellectual endowment is a factor in a man's fate, and so is character, and so is industry, and so is courage, but they can all go down the drain without another factor that nobody likes to admit, and that's sheer, bald headed Luck"

"I would have expected you to say God's Saving Grace."

"Certainly you can call it that if you like, and the way He sprinkles it around is beyond all human comprehension. God's a rum old joker, Clem, and we must never forget it."

"He's treated us well, wouldn't you say Simon? Here's to the Rum Old Joker!"

"The Rum Old Joker! And long may he smile on us."

Robertson Davies, <u>The Rebel Angels</u>

University of Alberta

Faculty of Graduate Studies and Research

The undersigned certify that they have read, and recommended to the Faculty of Graduate Studies and Research for acceptance, a thesis entitled Transverse Cracking of $[\pm\theta/90_3]_S$ Composite Laminates submitted by Jamieson Wesley Hoover in partial fulfillment of the requirements for the degree of Master of Science

F. Ellyin

Z. Xia

W. Chen

March 1, 1999

ABSTRACT

The foundations of every successful design are based on the understanding of failure mechanisms. The focus of this study was to develop an understanding of failure mechanisms associated with matrix cracking to improve the general design approach for composite materials. This thesis outlines how specimens were created from commercially available fully pre-impregnated E-glass advanced composite material. Experimental testing established stress-strain, matrix crack accumulation and stiffness reduction relations of $[\pm\theta/90_3]_S$ (θ =0°, 20°, 45°, and 55°) coupon specimens which were modelled using four methods of stress analysis and two distinct failure criteria. Internal variable stress analyses were inferior to elasticity approaches. Fracture mechanics failure criteria were superior to strength of materials criteria. A hybrid model, combining a shear lag approach and an approximate elasticity solution, was formulated and adequately predicted the stress-strain response, stiffness reduction and damage progression entirely from the fundamental material constants.

Table of Contents

1. Introduction 1
    1.1 Previous work on composite laminate matrix cracking 2
    1.2 Overview of the current study 4

2. Specimen Fabrication and Measurement of Engineering Constants 5
    2.1 Constituents of fibre composites 6
    2.2 Geometry of laminates 7
    2.3 Fabrication process 8
    2.4 Elastic properties 9
    2.5 Determining the specific fracture energy 11
    2.6 Shear modulus determination 12
    2.7 Engineering properties 13
    2.8 Residual stresses and strains 14
    2.9 Figures - Chapter 2 16

3. Experimental Mechanical Response and Transverse Crack Data 21
    3.1 Stress - strain response 22
        3.1.1 Lay-up effects 23
        3.1.2 Strain rate effects 24
    3.2 Damage detection 24
        3.2.1 Matrix crack observation techniques 25
        3.2.2 Computer-based image processor crack detection 26
        3.2.3 Transverse cracks vs. strain 28
        3.2.4 Transverse crack accumulation and stress vs. strain 30
    3.3 Stiffness reduction of cracked composite laminates 30
    3.4 Observations regarding constraining ply damage 32
    3.5 Figures - Chapter 3 34

4. Stress Analysis of Cracked Symmetric Laminates 45
    4.1 Literature review 46
        4.1.1 Internal variable stress analysis 46
        4.1.2 Shear lag stress analysis 48
        4.1.3 Elastic element stress analysis 48
        4.1.1 Variational elasticity stress analysis 49
        4.1.5 Limit of analysis 49

4.2 Basic equations of stress analysis 50
4.2.1 Classical laminate theory 50
4.2.1.1 Basic relations of classical laminate theory 51
4.2.1.2. Ply discount theory 53
4.2.2 Damage mechanics approach of Talreja 53
4.2.3 A shear lag approach to progressive cracking 56
4.2.3.1 Determining the shear lag parameter, ξ 59
4.2.3.1 Stiffness reduction 60
4.2.4 The elastic element theory of Nuismer/Tan 61
4.3 Predictions stiffness reduction 64
4.4 Figures - Chapter 4 68

5. Progressive Damage and the Implementation of a Failure Criterion 73
5.1 Background 75
5.1.1 Strength of materials failure criteria 75
5.1.2 Fracture mechanics failure criteria 78
5.2 Classical laminate theory and ply discount theory 81
5.3 Crack progression calculated from shear lag theory 82
5.4 Crack progression calculated from the elastic element model of Nuismer/Tan 87
5.4.1 Progressive damage predictions 89
5.4.1.1 First ply failure strains 89
5.4.1.2 Progressive failure 90
5.5 Stress-strain relation predictions 91
5.6 Comparing shear lag and Nuismer/Tan model predictions 94
5.7 Figures - Chapter 5 96

6. Conclusions 111

7. Bibliography 118

Appendix : Shear modulii determination using standard notched beam method 123

List of Tables

Table 2.1: Engineering constants for Scotchply 1003 GFRP prepreg 10
Table 2.2: Measured critical stress intensity factors 12
Table 2.3: Engineering properties for Scotchply 1003 13
Table 3.1: Number of specimens tested for each lay-up and strain rate 21
Table 5.1: Calculated first ply failure strains from CLT 77
Table 5.2: Calculated first ply failure strains from elastic element model 90

List of Figures

Figure 2.1 Laminae are cut from prepreg roll in any orientation 16
Figure 2.2 Laminae are hand cut from prepreg roll 16
Figure 2.3 Hand-lay-up of composite laminate 17
Figure 2.4 Laminate is placed in mould 17
Figure 2.5 Schematic of curing mould 18
Figure 2.6 Curing mould is placed in oven 18
Figure 2.7 Dimensions of compact tension (CT) specimens 19
Figure 2.8 Residual stresses in laminate plies due to temperature drop after curing 19
Figure 2.9 Residual strains in laminate plies due to temperature drop after curing 20

Figure 3.1 Stress-strain response for all specimens 34
Figure 3.2 Stress-strain response for $[0_2/90_3]_S$ specimens 34
Figure 3.3 Stress-strain response for $[\pm 20/90_3]_S$ specimens 35
Figure 3.4 Stress-strain response for $[\pm 45/90_3]_S$ specimens 35
Figure 3.5 Stress-strain response for $[\pm 55/90_3]_S$ specimens 36
Figure 3.6 Schematic of image processor 37
Figure 3.7 Image processor crack counting technique 38
Figure 3.8 Transverse crack accumulation in $[0_2/90_3]_S$ specimens 39
Figure 3.9 Transverse crack accumulation in $[\pm 20/90_3]_S$ specimens 39
Figure 3.10 Transverse crack accumulation in $[\pm 45/90_3]_S$ specimens 40
Figure 3.11 Transverse crack accumulation in $[\pm 55/90_3]_S$ specimens 40
Figure 3.12 Applied stress and transverse crack accumulation in $[0_2/90_3]_S$ specimens 41
Figure 3.13 Applied stress and transverse crack accumulation in $[\pm 20/90_3]_S$ specimens 41
Figure 3.14 Applied stress and transverse crack accumulation in $[\pm 45/90_3]_S$ specimens 42
Figure 3.15 Applied stress and transverse crack accumulation in $[\pm 55/90_3]_S$ specimens 42
Figure 3.16 Measured stiffness loss in $[0_2/90_3]_S$ specimens 43
Figure 3.17 Measured stiffness loss in $[\pm 45/90_3]_S$ specimens 43
Figure 3.18 Penetrant enhanced front view of constraining ply damage in all specimens 44

Figure 3.18 Penetrant enhanced side view of ply damage 44

Figure 4.1 A solid containing two sets of oriented crack arrays 68
Figure 4.2 A cross-ply laminate with cracks in the transverse plies 68
Figure 4.3 Symmetric cross-ply laminate under axial load 69
Figure 4.4 Stresses on individual layers of the laminate 69
Figure 4.5 Two adjacent transverse cracks in the 90 degree plies 69
Figure 4.6 Composite laminate containing a cracked ply and subject to in-plane loading 70
Figure 4.7 One quarter of the composite laminate unit cell 70
Figure 4.8 Stiffness reduction of two $[0_2/90_3]_S$ specimens tested at 10^{-4} s^{-1} strain rate plotted with internal variable models 71
Figure 4.9 Stiffness reduction of a $[\pm 45/90_3]_S$ specimens tested at 10^{-4} s^{-1} strain rate plotted with internal variable models 71
Figure 4.10 Stiffness reduction of $[0_2/90_3]_S$ specimens tested at 10^{-4} s^{-1} strain rate plotted with shear lag and elastic element models 72
Figure 4.11 Stiffness reduction of a $[\pm 45/90_3]_S$ specimen tested at 10^{-4} s^{-1} strain rate plotted with shear lag and elastic element models 72

Figure 5.1 SEM image of a transverse matrix crack in composite laminate 96
Figure 5.2 Steps involved in modelling progressive failure in composite laminates 96
Figure 5.3 Classical laminate/ply discount theory prediction of $[0_2/90_3]_S$ 97
Figure 5.4 Classical laminate/ply discount theory prediction of $[\pm 20/90_3]_S$ stress-strain curve 97
Figure 5.5 Classical laminate/ply discount theory prediction of $[\pm 45/90_3]_S$ stress-strain curve 98
Figure 5.6 Classical laminate/ply discount theory prediction of $[\pm 55/90_3]_S$ stress-strain curve 98
Figure 5.7 Two adjacent transverse cracks in the 90degree plies 99
Figure 5.8 Accumulation of transverse cracks as a function of the applied stress in $[0_2/90_3]_S$ specimens showing shear lag prediction 99
Figure 5.9 Accumulation of transverse cracks as a function of the applied stress in $[\pm 20/90_3]_S$ specimens showing shear lag prediction 100
Figure 5.10 Accumulation of transverse cracks as a function of the applied stress in $[\pm 45/90_3]_S$ specimens showing shear lag prediction 100
Figure 5.11 Accumulation of transverse cracks as a function of the applied stress in $[\pm 55/90_3]_S$ specimens showing shear lag prediction. 101

Figure 5.12 Accumulation of transverse cracks as a function of the applied strain in $[0_2/90_3]_S$ specimens showing Nuismer/Tan prediction. 101
Figure 5.13 Accumulation of transverse cracks as a function of the applied strain in $[\pm 20/90_3]_S$ specimens showing Nuismer/Tan prediction 102
Figure 5.14 Accumulation of transverse cracks as a function of the applied strain in $[\pm 45/90_3]_S$ specimens showing Nuismer/Tan prediction 102
Figure 5.15 Accumulation of transverse cracks as a function of the applied strain in $[\pm 55/90_3]_S$ specimens showing Nuismer/Tan prediction 103
Figure 5.16 Schematic of Nuismer/Tan method to predict crack progression 103
Figure 5.17 Stress-strain curve of $[0_2/90_3]_S$ specimens showing shear lag and Nuismer/Tan prediction 104
Figure 5.18 Stress-strain curve of $[\pm 20/90_3]_S$ specimens showing shear lag and Nuismer/Tan prediction 104
Figure 5.19 Stress-strain curve of $[\pm 45/90_3]_S$ specimens showing shear lag and Nuismer/Tan prediction 105
Figure 5.20 Stress-strain curve of $[\pm 55/90_3]_S$ specimens showing shear lag and Nuismer/Tan prediction 105
Figure 5.21 Schematic of Nuismer/Tan method to predict stress-strain curves 106
Figure 5.22 Schematic showing the experimental data and theoretical model regimes 106
Figure 5.23 Accumulation of transverse cracks as a function of the applied stress in $[0_2/90_3]_S$ specimens showing Case 3 shear lag and Nuismer/Tan prediction 107
Figure 5.24 Accumulation of transverse cracks as a function of the applied stress in $[\pm 20/90_3]_S$ specimens showing Case 3 shear lag and Nuismer/Tan prediction 107
Figure 5.25 Accumulation of transverse cracks as a function of the applied stress in $[\pm 45/90_3]_S$ specimens showing Case 3 shear lag and Nuismer/Tan prediction 108
Figure 5.26 Accumulation of transverse cracks as a function of the applied stress in $[\pm 55/90_3]_S$ specimens showing Case 3 shear lag and Nuismer/Tan prediction 108
Figure 5.27 Accumulation of transverse cracks as a function of the applied strain in $[0_2/90_3]_S$ specimens showing Case 3 shear lag and Nuismer/Tan prediction 109
Figure 5.28 Accumulation of transverse cracks as a function of the applied strain in $[\pm 20/90_3]_S$ specimens showing Case 3 shear lag and Nuismer/Tan prediction 109

Figure 5.29 Accumulation of transverse cracks as a function of the applied strain in $[\pm 45/90_3]_S$ specimens showing Case 3 shear lag and Nuismer/Tan prediction 110
Figure 5.30 Accumulation of transverse cracks as a function of the applied strain in $[\pm 55/90_3]_S$ specimen and Nuismer/Tan prediction 110

1. INTRODUCTION

In our civilization, centuries of engineering expertise have led to well-designed and well-constructed components. Most people do not worry about the integrity of a bridge they drive across everyday or fret over a pipeline explosion near their home. Inherent in our society is the assumption that the professionals who build crucial infrastructure and devices have accounted for every compromising situation.

In most cases, safety factors have been used to ensure safe operation. These factors account for many types of unforeseeable situations: fatigue, corrosion, stress concentrations, or changes in external loads. In some cases, safety factors of 6 are used depending on the uncertainty of loading, material strength, consequences of failure and the cost of safety [1].

This method of design argues that safety risks outweigh financial concerns and over the last century has resulted in unimaginable economic costs. However, as our civilization enters the twenty-first century, new materials and new technologies are improving design practices. Emerging technologies, like those that have led to composite materials, smart materials, microelectronic mechanical systems, and optical fibre sensors, have the potential to radically affect the spectrum of products that society consumes. In the same way that the appearance of plastic in the twentieth century revolutionized the world by replacing wood, mortar, natural fibre, aluminum, rubber and other light structural materials, polymeric composites with fibre reinforcement have the potential to replace steel, concrete and other metals in critical applications.

In general, the progress in stress and failure analysis techniques for advanced composites has been exceeded by improvements in manufacturing techniques. At this time, the manufacturing industry produces a multitude of polymeric fibre composites in various forms, but optimal use of composite materials is being hindered by a lack of effective analysis methods. This thesis aims to partially rectify this problem.

1.1 PREVIOUS WORK ON COMPOSITE LAMINATE MATRIX CRACKING

Aerospace industries, possessing high performance requirements and large budgets, have been a major user of carbon fibre products and much of the early research in advanced composites was done by aerospace designers for aerospace purposes. In the early 1990's, the aerospace/aircraft industry was the largest user of advanced composites. Design practices, including the "black aluminum" approach in which composite parts were substituted for aluminum parts without any design modifications, were largely driven by performance considerations (i.e. weight reduction and fuel efficiency) and not by economic or life-cycle costs [2].

In the case of aerospace/aircraft design, stiffness loss and catastrophic failure are the crucial failure considerations. Matrix cracking may be tolerable if the overall stiffness reduction is small and the mechanical design requirements are still met. A literature review reveals that researchers associated with aerospace companies wrote approximately half of the papers published in the 1970's and 1980's. Many of these papers presented exclusively carbon fibre experimental data. High performance products fabricated from carbon fibre-based materials have excellent stiffness, high strength, and low mass but high cost excludes them from many industrial applications.

Two decades later, other industries are evaluating advanced composite designs and hoping to exploit the superior corrosion and fatigue resistance of fibre reinforced composites. Public infrastructure is being reinforced with carbon and aramid fibre cables [3], bridge decks have been constructed from glass reinforced polyester [4], automotive body panels have been made by injection moulding commercially available fibre mats [5], and low to intermediate pressure tubing has been successful in corrosive petrochemical applications [6].

Industries in competitive civilian economies have many different design requirements than aerospace applications. In particular, the marketplace requires that

economic considerations far outweigh performance considerations. Corrosion, fatigue, pressure containment and life-cycle costs are the important design parameters dictating the functionality of a design, not stiffness loss or ultimate failure.

These new design requirements have led to the use of functional failure, defined as the point at which the design may not fulfill its original function, as the design limit. Functional failure may occur well before the structural integrity of the design is compromised. Two examples are loss of fluid in a pressure containment structure or unacceptable displacements.

A major goal of the Advanced Composite Materials Engineering team at the University of Alberta is to design and develop a high-pressure composite pipe. The key damage considerations are progressive crack damage, fluid containment, structural integrity, and long-term usage. In fact, concurrent work is showing that weepage due to matrix cracking, not loss of structural integrity or stiffness loss, is the dominant failure mode [7]. To address weepage failure, the current scope of knowledge must be expanded to include progressive crack damage. No longer can overall laminate behaviour, stiffness loss and ultimate failure be investigated while the growth and development of cracks is ignored. Progress must be made in predicting cracking in first monotonic, then fatigue, loading situations so that glass fibre composites are available for use in petrochemical, automotive, medical and microelectronic applications.

In the case of glass fibre composites, the body of research produced with aerospace considerations foremost in mind is largely irrelevant to the present discussion as structural integrity is not a key performance criterion. The task at hand remains to investigate and understand the mechanisms involved with functional failure of high-pressure containment components, in this case, progressive matrix cracking.

1.2 OVERVIEW OF THE CURRENT STUDY

The focus of the current study was to develop an understanding of the failure mechanisms that lead to matrix cracking in order to contribute to the advanced composite design methodology. This thesis outlines how specimens were fabricated from commercially available continuous E-glass 'prepreg' sheets and how the material properties were determined from experiment (Chapter 2). The complete set of material properties was measured in the current work to evaluate existing analytical models and to provide a full reference for future work. Experimental tests to investigate stress-strain, matrix cracking, and stiffness reduction behaviour were performed on coupon specimens (Chapter 3). The stress-strain relations were bilinear curves with knee-points corresponding to the onset of matrix cracking. The number of matrix cracks increased as the applied strain increased and no saturation crack density was reached. The mechanical performance of the composite was modelled using four methods of stress analysis (Chapter 4) and two distinct failure criteria (Chapter 5). A hybrid model combining a shear lag approach, an approximate elasticity solution, and a fracture mechanics failure criterion was able to correctly predict the stress-strain response, stiffness reduction and damage progression entirely from the fundamental material constants reported in Chapter 2.

2. SPECIMEN FABRICATION AND MEASUREMENT OF ENGINEERING CONSTANTS

One aspect of composite material studies that cannot be overemphasized is material variation. Unlike metals and other common engineering materials, advanced composites are often only partially cured by the manufacturer. In the case of academic research, final material processing takes place with the end user, typically in small laboratories scattered around the globe. Variations in the curing process within and between labs lead to variations in material performance. This chapter describes specimen preparation and details the tests to determine the engineering constants.

Curing factors, such as applied pressure, temperature, duration of cure, fibre fraction ratio, quality of workmanship, and care of handling have an effect on the final properties. The presence of small defects (matrix voids, fibre/matrix debonding, and microcracking) induced during contaminated lay-up or faulty curing can change the global behaviour of the material. Even for high quality specimens, poor machining degrades performance. In order to make valid conclusions regarding the material behaviour, specimens within and between batches must give reproducible results.

Elastic modulii, Poisson ratios, energy release rates and coefficients of thermal expansion are also affected by specimen fabrication and thus vary between laboratories. This is a difficulty for researchers attempting to apply theoretical models to experimental data because they seldom have access to the complete set of engineering constants. In particular, out-of-plane shear modulii are rarely reported with experimental results because relatively expensive and difficult tests must be performed with a specialized testing apparatus. The out-of-plane shear modulus G_{23}, for example, is rarely measured because it must be determined from a thick laminates (often ~20 mm, see Section 2.6) tested in shear.

In order to fulfil the requirements of their models, some researchers use either assumed laminate properties or properties from several references. The success or failure of

these models cannot be evaluated effectively if the accuracy of the input parameters is questionable.

In order to make this current work comprehensive and to allow future users to evaluate their models correctly, care has been taken to eliminate material variation between specimens. The author is confident that high quality specimens have been produced and that scatter has been minimized. In all cases investigated, specimen performance exhibited low scatter and no data that could be termed 'outliers' were observed.

The author also acknowledges that a complete set of experimental data must be accompanied by a complete set of material constants that characterize the material, curing process, and machining techniques used in fabrication of specimens. All elastic constants reported here have been measured and the test methods will be described. Included in this set of constants are the out-of-plane shear modulii using the ASTM Standard and the specific fracture energy of compact tension specimens.

2.1 CONSTITUENTS OF FIBRE COMPOSITES

All of the data in this study were taken from tests done on 3M Scotchply type 1003 continuous E-glass prepreg. The prepreg consisted of unidirectional E-glass (aluminoborosilicate fibreglass) fibres and partially cured epoxy matrix supported by paper backing. Particulars of the matrix, including resin and sizing chemistry, are proprietary. The first reported studies on this type of material were in the 1970's [8-14].

The prepreg was shipped to the Department of Mechanical Engineering at the University of Alberta in rolls approximately 50m in length and 0.35 m in width. The rolls were stored in a freezer to prevent premature curing of the matrix. The thickness of a ply when cured was about 0.2 mm.

The 3M material data sheet provided some information regarding material properties [15]. Ultimate strengths, stiffness modulii, thermal expansion coefficients, conductivity, and fibre fraction were reported for the recommended curing procedure.

2.2 GEOMETRY OF LAMINATES

The most common applications of advanced composites in prepreg form are the fabrication of multidirectional laminates in either flat plates [8-14, 16-21] or tubes [22]. These multidirectional laminates can then be tailored to have superior directional properties in response to anticipated applied loads. Laminate plates were formed by stacking and consolidating multiple plies (laminae). Each prepreg lamina was 152 mm x 203 mm but the angle of the fibres within this ply could be changed depending on how the lamina was cut from the prepreg (Fig. 2.1).

The description of a flat plate laminate structure is determined by the material and loading directions. In continuum mechanics, the principle material directions are 1, 2, and 3. For continuous fibre composites, the 1 direction corresponds to the fibre axis, the 2 direction to the in-plane transverse to fibre axis, and the 3 direction refers to the out-of-plane axis. The angle between the fibre direction and the applied uniaxial load in a coupon specimen determines the orientation of the ply. A 0° ply is oriented with the fibre in the loading direction and a 90° ply is oriented with the fibres perpendicular to the loading direction. A laminate description of $[0/90/90/0]_T$ is a four-layer crossply specimen with external 0° plies and internal 90° plies (transverse plies). A subscript T implies that the total laminate description is provided and a subscript S implies that the laminate is symmetric about the centerline. A numeric subscript following an angle refers to a multiple number of plies. For example $[0/90]_S$, $[0/90_2/0]_T$, and $[0/90/90/0]_T$ describe the same laminate. In most cases, researchers using coupon specimens denote the loading direction as x, the transverse to loading direction as y, and the out-of-plane direction as z.

Several laminates were used for this study. Specimens of the type $[\pm\theta/90_3]s$ were fabricated to determine the stress-strain response and transverse cracking behaviour. The $\pm\theta$ layers, known as the constraining plies, were made with θ=0°, 20°, 45°, 55° and 70°. $[90_{12}]_T$ plates were made into compact tension specimens for fracture testing and $[(0/90)_4]s$ and $[0_{70}]_T$ specimens were used to measure shear modulii. The thickness of the 70-layer specimen was 16mm. In order to make this specimen, a new mould had to be designed and constructed which explains the scarcity of out-of-plane shear test data.

2.3 FABRICATION PROCESS

The production of good quality specimens is crucial to obtaining reproducible experimental results and significant effort was invested in developing a fabrication process that was tightly controlled. The recommendations of the manufacturer were followed whenever possible.

Specimens were prepared from a roll of paper-backed prepreg tape. Fabrication of the coupon specimens started by cutting 152 mm x 203 mm (6"x8") rectangles from the prepreg roll. These rectangles could be cut so that the fibres had any orientation (Fig. 2.2). Once all the necessary laminae were cut from the roll, each lamina was carefully aligned and stacked. The first layer was placed in the curing mould with the exposed prepreg up and the paper backing down. Subsequent layers were placed on top of this layer with the exposed prepreg face down. Hand pressure was applied to the paper backing of this lamina to remove trapped air pockets and ensure uniform contact. After the hand pressure had been applied, the paper backing was removed (Fig. 2.3). This was repeated for each lamina until the laminate was completed.

Once the stacking and pressing process was completed, the uncured laminate was removed from the mould and placed in a vacuum chamber. The laminate remained in the vacuum chamber for 24 hours during which time any remaining air pockets trapped in the laminate were drawn out.

A curing mould was used to provide pressure and to contain the laminate during the cure (Fig. 2.4). The mould was constructed from steel and pressure was applied via an aluminum bladder. Support was provided to the uncured laminate by the mould base and a steel plate. On top of the laminate, another steel plate provided even distribution of the pressure applied by the bladder. Release film surrounded the laminate above and below to prevent it from bonding to the steel plates (Fig. 2.5). All steel members of the mould were treated periodically with mould release spray to prevent epoxy/steel bonding.

After 24 hours in the vacuum chamber, the uncured laminate was returned to the mould and an air pressure line was connected (Fig. 2.6). The laminate was then cured for 12 hours in a curing oven with the bladder pressure set to 25 psi and the temperature maintained at 150 °C (300°F). This time period and curing temperature were suggested by the manufacturer to allow for full polymer crosslinking. After the curing cycle, the mould was allowed to cool down to room temperature and the laminate was removed in the form of a 152 mm x 203 mm plate.

Test specimens approximately one inch wide were cut from the plate with a low-feed rate diamond blade saw. The feed rate was controlled by a hanging mass that exerted a constant force on the cutting blade. This force was approximately 10 Newton. A light cutting oil coated the diamond blade for lubrication. This method produced edges without notches, fibre pullouts, or edge delaminations that negatively affect material performance [20, 23-24].

2.4 ELASTIC PROPERTIES

Table 2.1 shows the variation in reported material properties for Scotchply 1003 prepreg. One can see that the values have a wide range and not all values have been measured for each test set.

Source	*Fibre Fraction (%)*	*Average Thickness (mm)*	E_1 *(GPa)*	E_2 *(GPa)*	G_{12} *(GPa)*	G_{23} *(GPa)*	ν_{12}	ν_{23}
current study	53	0.210	43.2	10.0	4.49	4.17	0.31	0.44
Scotchply [15]	46.8		39.3	9.7	3.1		0.254	
Hahn and Tsai† [8]	45.0		38.6	8.27	4.14		0.26	
Chou *et al.*† [9]		0.254	39.3	9.65	3.6		0.285	
Highsmith and Reifsnider [19]		0.203	41.7	13.0	3.4	4.58	0.3	0.40
Parhizgar [16]	50		40.7/ 40.0	8.1/ 8.3	4.1/ 4.1		0.29/ 0.26	0.07/ 0.05

† *material was Scotchply 1002*

Table 2.1: Engineering constants for Scotchply 1003 GFRP prepreg.

The fibre volume fraction percentage was determined from burn-off tests. If the initial mass and initial volume of a composite sample are known and the mass of fibres present after the burn-off is measured, the fibre fraction percentage is

$$v_f = \frac{mass_{fiber}}{\rho_{fiber} \times volume_{total}}$$

where the fibre density is known for E-glass to be 2.55g/cm^3[25].

Elastic modulii were measured from unidirectional specimens. A $[0_{12}]_T$ coupon specimen was outfitted with strain gauges in the axial (loading) and off-axis directions. The specimen was loaded to 0.3% strain several times and the strains and loads were recorded. E_1 and ν_{12} were found to be 43.2 GPa and 0.31 respectively. E_2 and ν_{23} were measured from a unidirectional $[90_{70}]_T$ specimen. The specimen was loaded to 0.05% and 0.1% strain to measure the modulii. Unfortunately, this specimen geometry is very weak and failure

occurred during the third loading attempt at 0.13%. E_2 and ν_{23} were found to be 10.0 GPa and 0.44 respectively. The measurements of shear modulii are described in Section 2.6.

2.5 DETERMINING THE SPECIFIC FRACTURE ENERGY

Several analytical models use the specific fracture energy as a failure criterion. Tests were done on compact tension specimens at the University of Alberta advanced composite materials laboratory to determine this value.

Compact tension (CT) specimens were cut from laminates fabricated in the same manner as the coupon specimens. The $[90_{12}]_T$ CT specimens (Fig. 2.7) had initial dimensions of:

a_o=25.4 mm

W=50.8 mm

B=2.52 mm

The initial a_o/W ratio was 0.5. The machined crack length, a, was created by the diamond blade saw and was subsequently hand-sharpened with a razor blade. The CT specimens were tested in an Inston Testing Frame at a rate of 2.5mm/min. The load required for crack growth was recorded and the critical stress intensity was calculated from the non-dimensional K_I solution for through-thickness cracks in flat plates shown below [26].

$$f\left(\frac{a}{W}\right)=\frac{K_I B\sqrt{W}}{P_Q}=\frac{2+\frac{a}{W}}{\left(1-\frac{a}{W}\right)^{\frac{3}{2}}}\left[0.886+4.64\left(\frac{a}{W}\right)-13.32\left(\frac{a}{W}\right)^2+14.72\left(\frac{a}{W}\right)^3-5.60\left(\frac{a}{W}\right)^4\right]$$

CT Specimen	Initial crack length, a (mm)	Crack Extension Load, P_Q, (N)	Crack Length Ratio, a/W	Critical Stress Intensity Factor, K_{IC}, ($N/m^{3/2}$)
D	26	133.6	0.512	2.29×10^6
E	26.5	111.4	0.522	1.97×10^6
F	30	95.8	0.590	2.16×10^6

Table 2.2: Measured critical stress intensity factors.

From the measured critical stress intensity factors, the energy release rate and the specific fracture energy can be found. Assuming perfectly elastic behaviour:

$$G_C = \frac{K_{IC}^2}{E}$$

$$\gamma_f = \frac{G_C}{2} = \frac{K_{IC}^2}{2E}$$

Using the average stress intensity value, the specific fracture energy, γ_f, is:

$$\gamma_f = \frac{K_{IC}^2}{2E} = \frac{(2.141 \times 10^6 \frac{N}{m^{3/2}})^2}{2 \times 11.4 GPa} = 201 \frac{J}{m^2}$$

2.6 SHEAR MODULUS DETERMINATION

Several theories require the shear modulii to model the behaviour of the composite laminates. Although several values for Scotchply 1003 were available in published documents, these values ranged widely (Table 2.1) and were determined from specimens cured differently. To be confident when comparing models with experimental data, the shear modulii of the current specimens were measured using the ASTM Standard Iosipescu

test method [27]. The Iosipescu specimens were prepared using the same method as the coupon specimens.

A full description of the tests is contained in Appendix A. G_{12} was determined with $[(0/90)_4]_S$ crossply specimens to be 4.49 GPa. G_{23} was determined with $[0]_{90}$ unidirectional specimens to be 4.17 GPa. The standard was followed except for the specified notch size and cord modulus domain. These two deviations from the ASTM Standard are described fully in Appendix A.

2.7 ENGINEERING PROPERTIES

Engineering Constant	Value
Longitudinal Modulus, E_1	43.2 GPa
Transverse Modulus, E_2	10.0 GPa
In-plane Shear Modulus, G_{12}	4.49 GPa
Out-of-plane Shear Modulus, G_{23}	4.17 GPa
In-plane Poisson ratio, ν_{12}	0.31
Out-of-plane Poisson ratio, ν_{23}	0.44
Coefficient of linear expansion, α_1	8.6 x10^{-6} per °C
Coefficient of linear expansion, α_2	22.1 x10^{-6} per °C
Temperature drop from stress-free temperature, ΔT	-125 °C
Specific Fracture Energy, γ_f	201 J/m^2
Average Ply Thickness	0.210 mm
Fibre Fraction, v_f	52%

Table 2.3: Engineering properties for Scotchply 1003.

Table 2.3 presents the complete list of measured engineering properties. Elastic modulii and Poisson ratios were determined by measuring strain with bonded strain gauges during a monotonic load ramp. Shear modulii were measured using the Iosipescu standard [27], the specific fracture energy as described in Section 2.5, and the fibre fraction with burn-out tests (Section 2.4). The coefficients of linear thermal expansion were obtained from the material data sheet [15] and the temperature drop was obtained from the curing cycle.

2.8 RESIDUAL STRESSES AND STRAINS

Residual strains and stresses develop in composites due to temperature change and thermal expansion coefficient mismatch between the matrix and the fibre. If the matrix and fibres are stress free near the curing temperature (150 °C, 300°F), thermal stresses will result as the specimen is cooled to room temperature (20 °C, 70°F) after curing. It is important to calculate these stresses to determine how they may contribute to damage or failure of the laminate.

Classical Laminate Theory can be used to determine the residual stresses and strains in a laminate [28]. The procedure involves calculation of the free hygrothermal strains from the expansion coefficients, engineering constants, and the temperature change. The thermal forces are then calculated from the stiffness matrix of each layer. The reference plane strains and the hygrothermal strains in the loading directions are subsequently used to find the hygrothermal stresses in the material and loading directions. In this application, the residual stresses and strains are well within the elastic region which means CLT provides accurate values.

The residual stresses of a $[\pm\theta/90_3]_S$ laminate were calculated using Matlab program *CLT.m*. The engineering values, expansion coefficients and temperature drop of the experimental specimens was used. The results of the calculations are shown in Figs. 2.9-2.10 for the stresses and strains in the 2-direction. This 2-direction is most important because the matrix direction has the least strain to failure. Figure 2.9 shows how the hygrothermal stresses change as a function of θ. At θ=0°, the residual stresses are approximately 12 MPa in the constraining ply and 10.5 MPa in the transverse ply. The constraining ply stress remains constant until θ=20° before decreasing to 0 MPa at 90°. The transverse stress simply decreases to 0 MPa at 90°. It should be noted that the stresses in the matrix direction

are always positive which indicates that the matrix is experiencing a tensile load at room temperature.

The residual strains in the matrix direction are plotted in Figure 2.10 as a function of constraining angle θ. This figure closely resembles the residual stress behaviour (Fig. 2.9). Once again, CLT indicates that the matrix is in tension due to thermal effects. It will be shown in Chapter 3 (Section 3.2.3) that the residual thermal strains calculated by CLT are a significant portion of the strain required to initiate matrix cracking (Section 3.2.3).

2.9 FIGURES - CHAPTER 2

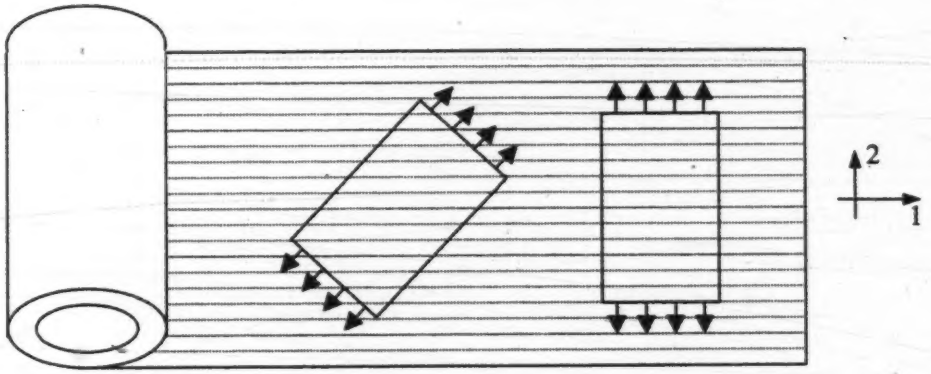

Figure 2.1 Laminae are cut from prepreg roll in any orientation.

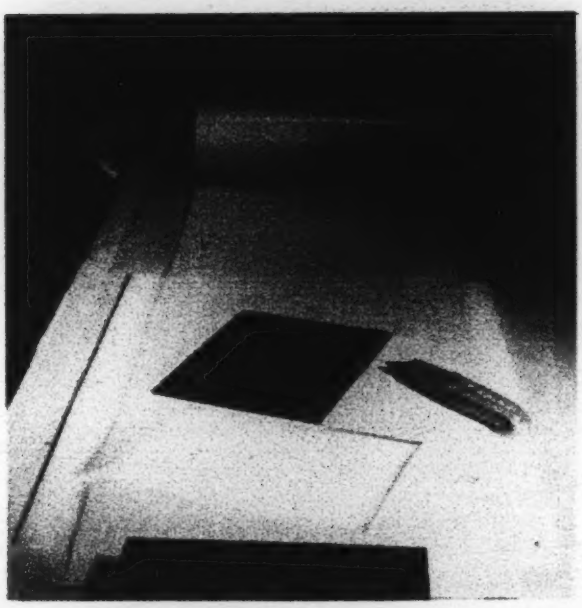

Figure 2.2 Laminae are hand cut from prepreg roll.

Figure 2.3 Hand lay-up of composite laminate. Here the paper backing is being removed from the top ply.

Figure 2.4 Laminate is placed in mould.

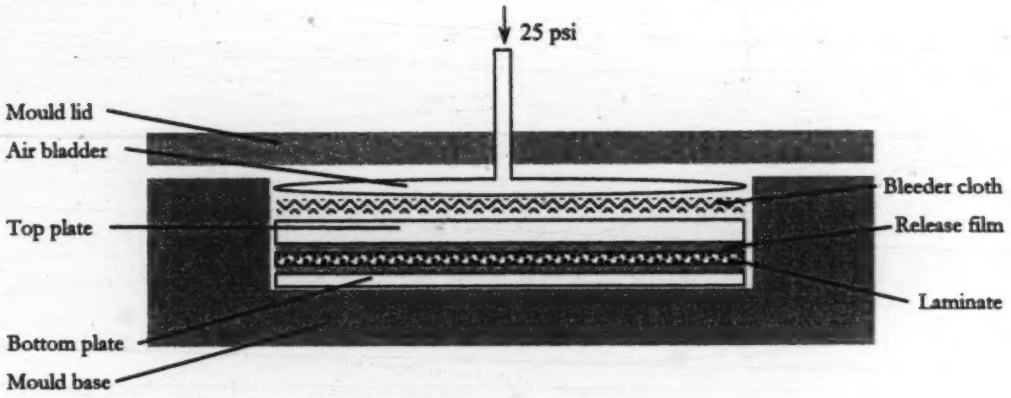

Figure 2.5 Schematic of curing mould.

Figure 2.6 Curing mould is placed in oven.

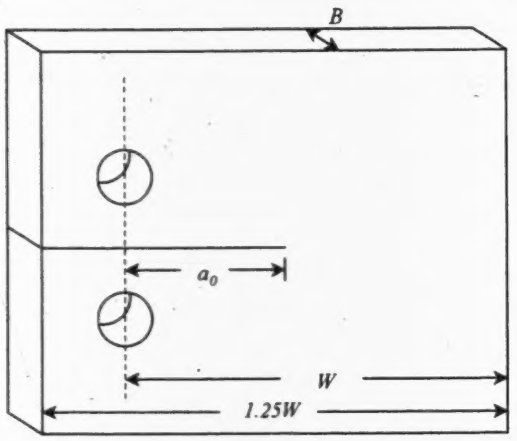

Figure 2.7 Dimensions of compact tension (CT) specimens.

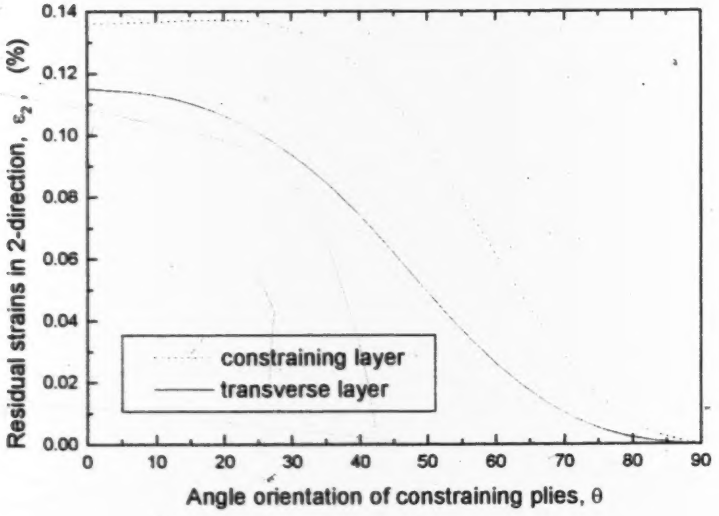

Figure 2.8 Residual stresses in laminate plies due to temperature drop after curing.

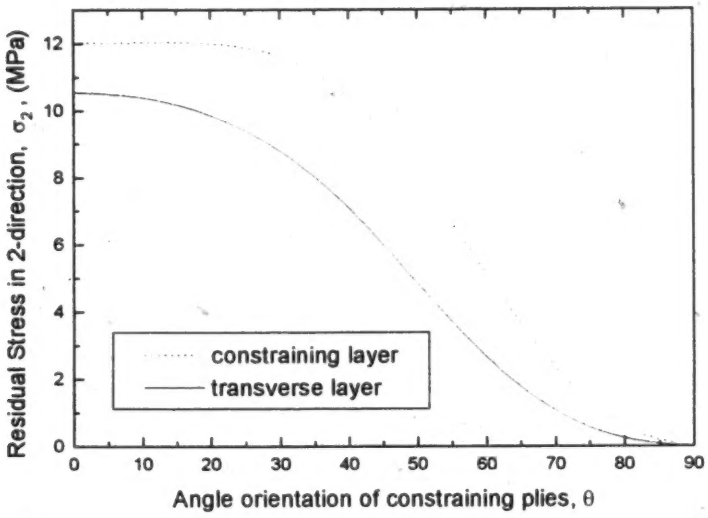

Figure 2.9 Residual strains in laminate plies due to temperature drop after curing.

3. EXPERIMENTAL MECHANICAL RESPONSE AND TRANSVERSE CRACK DATA

This study was conceived out of the need to understand the factors that influence material performance. It was intended to be an early step along the path to a general design approach. The focus included the stress-strain response, onset of cracking and delamination damage, ultimate failure stresses and thermal response of composite laminates.

For the purpose of this study, 26 coupon specimens were tested: six $[\pm\theta/90_3]_S$ specimens with θ=0°, 20°, 45°, 55° and two $[\pm70/90_3]_S$ specimens. Each $\pm\theta$ specimen set was tested to investigate rate effects at three monotonic strain rates: 10^{-4}, 10^{-5}, and 10^{-6} (except the $[\pm70/90_3]_S$ specimens that failed catastrophically after the initiation of one transverse crack, Table 3.1). In addition to those specimens shown below, $[0_2/90_3]_S$ and $[\pm45/90_3]_S$ specimens were tested to determine the stiffness reduction caused by matrix cracking.

Specimen Lay-up	Strain rate 10^{-4}	Strain rate 10^{-5}	Strain rate 10^{-6}
$[0_2/90_3]_S$	2	2	2
$[\pm20/90_3]_S$	2	2	2
$[\pm45/90_3]_S$	2	2	2
$[\pm55/90_3]_S$	2	2	2
$[\pm70/90_3]_S$		2	

Table 3.1: Number of specimens tested for each lay-up and strain rate.

The origins of this study were rooted in the effect of θ in $[\pm\theta/90_3]_S$ specimens. It was believed that changing θ from 0° to 45° would result in vastly increased failure strains. While this effect was not observed, the data in this chapter will show that the θ-ply orientation does affect the behaviour of the transverse 90° plies. It will also be shown that the onset of transverse cracking in the 90° plies leads to a 'knee' point in the stress strain curve, transverse cracking occurs until specimen failure, ultimate failure varies from 1.4% to

2.4%, and delamination only occurred at high strains. The effect of rate was negligible and cracking in the outer plies of the ±45° and ±55° specimens was observed.

3.1 STRESS-STRAIN RESPONSE

The stress-strain response is the most informative and universal information that can be provided for a material. It can be used as a basis for comparison or to indicate additional loads that may be applied. In the case of composite laminates, it indirectly provides information on the amount of damage in the specimen and how this may affect load carrying capacity in the future.

Tensile modulus measurements and unidirectional loading of coupon specimens were performed in strain control on coupon specimens. These specimens had dimensions of approximately 200 mm x 25 mm. Aluminum tabs (38 mm x 25 mm) were bonded to the specimen ends to prevent damage from the loading grips. Tests were computer controlled with load measured on a 10 kN load cell and strain measured with a 75 mm extensometer. An external PC collected load and strain data from the controller.

The stress-strain responses of all specimens (except the ±70° specimens) are shown in Figure 3.1. One can see that the scatter between specimens is very low and that lay-up, but not rate, affects the stress-strain response. Each data set in the figure will be discussed more thoroughly in the upcoming sections.

The definition of stress in composite materials is somewhat unclear because material inhomogeneity causes localized stress to vary within, and between, laminate plies. Local stresses are affected by fiber spacing irregularities and large stress gradients exist at the fiber and ply interfaces. The prevailing practice in composite laminate discussions is to define stress as the average applied stress, *i.e.* total applied load divided by total cross-sectional area. For the remainder of this thesis, any stress to be discussed will be the average applied stress.

One of the most striking effects seen in Figure 3.1 is the bilinearity of all the stress-strain curves. Each of the curves shows an initial elastic response up to approximately 0.6% strain. After this 'knee' in the curve, the responses are once again linear until failure. The stiffness losses are due to matrix cracking in the transverse plies which occurs at approximately 0.6% strain. Section 3.2 shows how the 'knee' point corresponds to first ply failure and Section 4.2 discusses analytical models that provide a theoretical explanation of this behaviour.

A comment must be made regarding the ultimate failure points. From Figure 3.1, it would appear that the ±45° specimens had the largest strain to failure by as much as 0.5%. Due to the method of data collection, this may be misleading. During the strain-controlled tests, strain was measured with an extensometer attached to the specimen. The response of the extensometer in the three-inch gauge length was known but the strain in the grips or outside the extensometer was impossible to measure. For this reason, and because the 0° and ±20° tests more often ended due to slippage in the tabs or grips, the apparent ultimate failure points shown in the Figure 3.1 may be misleading.

3.1.1 Lay-up Effects

The raw stress-strain data for each lay-up are shown in Figures 3.2-3.5 from the stiffest constraint (θ=0°) to the least stiff constraint (θ=55°). In each figure one can observe the bilinear response. Because the slope of the curve is related to the stiffness of the specimens, the 0° specimens exhibit a stiffness loss of approximately 20% while the stiffness of the ±55° specimens drops to zero. Transverse cracks (cracking within a ply) were observed after approximately 0.6% strain and increased in number until ultimate failure. Delaminations (cracking between plies) were only observed in the final moments of the test.

3.1.2 Strain Rate Effects

The effect of applied strain rate on the material response can be observed in Figure 3.1. The trends of the data suggest that as the strain rate is reduced, slightly lower stresses result. This is expected because the polymeric matrix has a viscoelastic (time-dependent) behaviour which results is some stress relaxation during the test.

The behaviour of glass fibres is almost perfectly elastic. One would expect that viscoelastic effects would be small for specimens with fibres oriented in the loading direction (fibre dominated 0° specimens) and large for specimens with fibres not oriented near the loading axis (matrix dominated ±45° and ±55° specimens). The effect of rate, however, is very slight. Even for the most matrix-dominated specimen, ±55°, the effect is barely discernable over the experimental scatter (Fig. 3.5).

3.2 DAMAGE DETECTION

One challenge facing engineers using composite materials is the multiple failure modes of composite laminates and composite materials in general. Damage can affect the fibres, the matrix, the interface or a combination of those. Damage can be microscopic in scale (fibre/matrix debonding, matrix microcracks) to macroscopic (matrix cracking, delamination, fibre failure).

Extensive research pursued the determination of ultimate strengths and strains. The earliest work on composite materials sought to find failure envelopes and analytical and empirical predictive models [8, 9]. These works studied the stiffness reduction of cracked crossply and quasi-isotropic laminates.

Early in the development of composite materials, aerospace design requirements defined specimen failure in terms of stiffness loss and ultimate strength [29-42]. Currently, more diverse industries are utilizing composite materials and the design requirements are changing. Therefore, the definition of failure may vary for each application. Aerospace designs may tolerate matrix cracking providing that the remaining stiffness is acceptable.

However, pressure containment may be compromised in the presence of matrix cracking. It is necessary to define functional failure as the state in which the design cannot perform its function.

One goal of the Advanced Composite Material Engineering team at the University of Alberta is to develop design criteria for high-pressure pipelines. In this case, failure to contain high-pressure gas is functional failure. This could result from a localized burst failure or fluid weepage via a network of cracks through the wall thickness. It has been shown from work done at the University of Alberta [22] that weepage is a failure mechanism. Since weepage results from cracking in the laminate, understanding crack initiation and accumulation is an important aspect of current research.

3.2.1 Matrix Crack Observation Techniques

Matrix cracking has been investigated for several years. The most influential work on the subject was done in 1982 by Highsmith and Reifsnider [19] who studied $[0_n/90_m]_s$ coupon specimens in uniaxial tension. The 90° layers in the specimen developed matrix cracks throughout the gauge length of the specimen. As the number of 90° layers increased, the average crack spacing increased and the cracks became more predominant. These through-thickness and through-width cracks were oriented parallel to the fibres and perpendicular to the applied load.

Several methods have been used to record the presence of matrix cracks. For E-glass materials, the composite is translucent which allows for visual observations. However, carbon fibre based materials are opaque which make through-thickness visual observations impossible. A variety of methods have been developed to record the initiation and accumulation of matrix cracks. These methods range from in-situ human observations [21], to edge examination [43], dye penetrant x-ray radiography [19, 41-42], and acoustic emission methods [29, 34].

These methods have two major limitations. The most crucial problem is verifying that the recorded cracks actually exist. In the case of edge examination, it has been shown that edge cracks may not propagate through the specimen width [43]. Acoustic emission methods record the sound of cracking and the location or type (transverse or delamination) of crack is difficult to determine.

The other limitation is time. Clearly, the unassisted human is limited in the accuracy and number of multiple measurements. A strain controlled test at a rate of $10^{-4}s^{-1}$ reaches 2% strain in 40 seconds. It would be difficult, if not impossible, to accurately record both the time and location of a new crack manually. Other methods also suffer from not recording cracks as they appear. Dye-penetrant methods require soaking time and thus cannot be used for monotonic testing. Ultrasonic and other scanning methods require scanning periods. If crack accumulation is rapid, one cannot determine the location, type and time of the appearance of a new crack with the methods listed above. To overcome human limitation and collect more essential data, a computer-based crack detection system was developed.

3.2.2 Computer-based Image Processor Crack Detection

Of particular interest to this study was transverse crack initiation and location during a monotonic strain controlled test. Determining crack initiation is an important factor in design because it reveals the onset of damage in some composite geometries. The location of each crack is also important because most theoretical models assume uniform spacing of transverse cracks.

A schematic of the PC-based image processor system is shown in Figure 3.6 (this system was developed at the University of Alberta by Dr. J.D. Wolodko). The cracked coupon specimen undergoing testing is shown in the upper center of the figure. A fluorescent light radiates through the specimen and is picked up by a video camera on the opposite side. The image of the specimen is backlit and the cracks appear as horizontal dark bands. The camera is placed so that only the specimen length between the extensometer

appears and the image is displayed on the PC monitor. The specimen is vertical in the testing frame but horizontal in the image to maximize the image area of the camera.

The image can then be captured and stored in a PC for future data processing. Application of an external trigger, either from a manual or automatic source, instructs the frame grabber inside the PC to capture the current image. The CPU directs the image to be saved in either extended memory or on disk. Once stored as an image file, the image can be processed any time in the future. This process is analogous to photographing and digitally imaging the specimen.

The next step is the processing of the stored images. To record the initiation and location of cracks, each image is individually examined. Cracks are found by noting the location of dark horizontal bands in the image. The procedure is shown in Figure 3.7. The original colour image, with the extensometer visible on the sides, is converted into a grayscale image. The grayscale image consists of each pixel having an intensity from 0-255, 0 being black and 255 being white. Thus, the image file now contains a light intensity value for each pixel in the image.

Two corners marked on the specimen during testing now define an observation area. Within this area, the grayscale intensities of vertical columns of pixels are summed and recorded. For uncracked areas, the grayscale intensity and corresponding summation is large. In cracked areas, the dark cracks cause a decrease in the grayscale intensity summation. The resulting summation is shown at the top of the figure.

To record cracks, cracked and uncracked (baseline) grayscale summations are compared. One will note that the baseline summation is not constant over the gauge length. This is due to uneven light intensity provided by the fluorescent source. The difference between the cracked and baseline summation is plotted as the subtracted waveform in the figure. If any point on the waveform drops below an adjustable threshold, the computer reports a crack at the corresponding pixel position. A plot of the observation area with

cracks can be reproduced on the screen and superimposed on the original image for verification. A data file records the cracks with their actual positions on the specimen. This automated procedure was verifred by comparing the number of cracks reported by the computer with visual crack counts performed during a slow strain rate test. Results from each test are examined to verify that the crack counts are accurate. The sensitivity of the threshold may be changed in response to intensity variations of the fluorescent light source.

This procedure will record transverse cracks for each image. Due to the vertical pixel column summation, it cannot count angle cracks. Each image is number catalogued which allows the stress-strain and damage state to be correlated. A challenge arises when determining crack initiation strain because a crack appearing between two sequential images may have occurred at any time during the time interval between images. By increasing the number of images, the time interval decreases and the crack initiation strain can be more accurately determined. Thus, accurately determining crack initiation strains is limited by the speed of which the computer can file images in memory. Initial tests included 17 images in 2% strain which gave a strain uncertainty of about 0.1% for the cracking state in each image. Future tests will be done with more images and the strain uncertainty will be decreased.

3.2.3 Transverse Cracks vs. Strain

In the current study, transverse cracks in the gauge length were recorded with the image-processor system for all specimens. The cracks were recorded over a gauge length of 70 mm. Images of the specimen were captured every 0.1% strain. Figures 3.8-3.11 show the number of transverse cracks increasing with the applied strain. In each figure, the data is confined to a narrow scatter band regardless of applied strain rate. In most specimens, the number of cracks are increasing until failure. This would indicate that crack saturation is not occurring and that crack saturation is not required to precede ultimate specimen failure. One can still argue the validity of the CDS (Characteristic Damage State) proposed by Highsmith and Reifsnider [19] by claiming that the ultimate failure strain is less than the CDS strain, but a CDS was not observed during this experimental study.

The onset of transverse cracking may be the most important finding of Figs. 3.8-3.11. Specimen-to-specimen variation makes it impossible to isolate a specific strain value for the appearance of the first crack, but it appears that the first cracks in the 0° and 20° specimens occur at 0.5% and the first cracks in the 45° and 55° occur at slightly higher strains. By 0.6%, almost all specimens have one transverse crack. This first ply failure strain will be used in the following chapter to model the stress-strain response using Classical Laminate Theory and the ply discount approach (Section 5.2).

Comparing Figures 3.8-3.11 show that the angle of constraining plies changes the accumulation of transverse cracks. The 0° and 20 ° specimens both show cracks appearing at 0.5% strain and accumulating rapidly. If superimposed, one would see that the cracking behaviour of both 0° and 20° specimens is very similar. For the matrix dominated specimens, crack initiation appears to be slightly delayed and the total number of cracks is less. The 45° results show a steady accumulation of cracks that decreases slightly after 1.5% strain. The 55° results definitely show delayed crack initiation and a reduced rate of accumulation. The maximum number of cracks is less for matrix dominated specimens: about 33 for 45° and 20 for 55°. The fibre dominated 0° specimens reach 40 cracks in the 70 mm gauge length.

One reason for the different crack behaviour of matrix and fibre dominated specimens is revealed in Figure 2.10. The figure shows that the interlamina residual thermal tensile strains in the transverse fibre direction are higher for fibre dominated specimens. For the 0° specimens, the residual tensile strain is 0.115% which is a significant portion of the 0.5% first crack strain. For the matrix dominated specimens, this residual tensile strain drops to 0.055% and 0.035% for the 45° and 55° specimens, respectively. One would expect that cracks would appear in fibre dominated specimens before matrix dominated specimens due to thermal residual strains. An explanation for the reduced crack accumulation in matrix dominated specimens is suggested in the next section.

3.2.4 Transverse Crack Accumulation and Stress vs. Strain

Earlier in this chapter it was suggested that matrix cracking caused a bilinear stress-strain response. One can see evidence of this if the average stress and the number of cracks are plotted against the applied strain in the same graph (Figs. 3.12-3.15). The plots contain the data from the test rate of $10^{-4}s^{-1}$. Only the data from one rate (two specimens) is shown so that the trends do not get lost in the scatter of too many specimens.

Figures 3.12-3.15 reveal that the knee in the stress-strain curve corresponds to the strain at which the first transverse crack appears (first ply failure strain). This is an important observation because it validates the theoretical approach that will be undertaken in the next chapter dealing with modelled laminate mechanical response. The figures contain two key observations:

1. The stress-strain response of a specimen is linear up until the appearance of the first transverse crack at approximately 0.6% strain. This will enable the use of elastic laminate analysis to accurately determine the thermal response of the laminate up until the point of crack damage. Classical Laminate Theory (Section 4.2.1) can be used to predict residual thermal stresses and the initial stiffnesses of multidirectional laminates.
2. Mechanical response is directly affected by transverse crack damage. The figures show that the stresses carried by the laminate and the number of cracks in the laminate are connected. It seems reasonable to develop models that associate the stress to the number of cracks. This approach is used in the shear lag and elastic element models described in Chapter 4.

3.3 STIFFNESS REDUCTION OF CRACKED COMPOSITE LAMINATES

Modelling progressive damage is a two step process combining a stress analysis with a failure criterion. A thorough experimental work would collect data to examine both steps

in this process. While it is straightforward to compare failure criteria with experimental data, collecting data regarding the stress analysis is more difficult.

It is impossible to quantitatively measure the stress state of composite laminates. No instruments or methods to determine microstructural stresses are available. Furthermore, the concept of stress used in this work is actually the average stress that does not represent the actual local values in the polymorphic composite structure.

In order to evaluate the models that predict the stress state, the stress analysis of the models is examined by comparing the predicted stiffness loss with the experimentally measured stiffness loss. The stiffness prediction of each model is available because most models develop constitutive equations in which the stress state is a function of crack spacing. Many models assume that strain or stress is uniform across the specimen thickness and calculation of the element stiffness is therefore quite simple.

Experimental measurements of the stiffness loss due to increased matrix cracking were completed on a pair of $[0_2/90_3]_S$ specimens and a single $[\pm 45/90_3]_S$ specimen. The specimens were loaded up to a predetermined strain and then unloaded to zero. The stiffness was determined by measuring the stress when the strain reached 0.3% during the loading ramp.

The testing procedure began with 3 monotonic ramps to 0.3% strain. During these three ramps the stiffness did not change. The specimens were then loaded to higher strains in increments of 0.05% until the first crack appeared. The stiffness of the specimen during the ramp that led to the first crack was used as the original stiffness value.

The stiffness was then measured as the number of cracks increased. Figure 3.16 shows the drop in stiffness of the $[0_2/90_3]_S$ specimens. The two specimens tested show small scatter and the curve is approximately linear. The maximum stiffness loss is 15% before specimen failure.

The response of the $[\pm 45/90_3]_S$ specimen is shown in Figure 3.17. In this case, the maximum stiffness loss is 45% of the original value and the curve is definitely non-linear. The stiffness loss of the ±45° specimens is larger because the contribution of the transverse plies to the overall laminate stiffness is greater as the constraining ply angle increases. The effect of cracking on the overall stiffness is greater as the stiffness of the constraining plies decreases. These stiffness reduction plots will be examined more thoroughly in Section 4.3 when they will be compared to model predictions.

3.4 OBSERVATIONS REGARDING CONSTRAINING PLY DAMAGE

When modelling the mechanical response of the laminates, the stress state is found by solving an elasticity problem based on elastic ply behaviour and transverse ply cracking. An assumption that simplifies this analysis greatly is that the constraining plies are perfectly elastic. For crossply specimens, this assumption is effective because 0° plies are dominated by the fibres oriented in the load direction. However, as the constraining angle increases from 0°, the fibres in the constraining plies depart from the loading axis and the effect of the matrix becomes more apparent. Therefore, the assumption that the constraining plies remain elastic may not be valid.

The effect of non-linearities in the constraining plies on model predictions will be shown in Chapter 4 and 5. Chapter 4 shows that stiffness loss is underestimated and Chapter 5 shows that crack accumulation is overpredicted in specimens with large (>20°) constraining ply angles. These problems arise because fracture mechanics models use either the stiffness or stress of cracked elements to calculate the elastic strain energy. This strain energy is then related to the energy release rate and the ability of the laminate to form a new crack. If the stiffness of the constraining plies is overestimated, the potential strain energy and corresponding number of cracks is overestimated. Constraining ply non-linearities can

explain the problems with the Chapter 4 and 5 predictions, but can the non-linearities actually be observed?

Once the tests were completed, an examination revealed that there is substantial damage in the constraining plies of large constraining ply angle specimens (Figure 3.18). Failed specimens were submerged in liquid penetrant for 12 hours and photographed with X-ray radiography. In addition to transverse cracks in the transverse plies, one can see that matrix cracking has also occurred in some constraining plies. For the 0° specimens, there are three cracks in the 0° plies that only developed during final failure. One can see that the cracks span several transverse cracks and do not seem to be associated with any particular crack. These cracks, situated along the loading axis, do not have a large affect on the stiffness of the 0° ply. The $[\pm 20/90_3]_S$ specimen in the figure shows no cracks in the constraining plies which conforms that transverse cracks do not damage the 0° and 20° constraining plies. As the angle of constraint increases, matrix cracks become more apparent. The $[\pm 45/90_3]_S$ specimens show several matrix cracks oriented at 45° to the applied load. In the case of the $[\pm 55/90_3]_S$ specimens, numerous constraining ply cracks were visible during the testing of the specimen cross the transverse crack. In addition, these constraining ply cracks are localized which indicates that transverse cracking may cause constraining ply cracks.

The effect of transverse cracking on the constraining plies can also be seen from the edge view of the specimens. Figure 3.19 shows a penetrant enhanced image of the $[0_2/90_3]_S$ and $[\pm 55/90_3]_S$ specimens. Two features are noticeable: the transverse crack density is greater and cracks are constrained more effectively in the $[0_2/90_3]_S$ specimen. In the case of the $[\pm 55/90_3]_S$ specimen, the crack density is lower but the transverse cracks seem to extend through the constraining plies to the surface of the specimen. Thus, the crack damage extends to the surface as was observed in Figure 3.18. The effect of these constraining ply cracks is to decrease the contribution of the constraining plies to the overall stiffness of the composite and introduces errors into the elasticity analysis.

3.5 FIGURES - CHAPTER 3

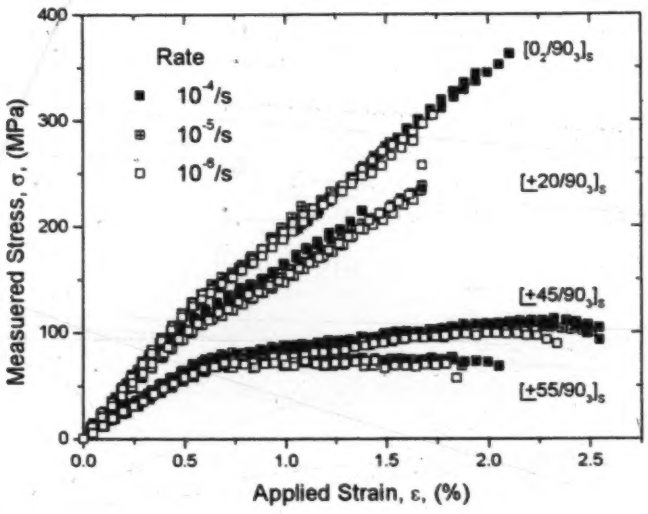

Figure 3.1 Stress-strain response for all specimens.

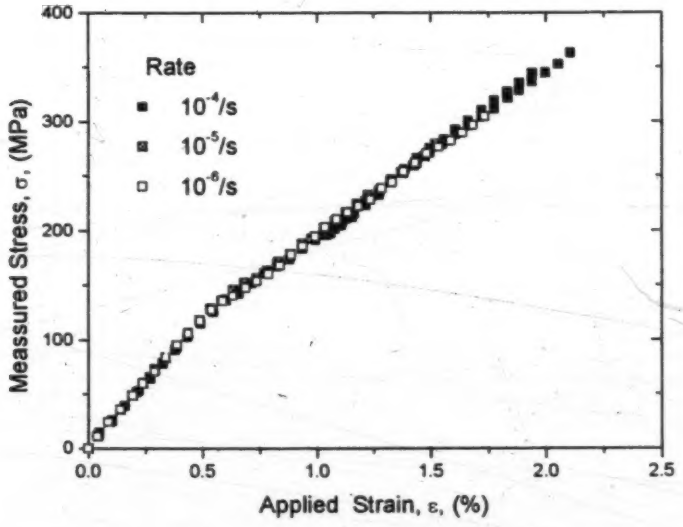

Figure 3.2 Stress-strain response for $[0_2/90_3]_S$ specimens.

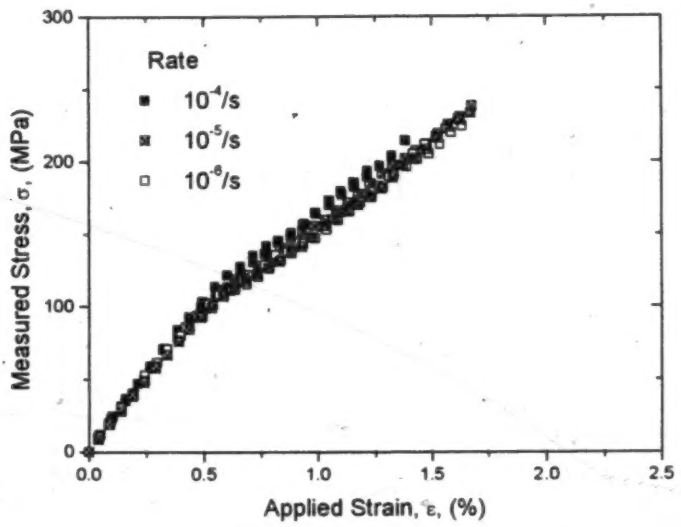

Figure 3.3 Stress-strain response for $[\pm 20/90_3]_S$ specimens.

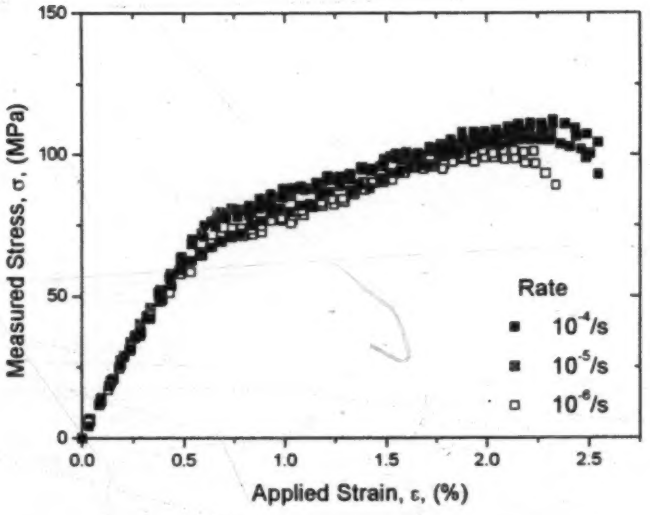

Figure 3.4 Stress-strain response for $[\pm 45/90_3]_S$ specimens.

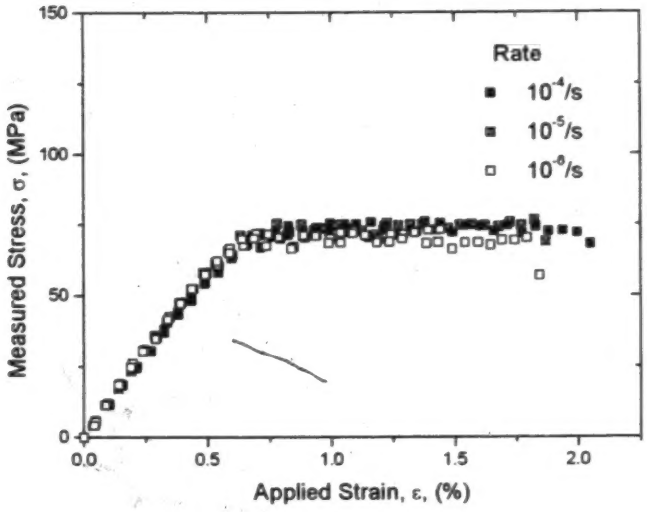

Figure 3.5 Stress-strain response for $[\pm 55/90_3]_S$ specimens.

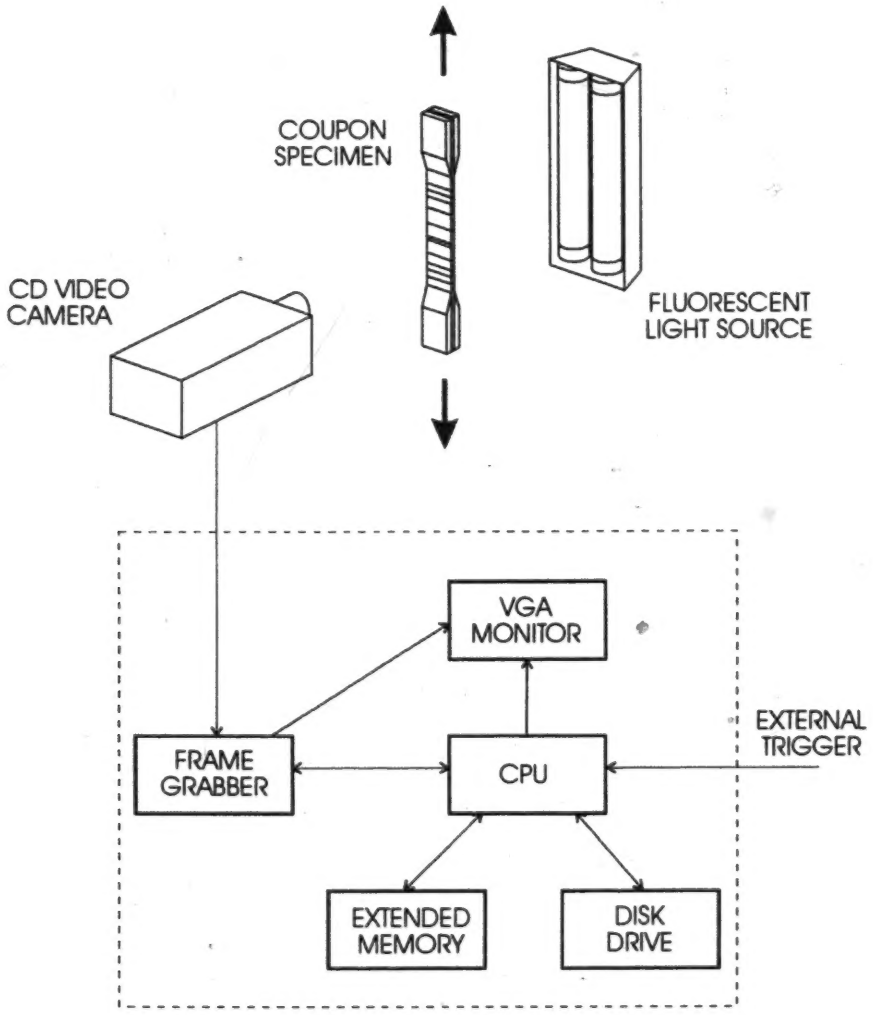

Figure 3.6 Schematic of image processor.

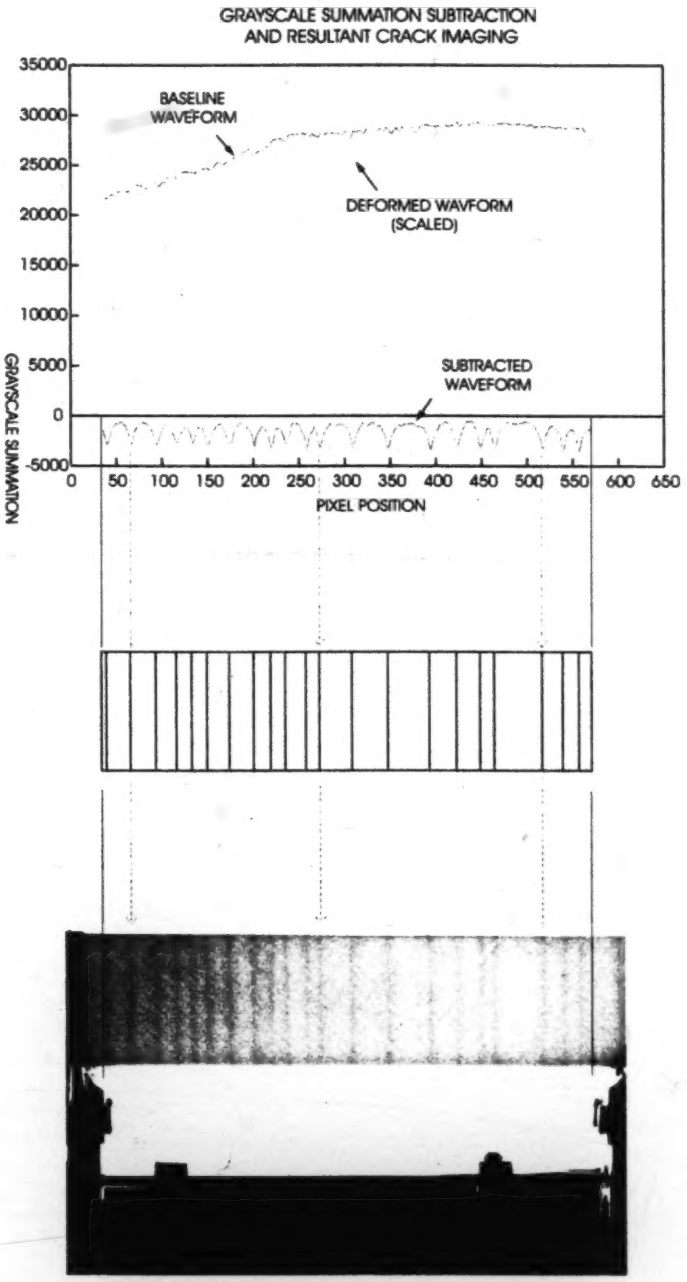

Figure 3.7 Image processor crack counting technique.

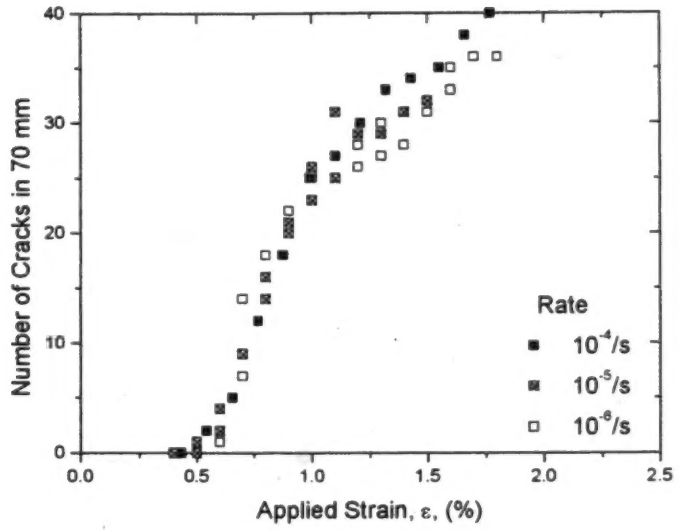

Figure 3.8 Transverse crack accumulation in $[0_2/90_3]_S$ specimens.

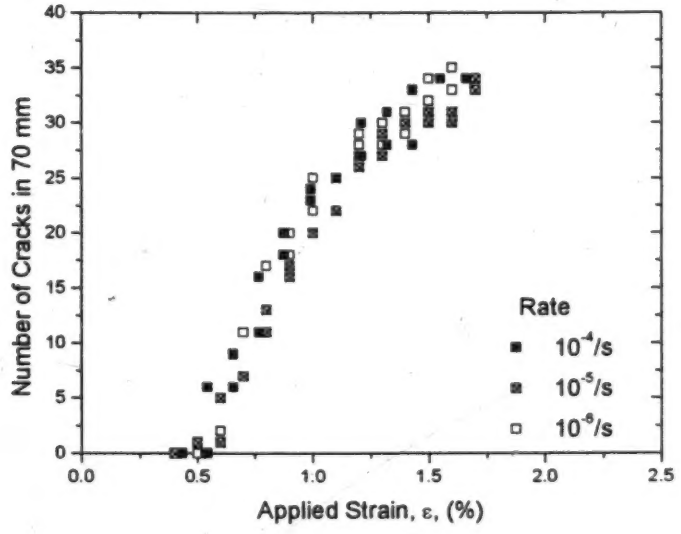

Figure 3.9 Transverse crack accumulation in $[\pm 20/90_3]_S$ specimens.

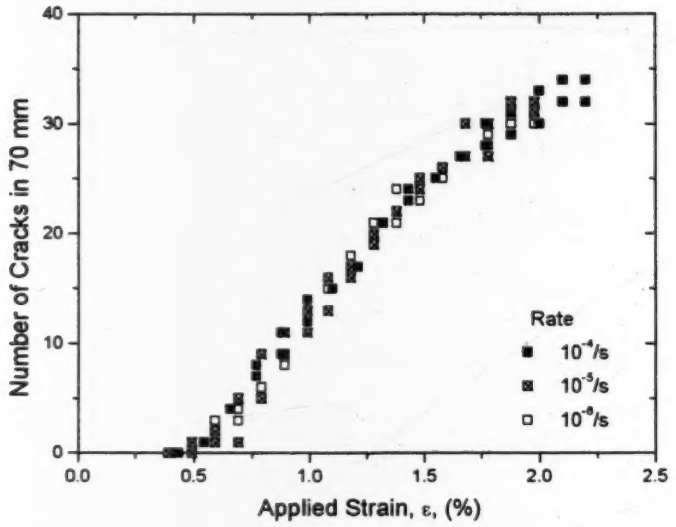

Figure 3.10 Transverse crack accumulation in $[\pm 45/90_3]_S$ specimens.

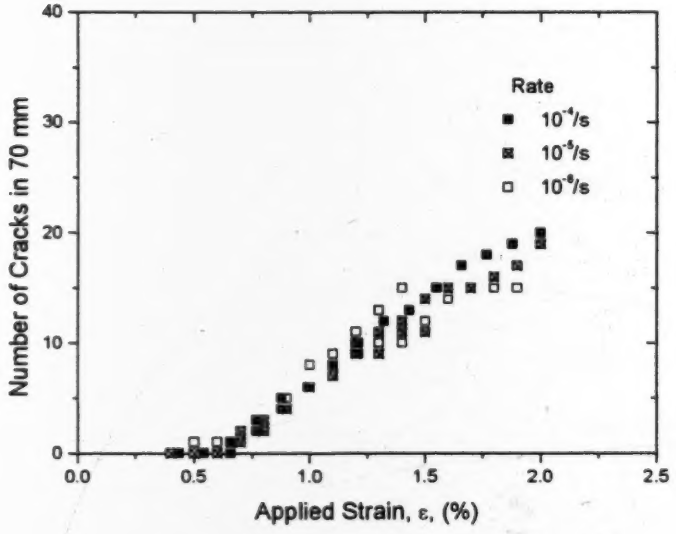

Figure 3.11 Transverse crack accumulation in $[\pm 55/90_3]_S$ specimens.

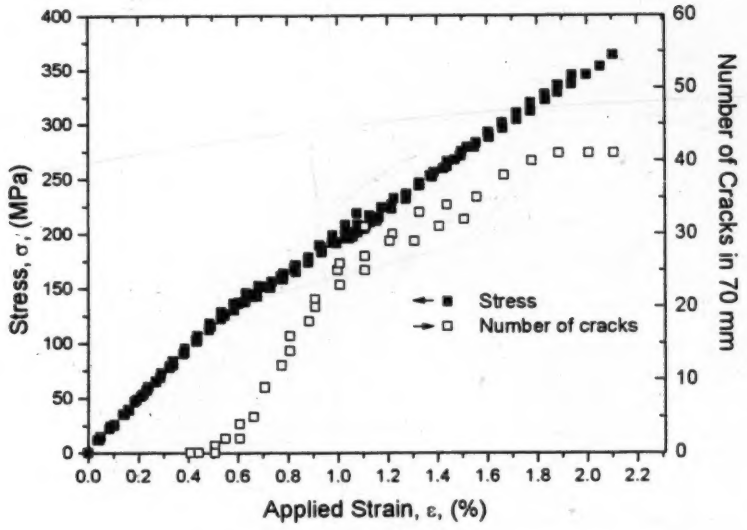

Figure 3.12 Applied Stress and Transverse crack accumulation in $[0_2/90_3]_S$ specimens.

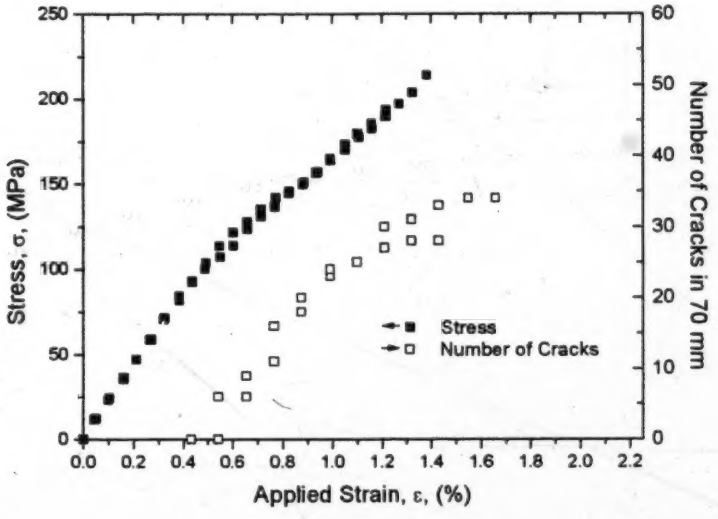

Figure 3.13 Applied Stress and Transverse crack accumulation in $[\pm 20/90_3]_S$ specimens.

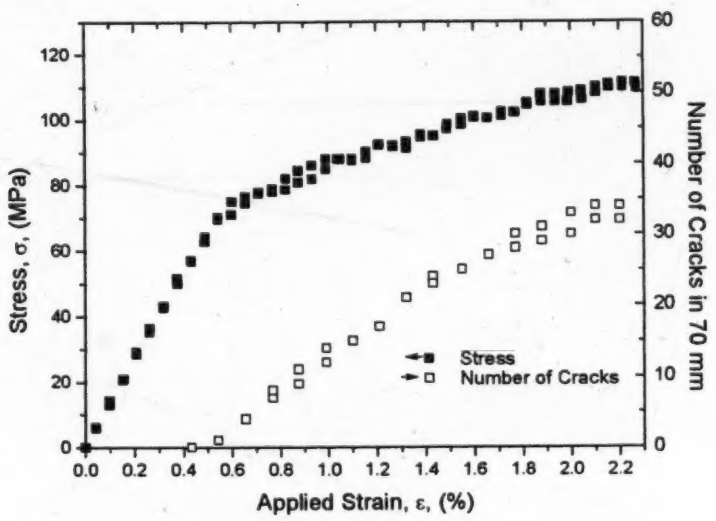

Figure 3.14 Applied Stress and Transverse crack accumulation in $[\pm 45/90_3]_S$ specimens.

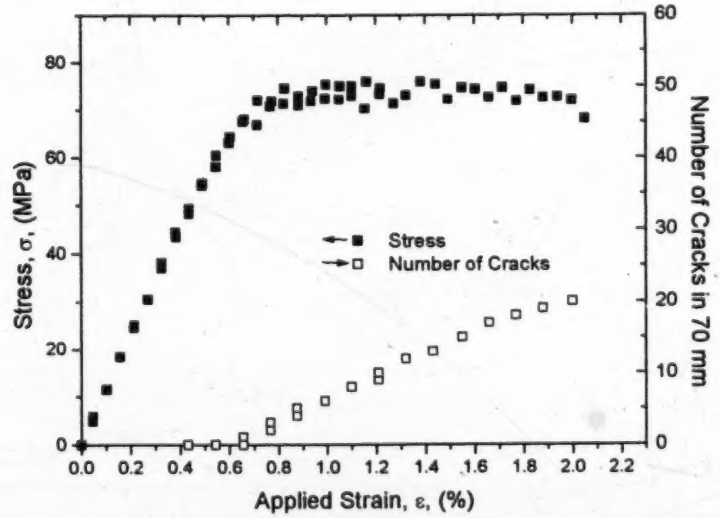

Figure 3.15 Applied Stress and Transverse crack accumulation in $[\pm 55/90_3]_S$ specimens.

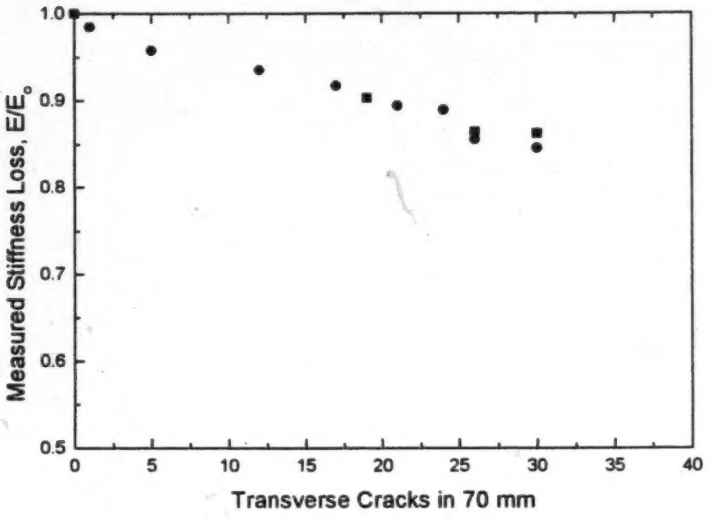

Figure 3.16 Measured stiffness loss in $[0_2/90_3]_S$ specimens.

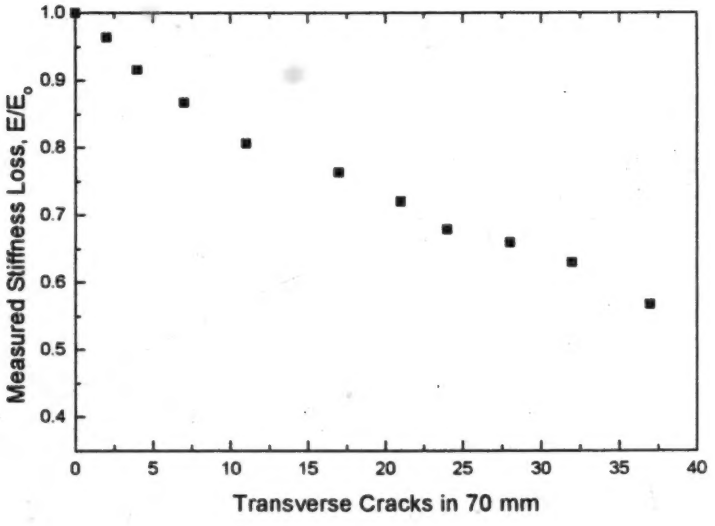

Figure 3.17 Measured stiffness loss in $[\pm 45/90_3]_S$ specimen.

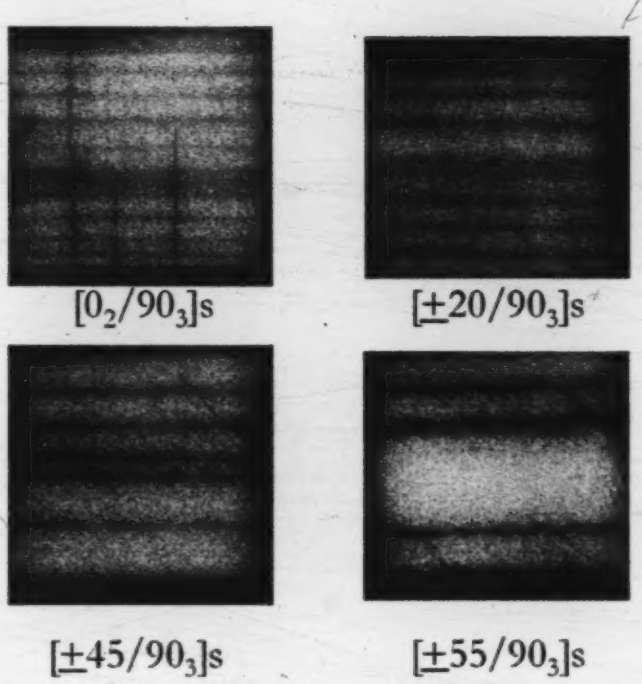

Figure 3.18 Penetrant enhanced front view of constraining ply damage in all specimens.

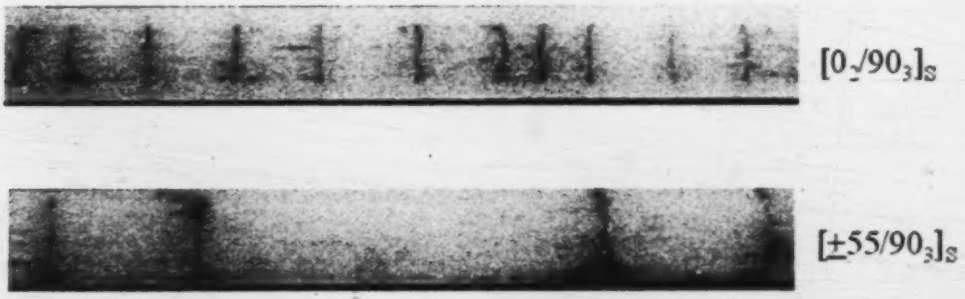

Figure 3.19 Penetrant enhanced side view of ply damage.

4. STRESS ANALYSIS OF CRACKED SYMMETRIC LAMINATES

A stress analysis is the first step in the process of modelling progressive failure in composite laminates. The name stress analysis is somewhat of a misnomer; in fact the analysis can determine the stress state, strain state, or the stiffness of a cracked laminate.

The goal of a stress analysis is to determine the distribution of the applied loads. From this information, one can determine if the load in any location is larger than may be maintained by the material. There are several methods of accomplishing this, and Chapter 5 deals exclusively with this topic, but it is informative at this time to highlight how the stress analysis and the failure criteria are related.

Consider a completed stress analysis that produces the stress state. From this information, one may invoke a maximum stress failure criterion and determine if any additional cracks might form in the laminate. This type of approach is a correct method but gives poor results. Current models invoke a fracture mechanics criterion. In this case, the work done in creating a new crack must be compared with the change in strain energy of the laminate to determine if the presence of the new crack is energetically admissible. The energy release rate measurement is quite straightforward but the strain energy can only be calculated if the stress and strain throughout the laminate are known.

In practice, the stiffness of a cracked unit cell is often the product of the stress analysis. For this reason, stress analysis and stiffness analysis are used interchangeably. In this chapter, the shear lag and the elastic element approaches both start with a determination of stiffness as a function of crack density. If one assumes uniform strain, the stiffness and strain can be used to determine the strain energy. From this point, applying fracture mechanics is straightforward.

This chapter deals exclusively with the stress analysis of cracked laminates. To begin, a literature review defines, explores, and criticizes the four main methods of stress analysis.

Before appling these models to the experimental results in Chapter 3, the assumptions and basic equations of several models are discussed. Finally, the models are applied to the experimental results in figures showing stiffness reduction due to multiple transverse cracks.

4.1 LITERATURE REVIEW

The problem of determining the stress state of a cracked laminate has been approached in many ways. This may be due to the difficulty of measuring the local stresses or perhaps researchers develop new approaches to improve model predictions. As time has progressed, the physical and mathematical complexity of the new models have increased. The newer models are becoming more and more difficult to solve but are capable of dealing with 2D and 3D problems rather than merely the in-plane values.

In this section, the models will be split into four main categories: internal variable, shear lag, elastic element, and variational methods. The models will be discussed roughly in chronological order of their appearance with, of course, some unavoidable overlap. It will be shown in Section 4.3 that the mathematics of the shear lag and elastic element methods are very similar and that the derivations produce similar governing equations.

4.1.1 Internal Variable Stress Analysis

Internal variable stress analysis can be divided into two approaches: Classical Laminate Theory and the continuum mechanics approach of Talreja. Classical Laminate Theory was one of the first methods used to study composite laminates. While there are serious limitations, it is still the most effective method to determine hygrothermal residual stresses, warpage of flat plates and elastic stiffness values of multidirectional laminates.

Classical Laminate Theory (CLT) transforms each lamina into a homogeneous orthotropic layer. While this simplifies the complex problem of thousands of fibres

arranged randomly in a matrix to a flat homogenous lamina with orthotropic properties, issues such as matrix cracking are very difficult to discuss after this homogenization.

The most common application of CLT is linear elastic analysis of multidirectional laminates. Beginning with the principle stiffness modulii, the stiffness matrix of each ply is transformed to the to the loading directions and the overall stiffness matrix of the laminate is calculated. Loads are applied to find the stresses in the laminate. Since each stiffness matrix is based on the engineering elastic constants (E_1, E_2, G_{12}, *etc.*), the analysis is limited to linear problems. Residual stresses and warpage of flat laminates are well within the elastic range and CLT is used often for these types of problems.

Damage is difficult to incorporate into a CLT model and often the methods of doing so are not based on any physics involved in the process. The CLT analysis of a problem produces a set of stresses in each layer, σ_1, σ_2 and σ_{12}. These calculated stresses can be compared with a strength of material failure criterion, *i.e.* transverse failure stress. It will be shown in Chapter 5 that the ultimate failure stress is not acceptable failure criterion and there is no correct physical method to change the stiffness matrix to account for the appearance of a new crack.

Ply discount [19, 28] is a method to change the stiffness matrix after the appearance of the first crack. Essentially the formulation is based on the unrealistic principle that one crack in a laminate eliminates the contribution of that lamina to the remaining structure. Section 4.3.1 describes this in more detail.

Talreja wrote a series of papers [44-47] on a damage mechanics approach in which the stiffness matrix was changed as a function of the crack density in the transverse plies. Hashin elegantly argued that the Talreja approach "results in a mathematical description of stiffness reduction involving a set of unknown ply damage constants which must be found experimentally" [48]. In addition, no failure criterion is involved which limits the use of this approach to stiffness reduction predictions.

4.1.2 Shear Lag Stress Analysis

Shear lag has been the most prolific method of stress analysis. It was used in the both the earliest [10, 12, 14] and most influential [19] works on the topic of matrix cracking. Shear lag methods have also been used in conjunction with probabilistic crack distributions [33-35, 41]. It has been used because it requires only basic material properties, is relatively simple, and provides a non-linear stiffness reduction resulting from increased crack density. The method is based on the continuity of the interfacial shear at ply interfaces.

The shear lag method is a one-dimensional analysis which determines the stresses as a function of their distance from a crack. The solution includes an undefined shear lag parameter which can be adjusted to fit the experimental data. The presence of this parameter allows for one to fit the stiffness reduction data very well but leaves the procedure partially undefined. Some authors have tried to define this parameter in term of first ply cracking [49-51] but this relies on experimental data. Section 5.3 describes how the first ply failure stress calculated from the Nuismer/Tan approach can be used to fully define the shear lag approach in terms of the fundament material constants.

4.1.3 Elastic Element Stress Analysis

The elastic element method is an advanced form of the shear lag approach and both methods have similar governing equations. The elastic element analysis calculates the in-plane stresses in both the loading and transverse to loading direction, includes out-of-plane material properties, but remains one-dimensional by determining stresses as a function of x only (the x direction is the loading direction). The elastic element method contains one more assumption than the shear lag approach and the derivation is more involved but the extra effort eliminates the adjustable parameter that undermines the shear lag method. The greatest advantage of the elastic element method is that it is the simplest method to predict progressive matrix cracking entirely from material properties.

4.1.4 Variational Elasticity Stress Analysis

The variational approach is the most advanced form of stress analysis. It is also the most recently proposed method and the most mathematically advanced. The method was initially proposed by Hashin [48] and subsequently used by Nairn *et al.* [52-55], Varna *et al.* [56-59] and Motogi and Fukuda [60].

The variational method is derived from the specimen geometry and the assumption that stresses are uniform across the thickness of each ply. The procedure is to first propose an arbitrary stress state that satisfies boundary conditions and then apply variational calculus and the principle of minimum energy to find the most probable stress distribution. Unlike the methods above, the variational method can be expanded into 2D and 3D analysis. Nairn [55] argues that only 2D and 3D methods will be able to provide predictions independent of geometric and material nuances.

The major barrier to implementation of this method is the imposing mathematics involved. At this time, the variational method has been derived for crossply specimens but significant complexities arise as the angle of constraining plies changes from 0°. The scope of this work is not large enough to include the implementation of the variational method to the current experimental data.

4.1.5 Limit of Analysis

All of the methods described above are based on the elastic material properties. Non-linear effects, such as viscoelastic behaviour, plastic deformation, stress relaxation, and constraint ply cracking, are not accountable in any model. In the case of crossply specimens, non-linear behaviour is limited and the predictions are reasonable. However, as the angle of the containing plies becomes greater than 20°, the predictions of the models become poor. Section 3.4 discussed the onset of constraining ply cracking and how this may effect the

ability of the models to prediction mechanical response. A important subject that needs addressing is the stiffness analysis of viscoelastic or cracked constraining plies.

4.2 BASIC EQUATIONS OF STRESS ANALYSIS

The stress analysis predictions of several models were evaluated by comparing predictions with experimental data of this study. To do this one can discuss the actual stress distributions as they vary throughout the laminate or show the stiffness reduction as a function of the crack density. Of these two, it is much easier to measure and plot stiffness reduction from experiment.

If this approach is taken to evaluate stress analysis models, as is done in most journal publications, it is difficult to understand the limitations and assumptions of each method. In fact, many stiffness reduction models appear to produce excellent predictions. One can only really determine the effectiveness of a model if the fundamentals of the derivation are understood. This section briefly describes the derivation of four models: CLT and ply discount, the damage mechanics method of Talreja, the shear lag approach, and the elastic element model of Nuismer and Tan. Space limits the amount of material that can be described here. It is recommended that the original references be consulted for more information.

4.2.1 Classical Laminate Theory

The overall behaviour of a laminated structure depends on material type and geometry. Classical Laminate Theory (CLT) is a continuum mechanics-based approach to determining the elastic mechanical response of laminates of arbitrary orientation. The theory has been developed within the framework of the following assumptions [28]:

1. Each layer (lamina) is quasihomogenious and orthotropic.
2. The laminate is thin and each layer is in a state of plane stress

3. All displacements are small compared to the thickness of the laminate.
4. Displacements are continuous throughout the laminate.
5. In-plane displacements vary linearly through the thickness of the laminate.
6. Transverse shear strains are negligible.
7. The behaviour of the laminate is linear elastic.
8. Normal distances from the middle surface remain constant.

Assumption 1 forms a uniform orthotropic ply out of the non-uniform lamina. Immediately one loses sensitivity to some issues due to this averaging process. Assumption 7 limits the use of this theory to the linear elastic region. However, bilinear stress-strain curves can be approximated with the ply discount approach [19,28].

4.2.1.1 Basic Relations of Classical Laminate Theory

The derivation of the in-plane response of a laminate begins with assumption 4. The continuous displacement throughout the laminate in the reference plane, u_o, is used to find the reference plane strain, ε_x^0

$$u_0 = u_0(x, y) \qquad \varepsilon_x^o = \frac{\partial u_0}{\partial x}$$

The stresses in the material directions are found from the constitutive relations

$$[\sigma]_{1,2}^k = [Q]_{1,2}^k [\varepsilon^0]$$

where $[Q]$ is the laminate stiffness matrix found from the engineering constants in the principle directions

$$Q_{11} = \frac{E_1}{(1-\nu_{12}\nu_{21})}$$

$$Q_{22} = \frac{E_2}{(1-\nu_{12}\nu_{21})}$$

$$Q_{12} = \frac{\nu_{12}E_2}{(1-\nu_{12}\nu_{21})}$$

$$Q_{66} = G_{12} \tag{4.1}$$

The laminate stiffness matrix in the material direction can be transformed to the loading direction

$$[\sigma]^k_{x,y} = [Q]^k_{x,y}[\varepsilon^0] \tag{4.2}$$

and the force $[N]_{x,y}$ required to achieve the strain, $[\varepsilon^o]$, is found by integrating the stress over the entire thickness, dz

$$[N]_{x,y} = \sum_{k=1}^{n} \int_{h_{k-1}}^{h_k} [\sigma]_{x,y}\, dz = \sum_{k=1}^{n} \int_{h_{k-1}}^{h_k} [Q]^k_{x,y}[\varepsilon^0]\, dz \tag{4.3}$$

In the integral above, the strain is uniform over the entire thickness so it can be removed from underneath the integral

$$[N]_{x,y} = \left[\sum_{k=1}^{n} [Q]^k_{x,y} \int_{h_{k-1}}^{h_k} dz\right][\varepsilon^0]$$

$$[N]_{x,y} = \left[\sum_{k=1}^{n} [Q]^k_{x,y}(h_k - h_{k-1})\right][\varepsilon^0]$$

$$[N]_{x,y} = [A][\varepsilon^0] \tag{4.4}$$

Where the A_{ij} are the extensional stiffnesses, or in-plane laminate modulii, relating to the in-plane strains. From the matrix of applied forces, [N], and the in-plane strains, [ε^0], one can determine the engineering constant E_x

$$E_x = A_{11} - \frac{A_{12}^2}{A_{22}} \tag{4.5}$$

4.2.1.2 Ply Discount Theory

Ply discount theory is an attempt to predict the stress-strain behaviour of a damaged laminate. It follows the same formulation as CLT but the input engineering constants are changed after damage has been incurred [28].

The composite material tested in this study developed the first crack at approximately 0.6% strain. The effect of this crack was to decrease the tensile modulus in the off-axis direction, E_2, and the in-plane shear modulus, G_{12}, of the transverse plies. The approach of ply discount theory is to set G_{12} and E_2 to 0 for all cracked plies and recalculate the laminate stiffness matrix $[Q]_{12}$ (eq. 4.1). In essence, the appearance of the first crack acts to remove the contribution of the entire cracked ply to the stiffness of the laminate in the direction perpendicular to the crack. With the new stiffness matrix, the new stiffness value of E_x can be calculated (eq. 4.5).

4.2.2 Damage Mechanics Approach of Talreja

One type of internal variable method uses damage mechanics to model stiffness reduction. Talreja [44, 45, 46, 47] has developed an approach to describe the elastic constitutive behaviour of composite materials with parallel cracks. The theory characterizes each set of parallel cracks by a vector field and derives a relationship between the overall elastic moduli and magnitudes of the damage vectors. This approach is one of the few that account for angle ply cracking. A debilitating limitation, however, is that there are four

unknown constants which must be determined from the drop in the four elastic moduli at some crack density. In addition, implementation of a failure criterion is difficult due to the inability of the model to calculate strain energy in the laminate. Hence, fitting experimental data using visual judgement [47] is necessary to determine the crack density development.

The damage mechanics model begins by determining damage vectors for any set of cracks oriented in any direction (Fig. 4.1). To each parallel crack array, a damage vector is assigned

$$\tilde{V}^{(\alpha)} = D^{(\alpha)}\tilde{n}^{(\alpha)}, \alpha = 1,2,..m$$

where $n^{(\alpha)}$ is a unit vector oriented normal to the planes of the α^{th} crack array and $D^{(\alpha)}$ is the magnitude of the vector $V^{(\alpha)}$. The magnitude of the vector can be found

$$D^2 = \tilde{V} \cdot \tilde{V} = \frac{\eta_c \cdot \bar{l}_c \cdot \bar{w}_c \cdot t_c}{t} \tag{4.6}$$

where η_c is the number of cracks per unit surface area, and l_c and w_c are the average length and width, respectively, of the cracks in the array. t_c and t are the thicknesses of the cracked ply and total laminate, respectively.

The stress-strain relations are given by

$$\sigma_p = (C^0_{pq} + C^{(\alpha)}_{pq})\varepsilon_q$$

where $C_{pq}{}^0$ is the stiffness of the undamaged composite and $C_{pq}{}^{(\alpha)}$ are the matrices whose coefficients are the functions of the damage vectors. For the case of transverse cracking in the transverse ply and undamaged constraining plies

$$\tilde{V} = D(1,0)$$

where the (1,0) indicates that the normal to the crack direction is in the (1,0) direction (Fig. 4.2). The matrix $C_{pq}^{(\alpha)}$ now becomes

$$C_{pq}^{1} = \begin{bmatrix} 2k_3D^2 & k_{13}D^2 & 0 \\ k_{13}D^2 & 2k_7D^2 & 0 \\ 0 & 0 & 2k_{11}D^2 \end{bmatrix}$$

and the residual elastic modulus in the loading direction is

$$E_1 = E_1^0 - 2\frac{t_c^2 k}{tl}[c_3 + c_8(\nu_{12}^0)^2 - c_{16}\nu_{12}^0] \tag{4.7}$$

where the c_i are the material constants associated with the state of damage. Their solutions are obtained from

$$\begin{aligned} kc_3 &= A_1(2\nu_{12}^0\nu_{21}^0 - 1) - A_2(\nu_{12}^0)^2 - 2A_3E_2^0\nu_{12}^0 \\ kc_8 &= A_1(\nu_{21}^0)^2 - A_2 - 2A_3E_2^0\nu_{12}^0 \\ kc_{13} &= -A_4 \\ kc_{16} &= 2A_1\nu_{12}^0(\nu_{21}^0)^2 - 2A_2\nu_{12}^0 - 2A_3E_2^0(1 + \nu_{12}^0\nu_{21}^0) \end{aligned} \tag{4.8}$$

in which

$$A_1 = \frac{t}{2t_c^2(1-\nu_{12}^0\nu_{21}^0)^2}\frac{E_1 - E_1^0}{\eta}$$

$$A_2 = \frac{t}{2t_c^2(1-\nu_{12}^0\nu_{21}^0)^2}\frac{E_2 - E_2^0}{\eta}$$

$$A_3 = \frac{t}{2t_c^2(1-\nu_{12}^0\nu_{21}^0)^2}\frac{\nu_{12} - \nu_{12}^0}{\eta}$$

$$A_3 = \frac{t}{2t_c^2}\frac{G_{12} - G_{12}^0}{\eta} \tag{4.9}$$

where η is the number of transverse cracks per unit length of the laminate. One will note that in order to determine an expression for the decrease in E_1, kc_i and A_i must be calculated. Since E_1 is used to find A_i, we are left finding E_1 based on a measured E_1. Hence, stiffness reduction curves can only be accomplished once the stiffness reduction data is produced. In addition, once A_i and kc_i are calculated, the expression for E_1 becomes

$$E_1 = E_1^0 - c\eta \tag{4.10}$$

where c is a constant [21]. The damage mechanics approach reduces to nothing more than a linear curve fit to the stiffness reduction data. Furthermore, this approach cannot incorporate a failure criterion to model progressive damage. The original work instructs one to insert the change in the four elastic moduli at any given crack density into the equations to obtain the desired constants [47].

4.2.3 A Shear Lag Approach to Progressive Cracking in Composite Laminates

The shear lag method has been used extensively to model progressive cracking in laminates [12, 14, 19, 33-35, 41, 49-51]. The approach is based on equilibrating shear stresses at the interface between transverse and longitudinal plies and solving for the stress state. Various methods of progressive cracking have been used that include assuming either

uniform cracking [14] or probabilistic crack distributions [17, 33-35]. In every shear lag analysis, there is an adjustable shear lag parameter. Later papers attempted to develop methods of well-defining this parameter [49-50]. In this section we will follow the derivation of Laws and Dvorak [49] shear lag theory. It varies somewhat from the other shear lag derivations but only slight differences are involved.

For simplicity, we will only consider the case of symmetric crossply laminates is this discussion. In addition, the analysis focuses exclusively on the stresses in the x-direction (loading direction). For a laminate cured at an elevated temperature, residual stresses develop

$$b\sigma_l^R + d\sigma_t^R = 0$$

where b is the thickness of the outer 0° plies and d is the half-thickness of the 90° plies (Fig. 4.3). Assuming that the displacement of a particular layer is uniform over the thickness of that layer, the strains in the transverse, t, and 0° (longitudinal), l, plies are

$$\varepsilon_t = \frac{dv}{dx} \qquad \varepsilon_l = \frac{du}{dx}$$

where $u(x)$ is the uniform displacement of the 0° layer and $v(x)$ is the displacement of the 90° layer. Equilibrium of stresses implies that

$$\tau = -b\frac{d\sigma_l}{dx} = d\frac{d\sigma_t}{dx}$$

where the stresses are the result of combined residual and mechanical loads (Fig. 4.4). The key assumption of the shear lag approach is that shear stress is proportional to the relative displacement

$$\tau = K(v-u) \tag{4.11}$$

where K is a constant. In order to solve for the stress distribution, the strain energy per unit width between two sections due to the applied loads is calculated. From the strain energy, a set of differential equations can be derived

$$\frac{d^2\sigma_t}{dx^2} - \frac{\xi^2}{d^2}\sigma_t = \frac{\xi^2}{d^2}\left(\sigma_t^R + \frac{E_t}{E_o}\sigma_o\right) \tag{4.12}$$

where E_0 is the original laminate stiffness (from CLT) and

$$\xi^2 = \frac{Kd(bE_l + dE_t)}{bE_lE_t} \tag{4.13}$$

is the non-dimensional shear lag parameter. In the next section, a method to calculate this parameter is described. If one applies crack surface boundary conditions

$$\sigma_t = 0, when \qquad x = \pm h$$

The differential equation can be solved for the stresses and displacements in the laminate respectively

$$\sigma_t = \left(\sigma_t^R + \frac{E_t}{E_0}\sigma_o\right)\left(1 - \frac{\cosh\frac{\xi x}{d}}{\cosh\frac{\xi h}{d}}\right) \tag{4.14}$$

$$u = \frac{\sigma_a}{E_0} + \frac{d^2}{\xi b E_l}\left(\sigma_t^R + \frac{E_t}{E_0}\sigma_a\right)\frac{\sinh\frac{\xi x}{d}}{\cosh\frac{\xi h}{d}} + c_1 \tag{4.15}$$

The strain can be found from the displacements and used to determine the stress.

$$\varepsilon_a = \frac{u(B)-u(A)}{2h} = \frac{\sigma_a}{E_0}\left\{1 + \frac{d^2 E_t}{\xi h b E_l}\tanh\frac{\xi h}{d}\right\} + \frac{d^2\sigma_t^R}{\xi h b E_l}\tanh\frac{\xi h}{d} \tag{4.16}$$

$$\sigma_a = E_0\left\{\varepsilon_a - \frac{\beta}{\xi}\frac{d\sigma_t^R}{bE_l}\tanh\frac{\xi}{\beta}\right\}\left\{1 + \frac{\beta}{\xi}\frac{dE_t}{bE_l}\tanh\frac{\xi}{\beta}\right\}^{-1} \tag{4.17}$$

4.2.3.1 Determining the Shear Lag Parameter, ξ

One criticism of past shear lag analyses has been that the shear lag parameter, ξ, is undefined and obtained by fitting the model results to stiffness reduction data [19, 14, 41, 12]. As a result, shear lag theory often reproduces the experimental stiffness loss data very well. Later papers on the subject have attempted to correct this shortcoming by expanding the derivation to include a branch connecting the shear lag parameter and some independently measurable property [49, 50]. This section will continue with the Laws and Dvorak derivation and illustrate how the shear lag parameter, ξ, can be measured from experiment.

Chapter 5 deals exclusively with the implementation of a failure criterion to the transverse cracking analysis. In order to determine ξ, however, the findings of Section 5.3 will be summarized here. Consider a cracked ligament (Fig. 4.5) which initially has cracks at A and B separated by distance $2h$. The ligament, under appropriate stress, fails at C and changes the cracks spacing to h_1 and h_2. A fracture mechanics technique is then imposed and the energy release rate, G, is calculated

$$G = \frac{d(b+d)E_0}{\xi b E_1 E_t}\left(\sigma_t^R + \frac{E_t}{E_0}\sigma_a\right)^2\left\{\tanh\frac{\xi h_1}{2d} + \tanh\frac{\xi h_2}{2d} - \tanh\frac{\xi h}{d}\right\} \tag{4.18}$$

where σ_a is the applied stress. First ply failure occurs when all crack spacings, h_i, are taken to be large and the energy release rate is set to the critical value, G_c. The equation reduces to

$$\sigma_a^{fpf} = \left\{\frac{\xi b E_1 E_0 G_c}{d(b+d)E_t}\right\}^{1/2} - \frac{E_0}{E_t}\sigma_t^R \tag{4.19}$$

where σ_a^{fpf} is the first ply failure stress. If the standard geometric and material data are provided (b, d, E_1, E_t), then σ_t^R and E_0 can be calculated from Classical Laminate Theory. Since both σ_a^{fpf} and G_c can be determined experimentally, this equation can be regarded as the rule which determines the shear lag parameter, ξ.

4.2.3.2 Stiffness Reduction

From the basic equations described above, the stiffness can be related to the average crack density

$$E(\beta) = E_0\left\{1 + \frac{\beta}{\xi}\frac{dE_t}{bE_1}\tanh\frac{\xi}{\beta}\right\}^{-1} \tag{4.20}$$

where $\beta = d/h$ is a normalized crack density parameter. When $\beta = 0$, the stiffness is E_0 and as β approaches infinity

$$E \to E_0\left(1 + \frac{dE_t}{bE_1}\right)^{-1} = \frac{bE_1}{b+d}$$

which is the result given by setting the transverse stiffness of the transverse ply to zero (ply discount theory).

4.2.4 The Elastic Element Theory of Nuismer /Tan

The model developed by Nuismer and Tan [37-38] was chosen because it requires only fundamental mechanical properties to predict laminate behaviour. These properties can be measured independently. The model is based on an approximate elastic solution, linear elastic fracture mechanics and it applies to laminates with multiple 90° plies and symmetric constraining plies. General in-plane loading, including the effects of non-mechanical strains (residual hygrothermal strains), is handled.

Consider the uniformly transverse cracked laminate subjected to general in-plane loads of Figure 4.6. Due to the symmetry of the problem, the laminate section can be reduced to a quarter unit cell (Fig. 4.7). The assumption is made that the load, material and geometry are uniform in the y-direction. Each lamina is considered orthotropic

$$\begin{Bmatrix} \sigma_x^{(i)} \\ \sigma_y^{(i)} \\ \sigma_z^{(i)} \\ \tau_{yz}^{(i)} \\ \tau_{xz}^{(i)} \\ \tau_{xy}^{(i)} \end{Bmatrix} = \begin{bmatrix} C_{11}^{(i)} & C_{12}^{(i)} & C_{13}^{(i)} & 0 & 0 & 0 \\ C_{12}^{(i)} & C_{22}^{(i)} & C_{23}^{(i)} & 0 & 0 & 0 \\ C_{13}^{(i)} & C_{23}^{(i)} & C_{33}^{(i)} & 0 & 0 & 0 \\ 0 & 0 & 0 & C_{44}^{(i)} & 0 & 0 \\ 0 & 0 & 0 & 0 & C_{55}^{(i)} & 0 \\ 0 & 0 & 0 & 0 & 0 & C_{66}^{(i)} \end{bmatrix} \begin{Bmatrix} \varepsilon_x^{(i)} - \varepsilon_{xN}^{(i)} \\ \varepsilon_{yz}^{(i)} - \varepsilon_{yzN}^{(i)} \\ \varepsilon_z^{(i)} - \varepsilon_{zN}^{(i)} \\ \gamma_{yz}^{(i)} \\ \gamma_{xz}^{(i)} \\ \gamma_{xy}^{(i)} \end{Bmatrix}$$

where the subscript *N* refers to the nonmechanical strains.

From this point, application of the equations of stress equilibrium with the assumption of interfacial shear stress continuity completes the solution. An approximation is made which assumes that average properties across a lamina thickness can be defined

$$\left(\bar{\ }\right)^{(i)} = \frac{1}{h^{(i)}} \int_{h^{(i)}} (\ )^{(i)} dz$$

and the assumed thinness of the laminate implies that no out-of-plane stresses are present.

Application of stress equilibrium and the average approximation on the orthotropic lamina relations results in the average in-plane normal constitutive relations. If one assumes that the shear strain distribution through the thickness is linear

$$\begin{aligned}
\tau_{xz}^{(1)} &= a(x) \cdot z \\
\tau_{xz}^{(2)} &= a(x) \cdot h^{(1)} \left(\frac{\bar{h} - z}{\bar{h} - h^{(1)}} \right) \\
\tau_{yz}^{(1)} &= b(x) \cdot z \\
\tau_{yz}^{(2)} &= b(x) \cdot h^{(1)} \left(\frac{\bar{h} - z}{\bar{h} - h^{(1)}} \right)
\end{aligned} \tag{4.21}$$

the out-of-plane shear constitutive relations can be found. The final step is to solve for the unknown constants by solving the ordinary differential equation

$$\tau^{*''} - \alpha_1^2 \tau^* = 0 \tag{4.22}$$

where τ^* is the xz shear stress at the interface. Application of boundary conditions and subsequent integration leads to the damaged laminate stiffness relations

$$\begin{aligned}
\bar{\sigma}_x &= \bar{A}_{11} \bar{\varepsilon}_x + \bar{A}_{12} \bar{\varepsilon}_y - \bar{\sigma}_{xN} \\
\bar{\sigma}_y &= \bar{A}_{12} \bar{\varepsilon}_x + \bar{A}_{22} \bar{\varepsilon}_y - \bar{\sigma}_{yN}
\end{aligned}$$

where

$$\overline{A}_{11} = \frac{h^{(1)}Q_{11}^{(1)} + h^{(2)}Q_{11}^{(2)}}{\beta_2 \overline{h}}$$

$$\overline{A}_{12} = \frac{\beta_1 h^{(1)}Q_{12}^{(1)} + \beta_2 h^{(2)}Q_{12}^{(2)}}{\beta_2 \overline{h}}$$

$$\overline{A}_{22} = \frac{h^{(1)}Q_{22}^{(1)} + h^{(2)}Q_{22}^{(2)}}{\overline{h}} - \left(\frac{\beta_2 - \beta_1}{\beta_2}\right)\left(\frac{h^{(1)}Q_{12}^{(1)^2}}{\overline{h}Q_{11}^{(1)}}\right)$$

$$\overline{\sigma}_{xN} = \frac{\beta_1 h^{(1)}\sigma_{xN}^{(1)} + \beta_2 h^{(2)}\sigma_{xN}^{(2)}}{\beta_2 \overline{h}}$$

$$\overline{\sigma}_{yN} = \frac{h^{(1)}\sigma_{yN}^{(1)} + h^{(2)}\sigma_{yN}^{(2)}}{\overline{h}} - \left(\frac{\beta_2 - \beta_1}{\beta_2}\right)\left(\frac{h^{(1)}Q_{12}^{(1)}}{\overline{h}Q_{11}^{(1)}}\right)\sigma_{xN}^{(1)} \tag{4.23}$$

and

$$\beta_1 = 1 - \frac{\tanh \alpha_1 l}{\alpha_1 l}$$

$$\beta_2 = 1 + \left(\frac{h^{(1)}Q_{11}^{(1)}}{h^{(2)}Q_{11}^{(2)}}\right)\frac{\tanh \alpha_1 l}{\alpha_1 l} \tag{4.24}$$

The stiffness of the quarter cell under plane stress conditions then is

$$E_x(l) = \overline{A}_{11}(l) - \frac{\overline{A}_{12}^{\,2}(l)}{\overline{A}_{22}(l)} \tag{4.25}$$

where $E_x(l)$ is now a function of the length of the elastic element, l. Crack density is the inverse of l and is therefore uniform.

The undamaged stiffness relations can be found from setting l to infinity. An extremely important result of this analysis is that the constraining ply stiffness, $Q_{11}^{(2)}$, is a variable of the relation describing β_2. Thus, the damaged ply constitutive relations are

laminate dependent. Classical Laminate Theory and the damage mechanics formulation of Talreja assume that the damaged ply constitutive relations are laminate independent.

It should be noted that the measured value of G_{23} was used to calculate the elastic constant A_{55} and crack damage parameter α_1. For the case of 0° constraining plies, G_{23} is well defined but in the case of $\pm\theta$ constraining plies, the out-of-plane shear stiffness of both plies may not be the same as for the single $+\theta$ ply. In this study, the G_{23} of the single θ ply was assumed to be the same as the $\pm\theta$ plies. It is not known what effect this assumption may have.

4.3 PREDICTING STIFFNESS REDUCTION

Experimentally measured stiffness reduction has already been presented in Chapter 3. In this section, we apply internal variable, shear lag and elastic element models to the data to evaluate the effectiveness of each stress analysis.

Figures 4.8-4.9 show the predictions of the two internal variable methods: Classical Laminate Theory and the damage mechanics approach of Talreja. The CLT prediction is based on ply discount theory. Upon the appearance of the first crack, the transverse and shear moduli of the transverse ply are set to zero and the global stiffness is recalculated. For this reason, the ply discount prediction is a horizontal line in the figures. For the crossply $[0_2/90_3]_s$ specimens, the experimental data reach half of the ply discount prediction. In the case of the $[\pm45/90_3]_s$ specimen, the prediction is slightly better as the stiffness appears to be asymptotically approaching the ply discount prediction. It would appear that the CLT/ply discount theory does not provide a useful stress analysis. This should not be a surprise since the CLT approach homogenizes the constituents of the layer and no relation is provided between the number of cracks in a laminate and the stiffness of that laminate. The single value provided by the model is not suitable for progressive matrix cracking. Interestingly,

the next chapter will show that the ply discount approach can be used in conjunction with an experimentally determined first ply failure strain to model the stress-strain curve.

The other internal variable model which was plotted is the damage mechanics approach of Talreja. Section 4.2.2 provided the derivation of this model and showed that it reduced to a linear curve fit of the data. Figures 4.8-4.9 show the Talreja model that was created with a linear relation between the uncracked stiffness and the maximum stiffness reduction as suggested in the original reference [44]. In the case of the crossply specimens, the linear prediction is good but for the $[\pm 45/90_3]_S$ specimen, the results are poor and most of the data points lie off the line. It should be reiterated that the model is only a linear curve fit with no failure criterion and thus has limited functionality.

Two other models were also applied to the stiffness reduction data and are shown in Figures 4.10-4.11. The shear lag model explained in Section 4.2.3 equilibrates the shear stresses at the interface and solves the governing equation by assuming that the shear stress is proportional to the relative displacements of the transverse and constraining layers. The proportionality constant reveals itself in the final formulation of the theory in the form of the shear lag parameter, ξ.

In order to calculate the shear lag parameter, the first ply failure stress and the critical energy release rate, G_c, must be known. The specific fracture energy, γ_T, was determined in Section 2.5 and linear elastic fracture mechanics shows [26] that the energy release rate is simply twice the specific fracture energy. The first ply failure stress can be obtained from experiments which the original authors [49] suggest but the goal of the analysis is to formulate a prediction based only on material constants. Instead, the first ply failure stress calculated with the elastic element method (Section 5.4) was used. These values were predicted from undamaged laminate material constants and were close to the experimental values. Using this hybrid approach, the calculated shear lag parameters were 1.87 for the $[0_2/90_3]_S$ specimens and 1.09 for the $[\pm 45/90_3]_S$ specimens. (The accuracy of the first ply

failure stresses can be seen in Figures 5.23-5.26. Note that both models show crack initiation at the same stress level. The calculated stresses seem to lie within the data scatter.)

Figures 4.10-4.11 show the shear lag predictions of the stiffness reduction. In the case of the crossply specimens (Fig. 4.10), the curve follows the trend of the data as cracks accumulate. The prediction is close to all data points but could be improved as the curve appears to slightly overestimate the stiffness reduction. In the case of the $[\pm 45/90_3]_s$ specimen, the trend of the data is well represented but the curve is above the data. In this case, the prediction underestimates the stiffness reduction. This may be due to cracking in the constraining plies that cause additional stiffness reduction or inelastic behaviour of the constraining plies. The observation that the ±45° plies contained matrix cracks across the transverse cracks was described in Chapter 3. It should be noted that the abscissa ranges from 0.35 to 1 and this may make the errors appear artificially large.

It must be remembered that the shear lag approach has a variable parameter in the formulation. If required, the shear lag parameter could be varied until the curve matched the stiffness reduction data. In fact, this curve fitting could also be conducted by changing the first ply failure stress until the desired ξ value was obtained. The author acknowledges this possibility but emphasizes that the shear lag predictions in this study are based solely on undamaged laminate material constants and are fully independent of any data obtained from cracked laminates.

Also plotted in Figures 4.10-4.11 are the Nuismer/Tan [37] elastic element model predictions. For the $[0_2/90_3]_s$ specimens (Fig. 4.10), the elastic element model correctly predicts the experimental data. The accuracy of the model is very encouraging and indicates that the stress analysis could be very useful in modelling progressive damage. The accuracy of the model is partly due to the constraining plies behaving in an elastic manner.

The accuracy of the elastic element prediction is lost as the angle of constraining ply increases as with the $[\pm 45/90_3]_s$ specimens (Fig. 4.11). One can see from the figure that the

elastic element prediction underestimates the stiffness loss due to the presence of cracks. The cause of this underestimation is probably constraining ply cracking as was the case for the shear lag prediction. The effect of these constraining cracks is to decrease the stiffness of the overall laminate and are the source for the additional stiffness loss not predicted by the model.

FIGURES - CHAPTER 4

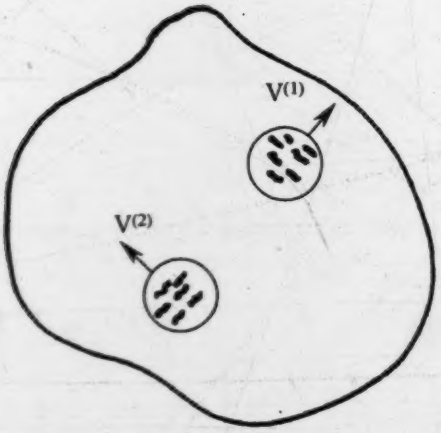

Figure 4.1 A solid containing two sets of oriented crack arrays (adapted from Talreja [44]).

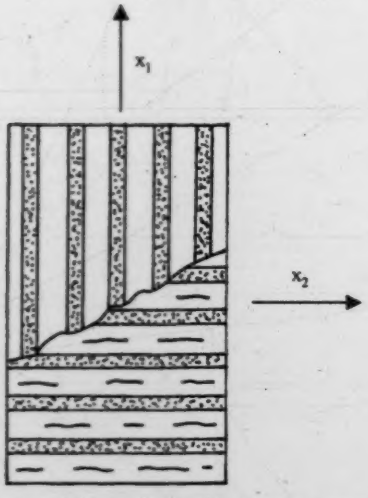

Figure 4.2 A cross-ply laminate with cracks in the transverse plies (adapted from Talreja [44]).

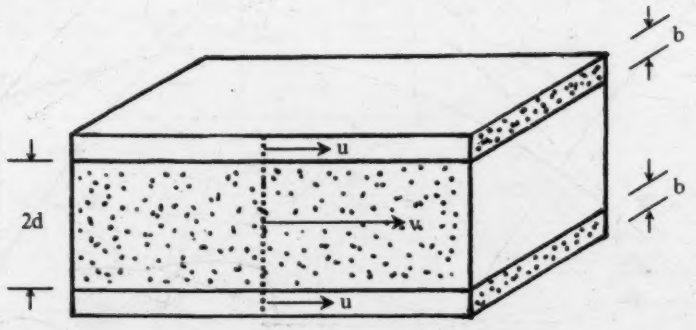

Figure 4.3 Symmetric cross-ply laminate under axial load (adapted from [49]).

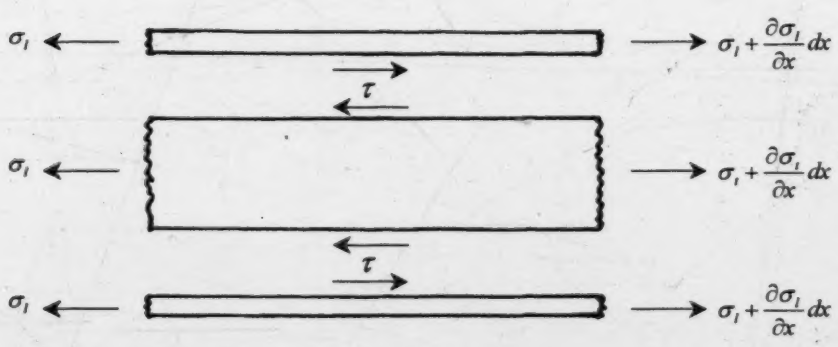

Figure 4.4 Stresses on individual layers of the laminate (adapted from Laws and Dvorak [49]).

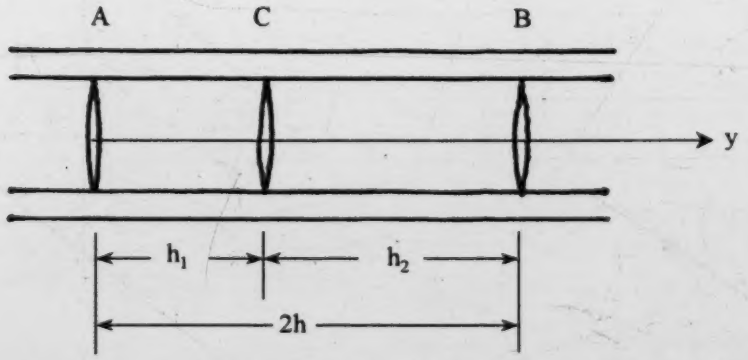

Figure 4.5 Two adjacent transverse cracks in the 90° plies (adapted from Laws and Dvorak [49]).

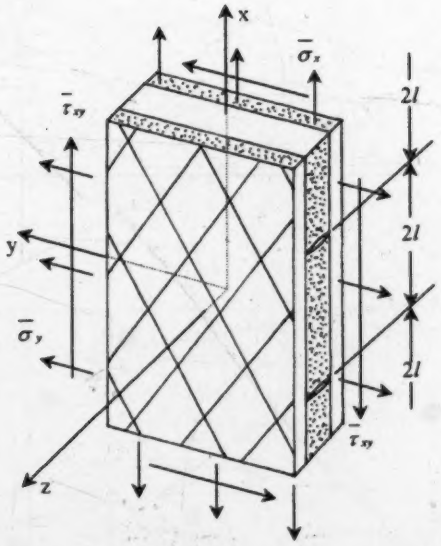

Figure 4.6 Composite laminate containing a cracked ply and subject to in-plane loading (adapted from Nuismer and Tan [37]).

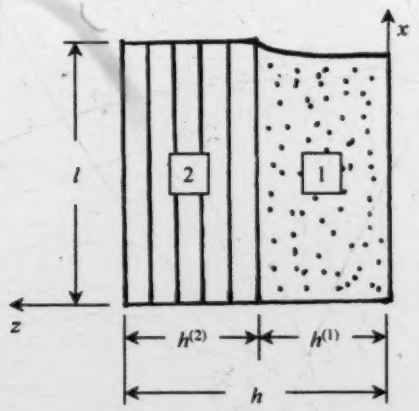

Figure 4.7 One quarter of the composite laminate unit cell (adapted from Nuismer and Tan [37]).

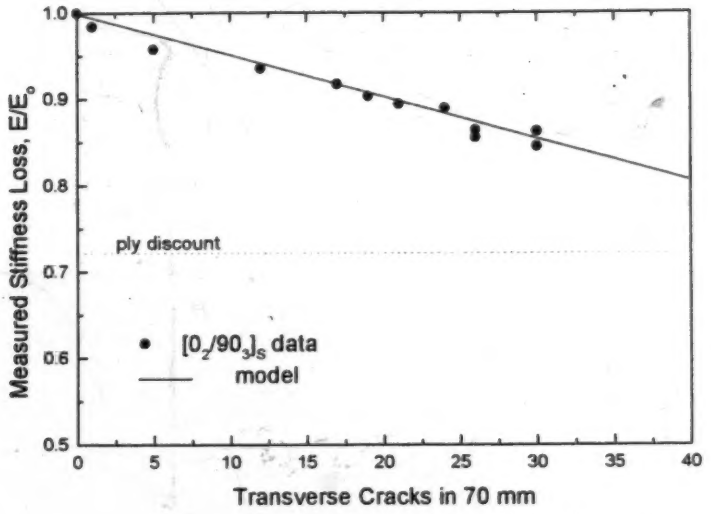

Figure 4.8 Stiffness reduction of two $[0_2/90_3]_S$ specimens tested at 10^{-4} s^{-1} strain rate plotted with internal variable models.

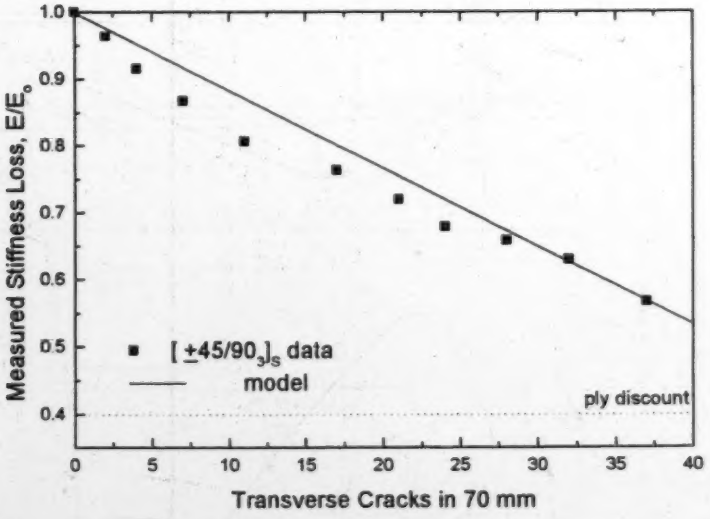

Figure 4.9 Stiffness reduction of a $[\pm45/90_3]_S$ specimens tested at 10^{-4} s^{-1} strain rate plotted with internal variable models.

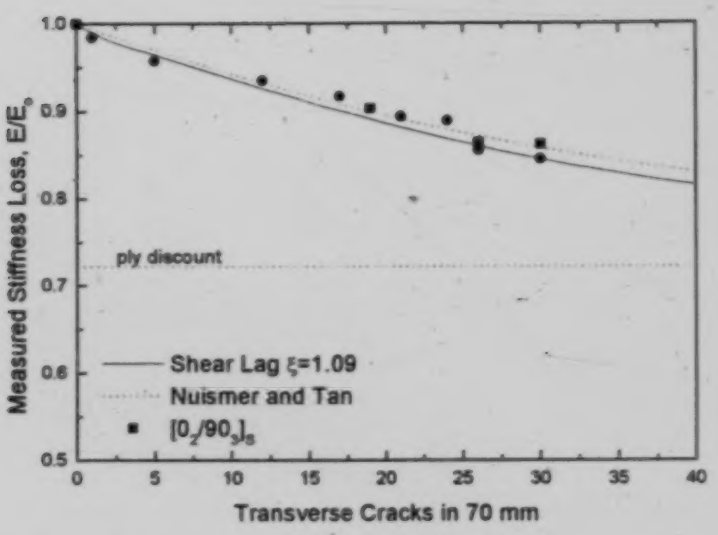

Figure 4.10 Stiffness reduction of a $[0_2/90_3]_s$ specimens tested at 10^{-4} s^{-1} strain rate plotted with shear lag and elastic element models.

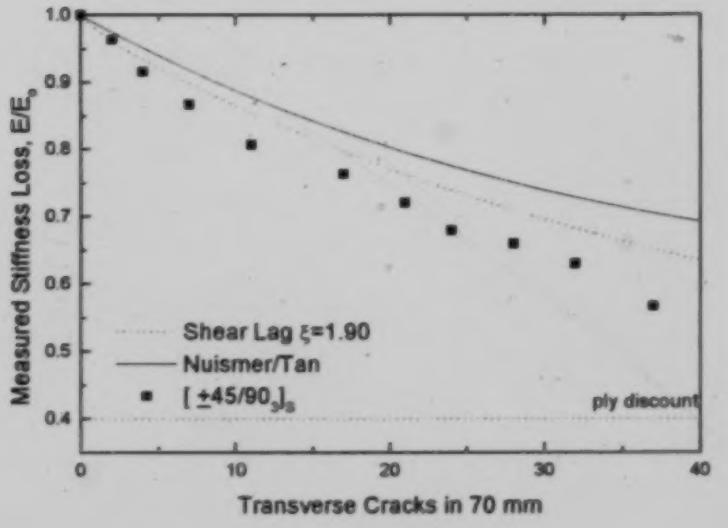

Figure 4.11 Stiffness reduction of a $[\pm 45/90_3]_s$ specimens tested at 10^{-4} s^{-1} strain rate plotted with shear lag and elastic element models.

5. PROGRESSIVE DAMAGE AND THE IMPLEMENTATION OF A FAILURE CRITERION

The foundations of every design are based on understanding the mechanisms that will lead to failure. Design failure has more than one definition; it may be the elastic limit, functional failure, localized failure or total failure. Intrinsic to each design is the knowledge, or assumption, of the crucial failure mechanism.

Failure of advanced composite materials is a complex topic. In the case of fibre reinforced composites, the combination of high-strength elastic glass fibres and low-strength viscoelastic epoxy matrix create a material that is lightweight, strong and versatile. The damage resistance of the combination is better than that of each isolated component. The behaviour of the composite material is difficult to describe even though the characteristics of constituents are well known.

There are several different failure modes present in fibre composites: fibre rupture, fibre/matrix debonding, hygrothermal degradation and matrix cracking. Fibre rupture is usually associated with ultimate failure since fibres are most often the strongest component of the composite. If some fibres are oriented near the loading axis and if the failure is not totally dominated by shearing between fibres, then some fibres must fail before complete separation. On the other hand, fibre debonding is a microscopic effect and its effect on the overall behaviour is usually ignored. In most cases, it is assumed that the amount of debonding remains unchanged during the life of the composite and is thus accounted for during the measurement of the initial properties.

In addition to the two fibre failure modes, there are two matrix cracking modes. Intralaminar cracking appears as cracks within each laminate ply. These cracks run through the thickness of the laminate and may be arrested by fibres that intersect the crack path (Fig. 5.1). The effect of intralaminar cracking is to cause stress relaxation in the small region near the crack. Load is returned to the ply via shear stress and the original stress distribution is

unaffected at large distances from the crack, usually 5-10 ply thicknesses. Multiple intralaminar cracks can be tolerated before ultimate failure.

Interlaminar cracking, also known as delamination, refers to cracking between plies and is often initiated by the tips of intralaminar cracks. Interlaminar cracks separate layers, prevent even load distribution and often lead to ultimate failure because they are very difficult cracks to arrest.

In a typical multidirectional laminate, all of these failure modes may be present and behaving independently. It is physically unreasonable to think that all failure modes can be modelled with the same failure criterion. In a full treatment of failure, all modes would have to be studied simultaneously. At present, the accumulated research has not progresses enough to accomplish this task.

The overall goal of this research project is to develop design criteria which can define functional failure. In many cases, leakage of pressure retaining composite structures leading to functional failure will be caused by matrix cracking at strains well below the ultimate failure strain of the composite material. This study was therefore narrowed to exclude all but intraply matrix cracking. One can isolate the intraply matrix cracking by making $[\pm\theta/90_n]_s$ specimens. If n is greater than 2, this type of specimen will be vulnerable to matrix cracking in the central 90° layers because the fibres are oriented perpendicular to the applied load. If cracks develop in these layers, no nearby fibres bridge the crack path and the crack runs unimpeded until it reaches the constraining plies.

During testing of $[\pm\theta/90_n]_s$ specimens, one can observe multiple matrix cracking in the 90° plies. These cracks occur before other forms of observable damage and the effect of the cracks is limited to the transverse plies (Section 3.4). In this way, one can isolate the effect of transverse matrix cracks on the overall performance of the laminate.

Chapter 4 evaluated several stress analyses and provided the stress and strain distribution and the stiffness reduction of the laminate. While the stiffness reduction may be very informative and useful in design, it does not provide any information regarding the onset or accumulation of crack damage. As Figure 5.2 shows, the important information required by design, including the stress-strain curve and the crack accumulation curves, can only be determined once a failure criterion is implemented.

The purpose of this chapter is to implement and evaluate possible failure criteria. Failure criteria can be divided into strength of material approaches or energy based fracture mechanics approaches. It will be shown that strength of material criteria are not suitable for composite materials applications. Fracture mechanics criteria, based on the more physically realistic cracking phenomenon, fare better in the analysis and can be used independent of experimental calibration. However, fracture mechanics failure criteria do not produce acceptable stress-strain or crack accumulation predictions in all cases even with an acceptable stress analysis.

5.1 BACKGROUND

At some point in the design process, it will be necessary to determine the appropriate load that a structure can withstand. It is crucial to understand the relationship between the dominant failure mode and the critical parameter associated with that mode [61]. Two distinct failure criteria, the strength of materials approach and fracture mechanics, will be evaluated here with respect to both the physics and effects of matrix failure. The order of the discussion will mimic the order of sophistication of the techniques; the simpler strength of materials approach will be discussed before fracture mechanics.

5.1.1 Strength of Materials Failure Criteria

Whenever design stresses are compared with ultimate, allowable or working stresses, a strength of materials approach is being used. The critical parameters which signal the

onset of failure may be the stress, strain, displacement, or load. Interaction between these parameters is also important and combinations of these critical parameters are also used.

This type of analysis can be used to find the maximum load a structural member can carry. A simple example is a 27 mm OD steel cylinder which is to act as a tension member. The stress along the longitudinal axis of the cylinder can be found using elementary stress analysis

$$\sigma = \frac{Load}{Area} = \frac{P}{A}$$

If the yield strength is 175 MPa, the maximum load which can be applied is

$$P_{max} = \sigma_{yield} A = (175MPa)\frac{\pi}{4}(27mm)^2 = 100kN$$

In this case, the failure criterion is the yield strength obtained from numerous experimental tests. No attempt is made to calculate this strength analytically because the value itself is sufficient to model the behaviour of the column. For simple static loading of homogeneous members, this type of analysis is effective.

In most composite laminate cases, a strength of materials failure criterion is based on ply failure. Since damage accumulates differently in each ply, failure modes and ply strength may vary through the laminate and failures will occur in each ply at different times. The first sign of damage will occur in one of the weaker plies and is called first ply failure. Ultimate failure of the laminate occurs once last ply failure is reached [28].

In the case of composite laminates with transverse cracking, first ply failure stresses and strains have been used [17, 32-35, 41-42, 44, 62]. Typically, one measures the stress and strain at which a transverse crack first appears in a unidirectional 90° laminate. This value becomes the transverse strength of the ply. In a similar manner, the ultimate longitudinal

strength can be determined by experimental testing of a 0° laminate. Once these parameters are known, they are used to determine failure in each ply. If the calculated stress or strain in a ply exceeds that of the measured ultimate value, one assumes that failure has occurred. As we will see below, however, the *in-situ* strength of the ply in a multidirectional laminate is not the same as the isolated ply strength.

With this in mind, it should be possible to measure the first ply failure strain of the $[\pm\theta/90_3]_s$ specimens used in this study. The total strain on the laminate is the sum of the applied strain and the residual thermal strain from the high temperature curing cycle.

$$\varepsilon_{tot} = \varepsilon_{thermal} + \varepsilon_{applied} \tag{5.1}$$

Using the results of Section 2.8 (Figs. 2.7-2.8) to characterize the thermal strains due to curing and Section 3.2.2 (Figs. 3.8-3.11) to determine the applied strains at which cracking first occurs, the calculated first ply failure can be determined (Table 5.1). The applied strains listed in the table are estimated from the experimental data shown in Figures 3.8-3.11.

Specimen Geometry	Calculated Residual Strain in 90° plies	Applied Strain at which cracking first occurs	Calculated First Ply Failure Strain
$[0_2/90_3]_s$	0.11	0.50	0.61
$[\pm 20/90_3]_s$	0.11	0.50	0.61
$[\pm 45/90_3]_s$	0.06	0.50	0.56
$[\pm 55/90_3]_s$	0.04	0.65	0.69

Table 5.1 Calculated First Ply Failure Strains from CLT.

The simple analysis described above does not produce a unique value for first ply failure strain. The value for the 0° and 20° constraining plies are similar which is to be

expected considering the similarity of lay-ups. The values for the 45° and 55° specimen differ by 18%.

Similar difficulties with defining a first ply failure stress were reported by Crossman and Wang [41] and Flaggs and Kural [42]. Flaggs and Kural performed tests on $[0_2/90_n]_s$, $[\pm 30/90_n]_s$ and $[\pm 60/90_n]_s$ specimens with n=1,2,4,8. They measured the *in- situ* transverse lamina strength based on their experimental determination of first ply failure strain and calculation of residual stresses from the effective stress free temperature. It was found that the transverse stress at the onset of transverse cracking was functions of both laminate orientation ('constraint effect') and transverse ply thickness ('thickness effect'). Crossman and Wang [41] tested $[\pm 25/90_n]_s$ and $[\pm 25_2/90_n]_s$ specimens with n=0.5, 1, 2, 3, 4, 6, 8. The observed tensile strain for transverse cracking, delamination and ultimate failure was found to be a function of the number of 90° plies in the laminate. The calculated thermal and mechanical stress at the onset of transverse cracking changed as n varied and was significantly higher than the unidirectional value. In discussing these two works, Hartsmith [40] pointed out that there is no single replacement strength suitable for use in a stress-interaction formula when applied to multidirectional laminates. Even for the similar specimens of Table 5.1, the results show that the constraint effect invalidates the strength of material failure criterion.

The strength of materials criterion would be the simplest failure criterion to use but the thickness and the constraint effects require variable ply failure strengths. As a result, the strength of materials approach to failure in composite laminates is inappropriate for modelling progressive damage because there is no unique value for the ply strength.

5.1.2 Fracture Mechanics Failure Criteria

In contrast to the strength of materials approach, fracture mechanics is based on fundamental physical and thermodynamic principles. The major advantage of fracture

mechanics is that the growth or presence of a crack depends on the geometry of the crack itself. As a result, thickness and constraint effects are accountable.

Fracture mechanics is a fully developed topic and several methods exist to model the cracking behaviour. These include cracks in undamaged material, crack growth from flaws or preexisting cracks, stationary cracks and dynamic cracking. While all of these phenomena may be present in composite laminates, this study will only consider cracking of undamaged material, i.e. material without preexisting flaws or microcracks. Limiting the analysis in this way does not compromise the analysis because experimental observations detailed in Chapter 2 show that cracks appearing during monotonic testing immediately propagate across the specimen. Further fatigue cracking and angle ply cracking may require a more advanced fracture mechanics treatment.

A matrix crack is essentially a crack in a brittle material. The matrix, which may have some viscoelastic characteristics if isolated, contains a high density of elastic glass fibres that limit the 'inelastic zone' to a small radius at the crack tip. If the inelastic deformation is small or negligible, the material can be modelled with an elastic analysis. For brittle materials, the Griffith energy balance is the simplest approach. The Griffith criterion states that fracture will occur when the energy available for crack growth is sufficient to overcome the resistance of the material [26]. The material resistance may include inelastic work or other types of energy dissipation associated with a propagating crack, but for a perfectly brittle crack would include primarily the surface energy.

A simple fracture mechanics problem is to calculate the failure of a infinitely wide plate containing a crack of length $2a$ [26]. The potential energy supplied by the internal strain energy is

$$\Pi_0 = \Pi - \frac{\pi\sigma^2 A^2}{4EB}$$

where Π_0 is the potential energy of an uncracked plate, A is the crack area ($2aB$), and B is the plate thickness. The cracks have an associated surface energy

$$W_s = 2A\gamma_s$$

where γ_s is the specific surface energy. In order for the crack to grow, the rate of decrease in the elastic potential energy must be equal to the rate of increase in the surface energy of the cracks.

$$-\frac{d\Pi}{dA} = \frac{dW_s}{dA}$$

The fracture stress of the plate can then be determined.

$$\sigma_f = \left(\frac{2E\gamma_s}{\pi a}\right)$$

It is important to note that the fracture mechanics approach relies on a failure criterion derived from physical principles (γ_s). In addition, the failure criterion is related to the stress analysis via the second law of thermodynamics (equilibrium) which makes the analysis more physically rigorous.

The following sections use the strength of materials failure criteria and fracture mechanics to model the stress-strain curve and progressive damage. To begin the discussion, the strength of materials criterion will be used with Classical Laminate Theory to model the stress-strain response. The fracture mechanics approach will be used later to introduce damage into the shear lag and Nuismer/Tan analyses.

5.2 CLASSICAL LAMINATE AND PLY DISCOUNT THEORY

The most notable experimental observation from the stress-strain curves is that all the specimens displayed a bilinear response. An approach has been developed using Classical Laminate Theory (CLT) with ply discount to model this bilinear response. The procedure is completed in two steps. First the original stiffness is calculated which determines the response until the onset of damage. After cracking has occurred in a ply, the ply stiffness is discounted and the stiffness recalculated.

The effect of a crack is to eliminate the stiffness contribution of the cracked ply to the overall laminate stiffness. It is assumed that the transverse stiffness, E_2, and the shear stiffness, G_{12}, of the cracked plies is zero. The laminate stiffness modulus, E_x, is then recalculated from the laminate stiffness matrix $[Q]_{12}$ (Section 4.2.1.2, eq. 4.5). To create a stress-strain curve, the initial stiffness is plotted until the onset of damage (in this case 0.6%) at which point the discounted stiffness is plotted. The CLT with ply discount model correlation is shown in Figures 5.3-5.6. The data shown is for the strain rate of 10^{-4}.

The correlation is very good for all specimen geometries. As one would expect, the model provides an accurate prediction for the fibre-dominated specimens (0° and ±20°) until final failure. For the matrix dominated specimens (±45° and ±55°) the post-knee prediction is not as good. This can be attributed to damage in the constraining plies. As the strain exceeded 1%, ligament-type cracks were observed (Fig. 3.18) in the constraining plies. This damage is not included in the ply discount model and leads to an overestimation of specimen stiffness.

The accuracy of the correlation between CLT with ply discount and mechanical performance is quite remarkable considering the simplicity of the approach. The major drawback of this method is that one cannot determine the knee-point in the stress-strain curve without *a priori* experimental tests on similar laminates. In addition, the ply discount method assumes that a single crack anywhere along the length of the specimen discounts the

stiffness of the entire ply along the entire length from the laminate stiffness matrix. This is neither physically realistic nor informative to the designer who needs information on damage accumulation. For this reason, a more advanced model that can predict both damage development and stiffness loss was pursued.

5.3 CRACK PROGRESSION CALCULATED FROM SHEAR LAG THEORY

Section 4.2.3 described the stress analysis that can be accomplished with a shear lag approach [49]. The approach is identified with the assumption that the shear stress is proportional to the relative displacement between the transverse and constraining plies. The analysis yields that the axial stress is described by the formula shown below

$$\sigma_a = E_0\left\{\varepsilon_a - \frac{\beta}{\xi}\frac{d\sigma_t^R}{bE_t}\tanh\frac{\xi}{\beta}\right\}\left\{1+\frac{\beta}{\xi}\frac{dE_t}{bE_t}\tanh\frac{\xi}{\beta}\right\}^{-1} \tag{4.17}$$

which is the effective stress-strain relation for the cracked laminate. The derivation followed by Laws and Dvorak formulates the strain energy in terms of applied stress. For this reason, the stress is determined as a function of crack spacing and the stress is plotted against the crack density to compare the theory to experimental results.

An energy based failure criterion is used to add progressive damage into the model. Consider Figure 5.7 where state 1 has cracks at A and B. At a certain load, a new crack will develop at C partway between A and B. The total energy per unit width released by the introduction of the crack at C is the work done by the applied loads minus the increase in strain energy

$$SE = \frac{2d^2(b+d)E_0}{\xi bE_t E_t}\left(\sigma_t^R + \frac{E_t}{E_0}\sigma_a\right)^2\left\{\tanh\frac{\xi h_1}{2d} + \tanh\frac{\xi h_2}{2d} - \tanh\frac{\xi h}{d}\right\} \tag{5.2}$$

The energy release rate, G is related to the change in energy due to the introduction of a new crack

$$SE = 2dG$$

from the two previous equations, the applied stress facilitating the new crack at C can be determined

$$\sigma_a(h_1,h_2) = \sqrt{\frac{G\xi bE_1E_0}{d(b+d)E_t}\left\{\tanh\frac{\xi h_1}{2d}+\tanh\frac{\xi h_2}{2d}-\tanh\frac{\xi h}{d}\right\}} - \frac{E_0}{E_t}\sigma_t^R \tag{5.3}$$

The stress is a function of the location of the crack, h_1 and h_2. In order to determine the location of crack C in the ligament, a probability density function for the site of crack C is defined. In a laminate which already contains cracks, the expected value of the applied stress to cause additional cracking, $E[\sigma_a(\beta)]$, is

$$E[\sigma_a(\beta)] = \int_0^{2h} p(y)\sigma_a(y)dy \tag{5.4}$$

where $\sigma_a(y)$ is the applied stress to cause an additional crack at location y. Laws and Dvorak [49] have three possible alternatives for the site of the new crack. Case 1 is for the next crack occurring at the midpoint of the unbroken ligament. In this case, h_1 is equal to h_2 and

$$p(y) = \delta(y-h)$$

which is the Dirac delta function. In Case 1 we obtain directly ($h_1 = h_2 = h$)

$$\sigma_a(h) = -\frac{E_0}{E_t}\sigma_t^R + \sqrt{\frac{\frac{G\xi b E_t E_0}{d(b+d)E_t}}{\left\{2\tanh\frac{\xi h}{2d} - \tanh\frac{\xi h}{d}\right\}}} \tag{5.5}$$

Case 2 is the possibility that all crack locations in the ligament are equally probable, giving

$$p(y) = \frac{1}{2h}$$

and Case 3 assumes that the probability is proportional to the stress in the transverse ply

$$p(y) \propto \sigma_t(y)$$

Both Case 2 and 3 require a numerical solution to find the applied stress.

Before proceeding further with this analysis, it is important to emphasize a limitation involved with the shear lag theory. In Section 4.2.3.1, it was shown that the shear lag parameter, ξ, was calculated from the standard geometric and material data (b, d, E_t, E_t, and G_c), two values to be determined from CLT (σ_t^R and E_0), and σ_a^{fpf}, the first ply failure stress of the laminate under study (equation 4.19). During an experiment, the first ply failure stress may be determined easily from direct observation but this requires that a test be done for every laminate geometry to be studied. The model, as described by Laws and Dvorak [49], is thus a correlation model which does not predict material behaviour. A complete model should predict the first ply failure strength and a method was sought to provide the shear lag analysis with a calculated first ply failure stress.

In the next section, the Nuismer/Tan approximate elasticity analysis will be described. A byproduct of the analysis is that the first ply failure strain is calculated explicitly

(equation 5.8). This strain can be expressed as a stress through the constitutive equations already developed (equation 4.17) and was used to determine ξ in the shear lag model. Once this modification was made, the shear lag model could predict the complete response of the $[\pm\theta/90_3]_S$ specimens and any $[\pm\theta_n/90_m]_S$ laminate. As a final note of some assurance, the calculated first ply failure strains calculated from the shear lag constitutive equations were within 1% of the original Nuismer/Tan first ply failure strain.

Figures 5.8-5.11 compare the experimental data with the modified shear lag predictions for each of the three cases. The experimental data was replotted by correlating the number of cracks to the measured stress via the applied strain. From the figures, one may extract the first ply failure stress used to calculate the shear lag parameter by noting the curve intercept on the horizontal axis. The stress values range from 132 MPa for $\theta=0°$ to 65 MPa for $\theta=55°$. It should be noted that by increasing or decreasing the first ply failure stress, the curves may be shifted along the horizontal axis. In this way, the model can be adjusted to fit the experimental data very well but the prediction now relies on experimental data for calibration. In addition, the first ply failure stresses plotted in the figures are slightly different for each case. This is believed to result from either truncation or round-off error involved in the computation of the probability integral and does not originate from the shear lag theory.

The predictions of the modified model diverge after the first ply failure stress for the three cases. The Case 1 prediction, based on cracks only occurring in the center of the ligament ($h_1=h_2$), overestimates the number of cracks which exist at any stress level. This is expected because the axial stress in the transverse plies is greatest in the center of the ligament which minimizes the applied stress required to cause a crack. In reality, the crack may not occur at this point if conditions are not favourable to crack growth (i.e. no flaw may exist there) and more applied stress may be required to cause cracking. Case 2, which assumes that the crack probability is equal along the length of the ligament, underestimates the number of cracks. This error occurs because the equal probability distribution is physically unrealistic. In this case, cracks are equally likely to occur in the center of the

laminate or immediately beside an existing crack. The stresses required to create two closely spaced cracks is very large and this leads to an overestimation of the applied stress required to cause cracking. Case 3, which assumes that the probability of a crack forming is proportional to the axial stress in the transverse ply, is the most physically realistic case and provides the best duplication of the experimental data trends. This affirms that the physics are important to the correct modelling of the problem. If the physics are not important, one should question the ability of the model to correctly address the problem. The Case 3 results fall between the two extreme cases previously mentioned which should be expected because the Case 3 probability distribution is between the Case 1 and Case 2 distribution. Case 3 provides the best predictions for all the experimental results with the exception of the $[\pm 55/90_3]_S$ specimens (Fig. 5.11) which may be modelled best by the more vertical Case 1 curve. This behaviour, essentially a failure strength of 70 MPa, is unique to the $[\pm 55/90_3]_S$ specimens and the Case 3 prediction is still fairly good. Due to the superior performance of the Case 3 predictions, Case 1 and Case 2 predictions will be omitted from upcoming plots and discussions.

In the case of the $[0_2/90_3]_S$ specimens (Fig. 5.8), the first ply failure stress is close to the experimental value and the trend of the data is duplicated by the Case 3 prediction. Figure 5.9 shows that the $[\pm 20/90_3]_S$ data is modelled well although the first ply failure stress predicted by the modified shear lag method appears to be larger than the experimentally observed value. In the case of the $[\pm 45/90_3]_S$ specimens, the modified model correctly predicts the first ply failure stress but then overestimates the number of cracks which will be present at any subsequent stress level. The shear lag prediction for the $[\pm 55/90_3]_S$ specimens indicates that stress must increase to initiate cracks but the data clearly shows that increased numbers of cracks occur as the stress is maintained at approximately 70 MPa. These errors are minor and overall shear lag predictions for crack progression as a function of applied stress are deemed to be very good.

5.4 CRACK PROGRESSION CALCULATED FROM THE ELASTIC ELEMENT MODEL OF NUISMER/TAN

Section 4.2.4 described an approximate elasticity approach to determine the elastic modulus, E_x, of a unit cell of length l. The next step in the analysis is to predict the strain at which each cracking event occurs. In this way, strain can be related to crack spacing, l, and elastic modulus, $E_x(l)$. Finally, from the strain and the elastic modulus, stress can be calculated and a stress-strain curve created. The derivation followed by Nuismer and Tan formulates the fracture energy in terms of applied strain. For this reason, the strain is determined as a function of element length and crack density *vs.* strain is plotted to compare theory to experimental results.

Progressive damage is introduced with an energy-based fracture mechanics criterion. The Nuismer/Tan model is based on a sequence of cracking that occurs in the center of the unit cell. As a result, the crack density doubles for each subsequent damage state and the crack spacing is uniform. The failure strain is found by comparing the elastic energy before fracture with the elastic energy of the unit cell after a fracture has bisected the transverse plies. Once this energy has reached a critical level set by the specific fracture energy, γ_T, a fracture has occurred.

Assuming elastic behaviour, the energy stored in a quarter cell (Fig. 4.7) is

$$U = Area \times \frac{\sigma\varepsilon}{2}$$

$$U = \frac{\bar{h}l}{2} E_x(l)\bar{\varepsilon}^2$$

where $2l$ is the crack spacing and $2h$ is the width of the specimen. From the energy balance consideration, the strain energy released from one damaged state to another is equal to the surface energy of the new crack surfaces. Just prior to a crack initiation, the strain energy of the original unit cell (state 0) is

$$U_o = \frac{\bar{h}l}{2} E_x(l) \bar{\varepsilon}_1^{\,2}$$

After fracture, the length of the unit cell is now $l/2$. The elastic energy of state 1 is

$$U_1 = \frac{\bar{h}\frac{l}{2}}{2} E_x(\frac{l}{2}) \bar{\varepsilon}_1^{\,2} \tag{5.6}$$

Since the four quarter cells have bisected to become eight cells, the total energy in the region is

$$\Delta U = 4U_o - 8U_1$$

$$\Delta U = 2\bar{h}l\left[E_x(l) - E_x(\frac{l}{2}) \right] \bar{\varepsilon}_1^{\,2} = 4h^{(l)}\gamma_T \tag{5.7}$$

where $4h^{(l)}\gamma_T$ is the energy required to make two new crack surfaces. This expression can be arranged to solve for the strain that initiates cracks, ε_1

$$\bar{\varepsilon}_1 = \sqrt{\frac{2h^{(l)}\gamma_T}{\bar{h}l}\left[\frac{1}{E_x(l) - E_x(\frac{l}{2})} \right]} \tag{5.8}$$

Once the elastic modulii for all quarter cells are known, the failure strains can be determined. The measured failure strain is the difference between the total failure strain and residual thermal strain

$$\bar{\varepsilon}_M = \bar{\varepsilon}_1 - \bar{\varepsilon}_N \tag{5.9}$$

where the residual thermal strain is given by

$$\bar{\varepsilon}_N = \frac{\bar{\sigma}_N}{E_x} = \frac{-Q_2\left(\frac{\bar{A}_{12}\bar{\sigma}_N}{\bar{A}_{22}E_x} - \frac{\bar{\sigma}_{yN}}{\bar{A}_{22}}\right) - \sigma_{xN}^{(1)} + \frac{Q_{11}^{(1)}}{Q_{11}^{(2)}}\sigma_{xN}^{(2)}}{\left[Q_1 E_x - Q_2\frac{\bar{A}_{12}}{\bar{A}_{22}}\right]} \tag{5.10}$$

Q_1 and Q_2 are stiffness constants and all other variables are defined in equations (4.23). Equations (4.23) show that the A_{ij} and the σ_{ij} change as the average crack spacing increases. Thus, equation (5.10) calculates the residual strains present in the laminate as a function of the cracking state and reveals that the intensity of the residual strain decreases as the number of cracks increases. The Nuismer and Tan formulation is the only model to accounts for this strain relaxation.

In order to calculate the stress during cracking, the crack density, ρ, is $1/2l$ and

$$\sigma_{prefracture} = E_x(l)\bar{\varepsilon}_1$$
$$\sigma_{postfracture} = E_x(l/2)\bar{\varepsilon}_1 \tag{5.11}$$

5.4.1 Progressive Damage Predictions

5.4.1.1 First Ply Failure Strains

Calculation of the first ply failure strains from the basic material constants is a major advantage of using a fracture mechanics approach. By including the value for the specific fracture energy, γ_T, in the analysis, one can predict the onset of cracking without any experimental results (the specific fracture energy was measured independently as described in Section 2.5). Table 5.2 shows the calculated and observed first ply failure strains. The calculated strains are closely grouped around 0.6% while the observed values are 0.5% for all but the ±55° specimens. The average difference between the calculated and observed values

Specimen Geometry	Calculated Total Failure Strain, ε_1	Calculated Initial Residual Strain from (5.10), ε_N	Calculated First Ply Failure Strain, ε_M	Observed First Ply Failure Strain
$[0_2/90_3]_S$	0.72	0.11	0.61	0.50
$[\pm 20/90_3]_S$	0.71	0.10	0.61	0.50
$[\pm 45/90_3]_S$	0.66	0.06	0.60	0.50
$[\pm 55/90_3]_S$	0.64	0.04	0.60	0.65

Table 5.2 Calculated First Ply Failure Strains from Elastic Element Model.

for the 0°, 20°, and 45° specimens is 15%. While this model can provide a theoretical first ply failure strain, the results should be closer to experiment. Most interesting is that as the constraining angle increases, the calculated strain value decreases while the observed value increases.

The reason for these discrepancies is not apparent. Comparing Tables 5.1 and 5.2 shows that the calculated residual strains for both the CLT and elastic element models are the same except for the $[\pm 20/90_3]_S$ specimens (which differs slightly due to the slightly different method of calculating residual strains, equations 4.4 and 5.10). The error must then arise from the total failure strain, ε_1, and the determination of either the specific fracture energy or the elastic element stiffness loss, $E(l)$. A parametric exercise showed that the first ply failure strain can be decreased by decreasing the specific fracture energy value. However, after this adjustment the model reduces to curve fitting which defeats the purpose of being able to predict cracking without experimental data.

5.4.1.2 Progressive Failure

The accumulation of cracks as a function of the applied strain is plotted in Figures 5.12-5.15. The figures show that experimental scatter makes determining the first ply failure

strain difficult. The curves start at the first ply failure strain and predict that cracks should accumulate rapidly as the strain is increased. As noted above, the first ply failure predictions are greater than the experimental observations.

The two curves in each figure result from two calculated strain values for the same crack state: the pre-fracture and post-fracture strain (Fig. 5.16). A true plot of the model would be a series of horizontal lines connecting the two strains of each crack state. However, the present figures were plotted to show the extremes of both calculated strains. The original reference [38] suggests that the two strain values should be averaged before plotting but this is merely a curve in the middle of post-fracture and pre-fracture strains.

The model does not provide adequate predictions of the progressive cracking behaviour. In every case shown in Figures 5.12-5.15, the first ply failure strain and the predicted number of cracks is too large for a given strain value. This is a curious situation because the model first overestimates and then underestimates the resistance to cracking. Again, the cause of this is not apparent. The model relies on the stiffness reduction and specific fracture energy to predict cracking. Chapter 4 (Section 4.3) showed that the stiffness reduction of the model matched experiments, particularly for stiff constraining layers. One can change the value of the specific fracture energy but this only results in a horizontal shifting and does not bend the curve closer to the data trend. The errors of the model become more apparent as the constraining ply angle increases and the results for the $[\pm 55/90_3]_s$ specimens are the least accurate.

5.5 STRESS-STRAIN RELATION PREDICTIONS

A stress-strain relation provides very important information. Once the stiffness reduction has been completed and the failure stresses or strains calculated, the stress-strain curve can be modelled. In the shear lag approach, the effective stress-strain relation is expressed explicitly from the associated displacements. Once the set of stresses to cause additional cracking is known (eq. 5.5), the stress-strain response follows from equation 4.17.

In the Nuismer/Tan approach, the set of failure strains is computed (equation 5.8) and the stresses are obtained from the stiffness modulii of the elastic elements of varying length (equation 4.25). To produce a set of stresses, one simply multiplies the failure strain by the element stiffness corresponding to that crack density. Note that in both cases, the stress analysis of Chapter 4 is used in conjunction with the failure criterion of Chapter 5. Figures 5.17-5.20 show the shear lag and Nuismer/Tan stress-strain predictions.

The shear lag model used with the Case 3 crack spacing distribution provides good stress-strain response for the 0° and ±20° constraining angels. The knee point in the curve matches the experimental data well and the post-knee prediction is good. As the constraining ply angles increase, the ability of the model to provide an accurate prediction diminishes. The stress-strain prediction for the ±45° and ±55° specimens is poor in the post-knee regime likely due to non-linear effects in the constraining plies observed during the experiments.

The Nuismer/Tan method does not contain an explicit stress-strain formula; it produces a stress-strain curve by relating strains to stresses via the set of calculated quarter unit cell elastic stiffnesses. This situation would not cause a problem but the number of cracks doubles for every crack state and leads to coarse resolution and large strain increases after the appearance of new cracks. The large differences in strain are apparent in the final results and produce an ambiguous stress-strain curve. It should be noted that this situation does occur in experiments but cracks occur individually and the problem of coarse resolution is avoided. The original authors [38] argue that the median strain at each crack state should be used to produce plots but this hides the actual mechanics of the model.

A schematic of a Nuismer/Tan stress-strain curve prediction is shown in Figure 5.21 (the schematic is actually the $[\pm 55/90_3]_s$ stress-strain curve with the data points removed). The effect of the coarse resolution is apparent as the curves diverge quite rapidly after first ply failure. To begin creating the stress-strain curve, the initial modulus is multiplied by the first ply failure strain, $\varepsilon^{(0)}$. The gives a value of the pre-fracture stress of state 1, the first

damaged state, and is essentially the same as a Classical Laminate Theory prediction because no data points exist in the elastic region. Once the laminate has cracked for the first time, the stress drops due to the drop in stiffness. The post-fracture stress of state (*i*) is found by multiplying $\varepsilon^{(i)}$ by the stiffness of state *(i+1)*. Similarly, the pre-fracture stress of state *(i+1)* is found from multiplying the failure strain, $\varepsilon^{(i+1)}$, by the stiffness of state *(i+1)*. This procedure, illustrated by Figure 5.21, continues with ever increasing strain intervals between $\varepsilon^{(i)}$ and $\varepsilon^{(i+1)}$.

The original reference [38] suggests that the average of these two values be used as the 'average load' for two reasons: (1) experimental data lie in a scatter band between the initiation and completion of a damage state, and (2) in reality the materials are inhomogeneous. They suggest that fibre clustering and unequal crack spacing can be accounted for in this way.

Averaging the two stresses in this way disguises the limitations and actual mechanics of the model. It can be observed that as the number of cracks increases, the two curves diverge. This occurs because of the assumption that the quarter unit cell represents the entire laminate. If single cracks could be added to the analysis, the step size would remain the same throughout the procedure. The average load suggested by Nuismer and Tan was not used in this study so that the true behaviour of the model could be observed.

The stress-strain predictions of the model (Figs. 5.17-20) appear to be accurate for low strain values. For all laminate geometries, the initial modulus is accurately predicted from the model. The initial response is the same as for the CLT prediction (Figs. 5.3-6). The curves of the stiffer 0° and ±20° specimens follow the experimental data with the two curves acting almost like scatter bands for the test data. As the angle of the constraining plies increases to ±45° and ±55°, the model predictions begin to deteriorate for the same reason that the elastic element stiffness reduction and crack progression predictions were poor. The additional constraining ply damage experienced by the high θ specimens is

unaccountable in the model and leads to an overestimation of the material strength. However, the model does provide a good prediction of the stress-strain curve for strains below 1%. The poor stress-strain predictions for the ±45° and ±55° specimens will lead to problems later when the two models are compared (Section 5.6).

5.6 COMPARING SHEAR LAG AND NUISMER/TAN MODEL PREDICTIONS

The shear lag and approximate elasticity models are difficult to compare. The shear lag approach is designed to determine the stress required to cause additional cracking. The approximate elasticity model calculates the strain required to make the fracture in the middle of an element energetically favourable. In order to compare the models, the failure stresses or strains must be transformed and therefore cannot be compared independent of the corresponding constitutive equations.

Figure 5.22 shows the relationship between the calculated values of both models and the collected experimental data. The figure shows that stress space and strain space are separated by constitutive equations. To examine a model in the opposite space in which it was created, the results must first pass through the constitutive equations. Experimental testing, performed in strain control with stress and crack numbers recorded as responding variables, thus resides in both stress and strain space. It is important to recognize that errors may be introduced during the transition through the constitutive equations.

Figures 5.23-5.30 compare predictions of both models used in this study. Figures 5.23-5.26 are the same as Figures 5.8-5.11 with only the Case 3 shear lag prediction remaining and the Nuismer/Tan prediction added. The stress value of Nuismer/Tan that was used was the pre-fracture stress (the larger of the two calculated stresses, Fig. 5.21). In every case the shear lag and Nuismer/Tan predictions are similar and only the $[0_2/90_3]_S$ specimen predictions are noticeably distinct. It is interesting that the Nuismer/Tan results plotted in stress space are superior to the results when considered in strain space in which

they were created in (Figs. 5.12-5.15). This may result from the errors in both the stress analysis and the failure strain calculations mutually canceling. In particular, the response of the $[\pm 55/90_3]_S$ specimens is much better in stress space (Fig. 5.26) than strain space (Fig. 5.15).

Figures 5.27-5.30 are Figures 5.12-5.15 with the Case 3 shear lag prediction added. The failure strain calculated by the shear lag theory was transformed to strain value through the basic stress-strain relation (eq. 4.16). For the $[0_2/90_3]_S$ and $[\pm 20/90_3]_S$ specimens, the shear lag model is closer to the experimental data than both the pre- and post-fracture strain values calculated from the Nuismer/Tan theory. The shear lag theory provides very good predictions for these specimen geometries with the exception that the first ply failure strain may be too large. As the angle of constrain increases for specimens $[\pm 45/90_3]_S$ and $[\pm 55/90_3]_S$, the calculated first ply failure strain is closer to experimental results but the models overestimate the number of cracks at any given strain value. This effect originates in the incorrect stress-strain curve predictions that do not accurately represent the post-knee behaviour in the stress-strain curve for large constraining angles (Figs. 5.19-5.20).

FIGURES - CHAPTER 5

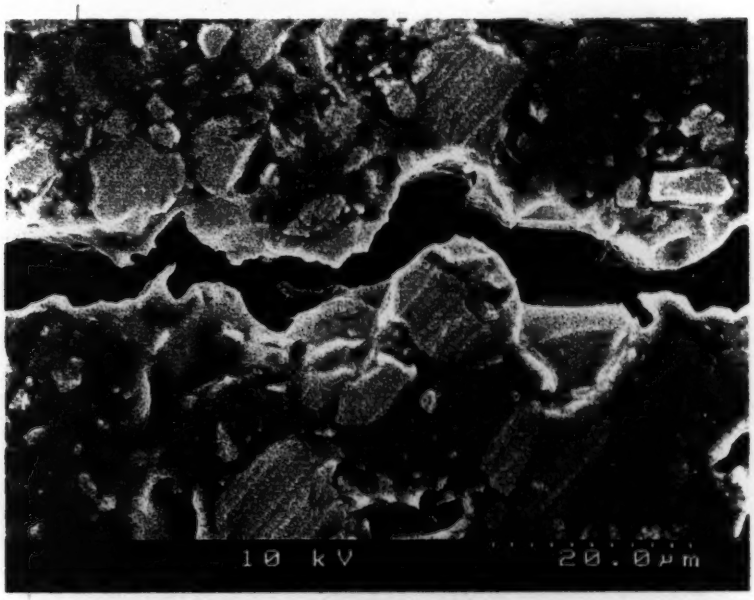

Figure 5.1 SEM image of a transverse matrix crack in composite laminate.

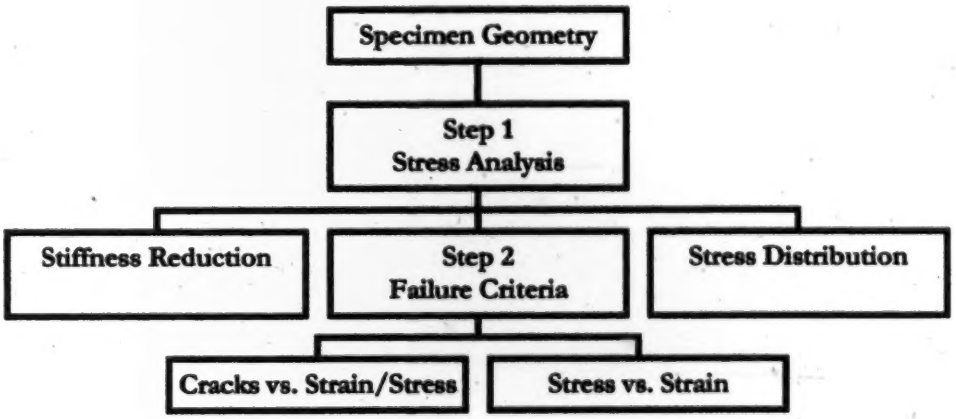

Figure 5.2 Steps involved in modelling progressive failure in composite laminates.

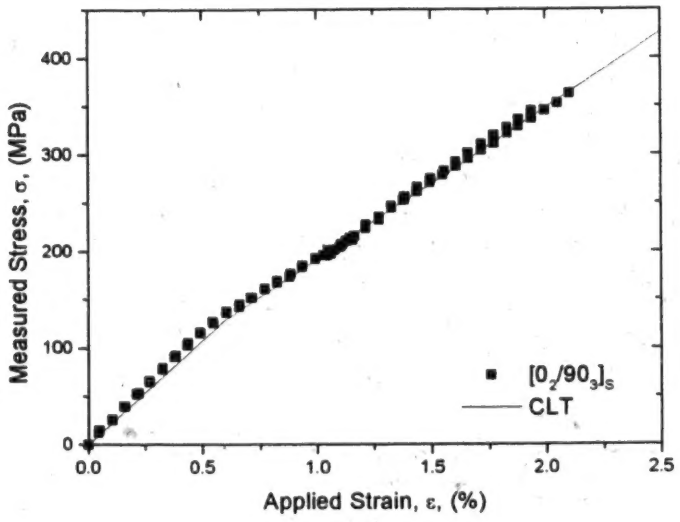

Figure 5.3 Classical laminate/ply discount theory prediction of $[0_2/90_3]_S$ stress-strain curve.

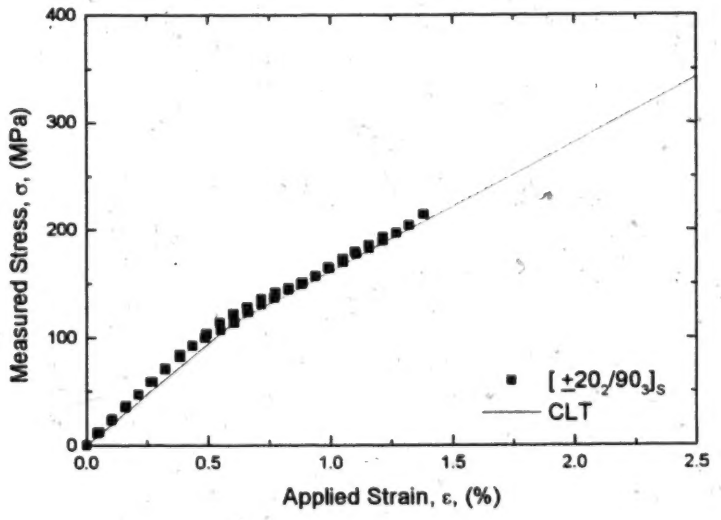

Figure 5.4 Classical laminate/ply discount theory prediction of $[\pm 20/90_3]_S$ stress-strain curve.

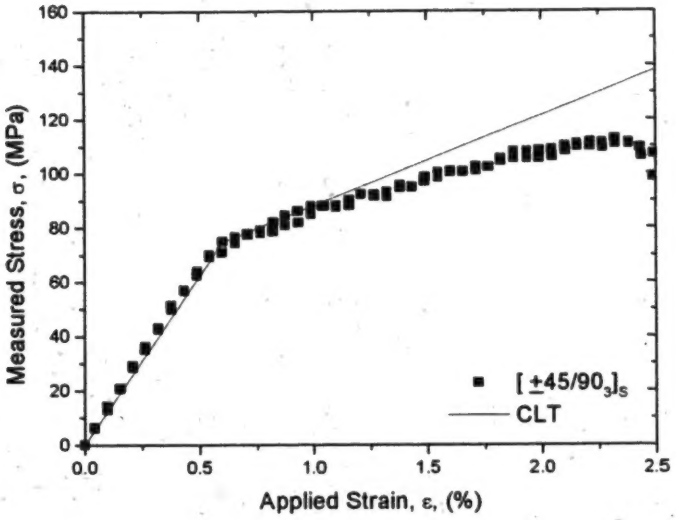

Figure 5.5 Classical laminate/ply discount theory prediction of $[\pm 45/90_3]_S$ stress-strain curve.

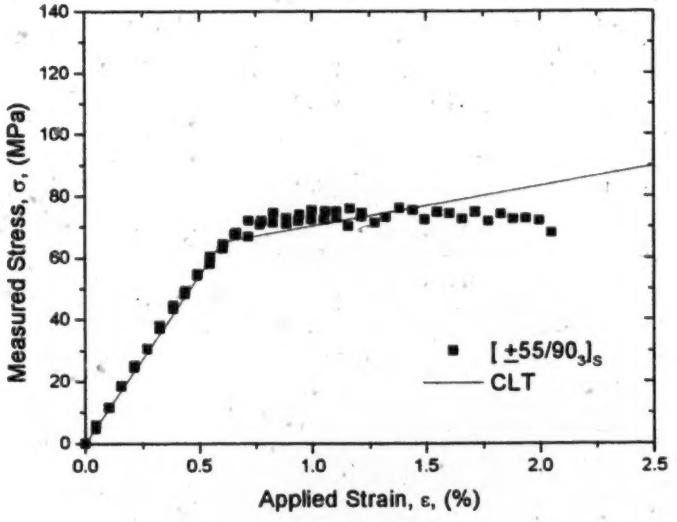

Figure 5.6 Classical laminate/ply discount theory prediction of $[\pm 55/90_3]_S$ stress-strain curve.

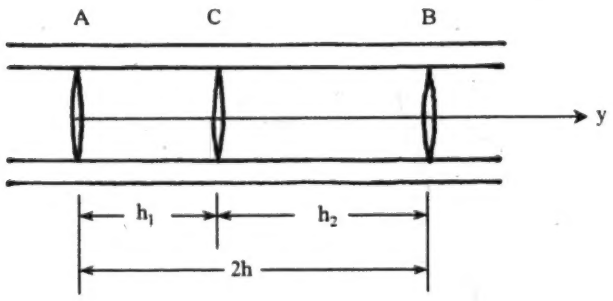

Figure 5.7 Two adjacent transverse cracks in the 90° plies (adapted from Laws and Dvorak [49]).

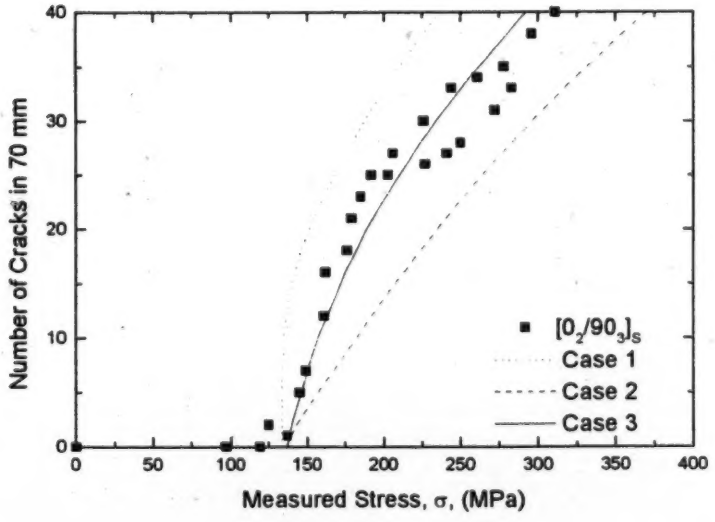

Figure 5.8 Accumulation of transverse cracks as a function of the applied stress in $[0_2/90_3]_S$ specimens showing shear lag prediction.

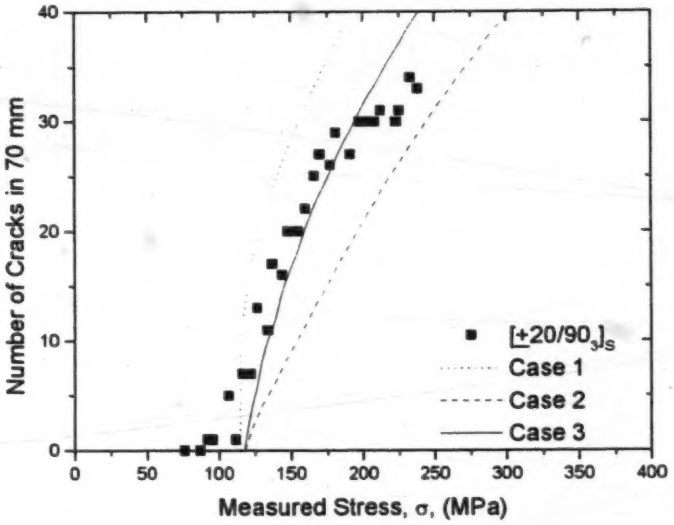

Figure 5.9 Accumulation of transverse cracks as a function of the applied stress in $[\pm 20/90_3]_S$ specimens showing shear lag prediction.

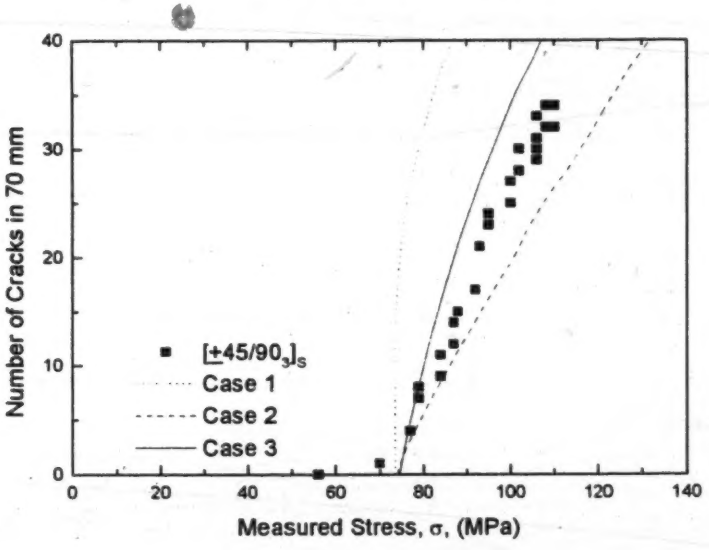

Figure 5.10 Accumulation of transverse cracks as a function of the applied stress in $[\pm 45/90_3]_S$ specimens showing shear lag prediction.

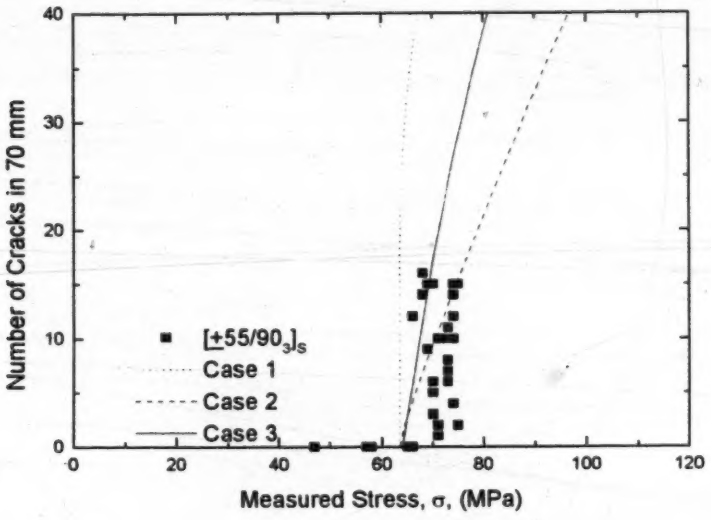

Figure 5.11 Accumulation of transverse cracks as a function of the applied stress in $[\pm 55/90_3]_S$ specimens showing shear lag prediction.

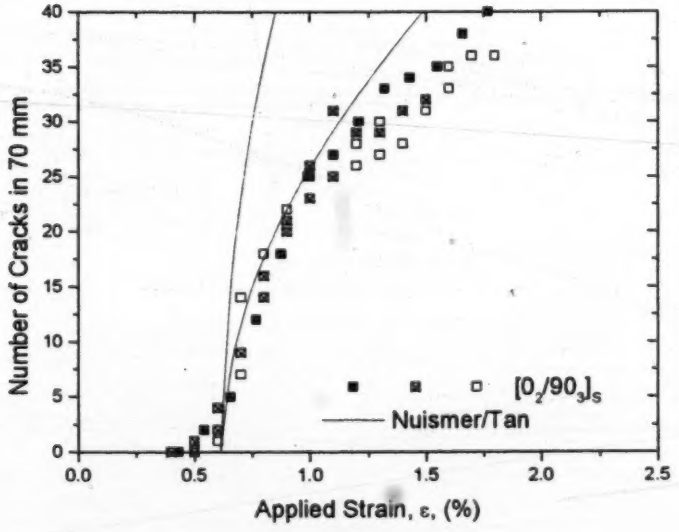

Figure 5.12 Accumulation of transverse cracks as a function of the applied strain in $[0_2/90_3]_S$ specimens showing Nuismer/Tan prediction.

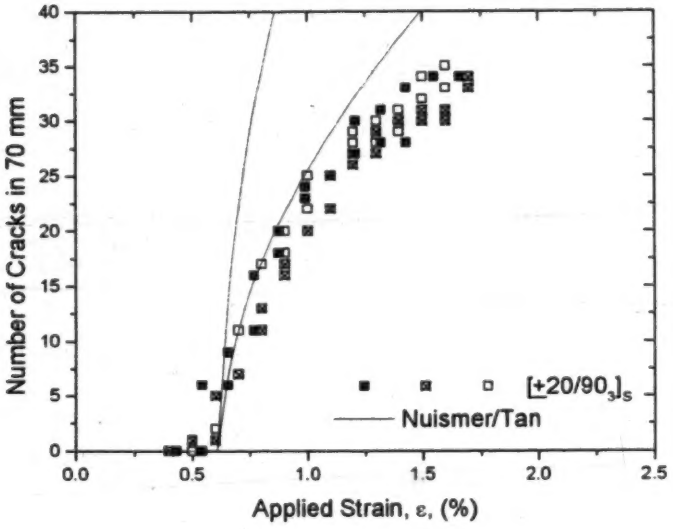

Figure 5.13 Accumulation of transverse cracks as a function of the applied strain in $[\pm 20/90_3]_S$ specimens showing Nuismer/Tan prediction.

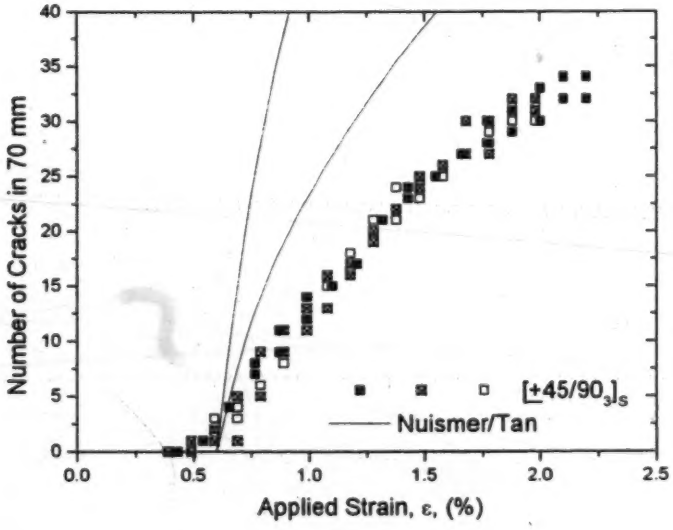

Figure 5.14 Accumulation of transverse cracks as a function of the applied strain in $[\pm 45/90_3]_S$ specimens showing Nuismer/Tan prediction.

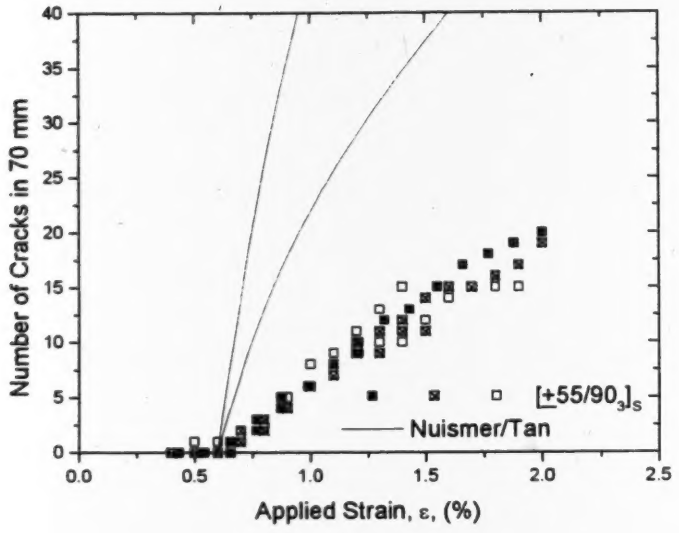

Figure 5.15 Accumulation of transverse cracks as a function of the applied strain in $[\pm 55/90_3]_S$ specimens showing Nuismer/Tan prediction.

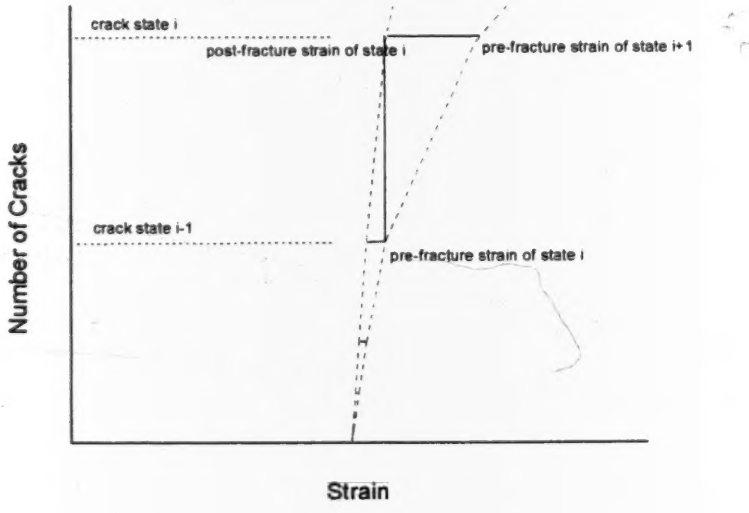

Figure 5.16 Schematic of Nuismer/Tan method to predict crack progression.

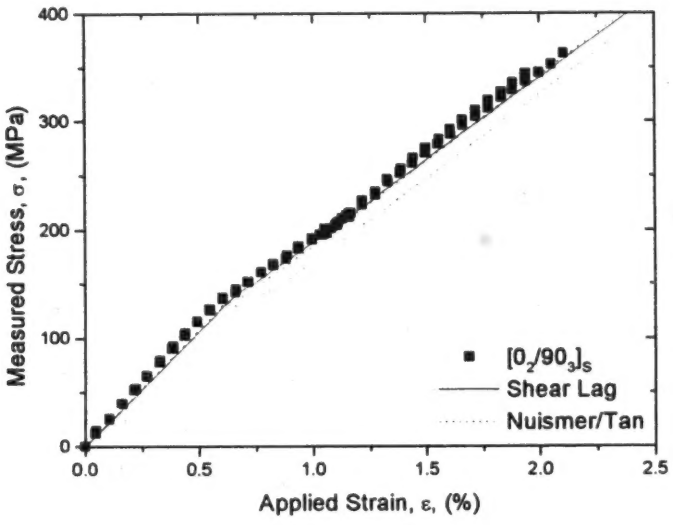

Figure 5.17 Stress-strain curve of $[0_2/90_3]_S$ specimens showing shear lag and Nuismer/Tan prediction.

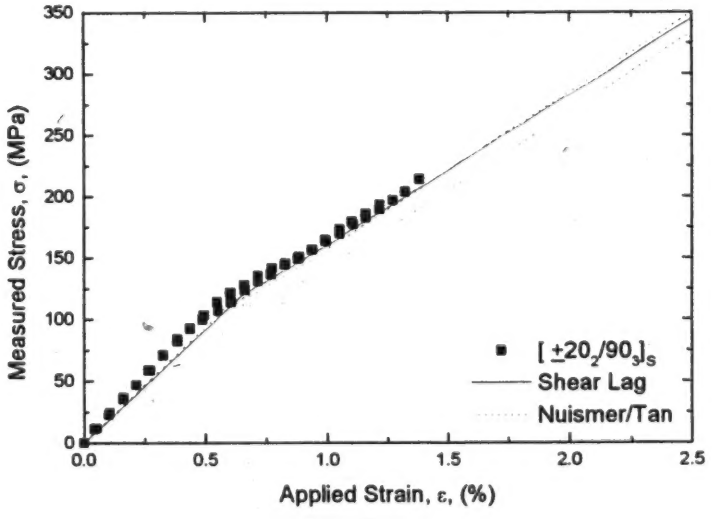

Figure 5.18 Stress-strain curve of $[\pm 20/90_3]_S$ specimens showing shear lag and Nuismer/Tan prediction.

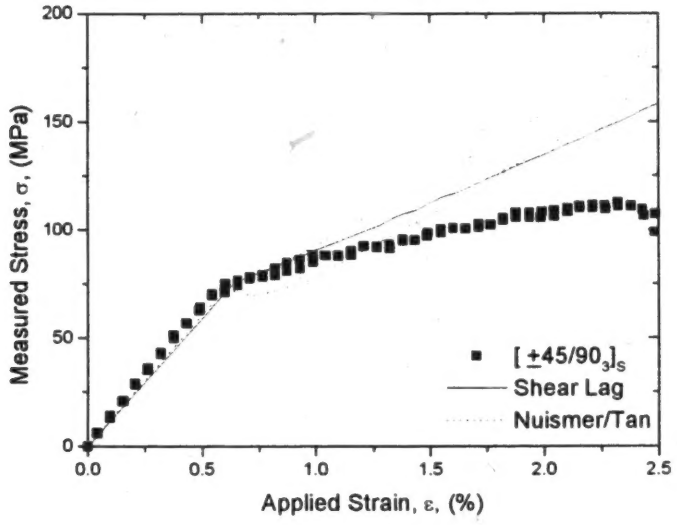

Figure 5.19 Stress-strain curve of $[\pm 45/90_3]_S$ specimens showing shear lag and Nuismer/Tan prediction.

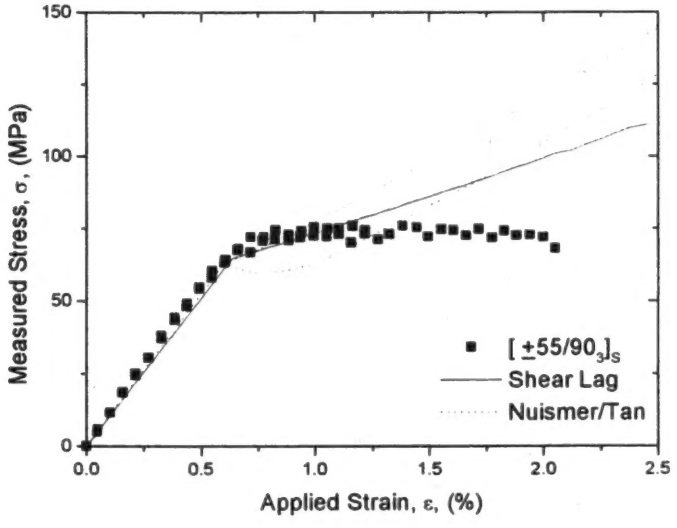

Figure 5.20 Stress-strain curve of $[\pm 55/90_3]_S$ specimens showing shear lag and Nuismer/Tan prediction.

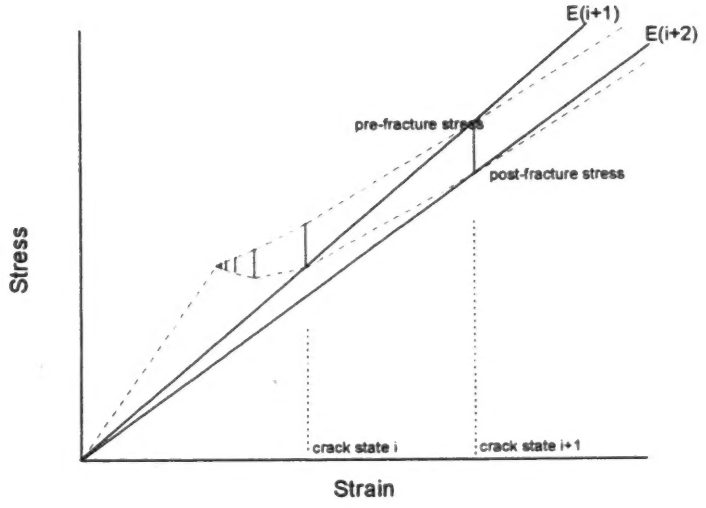

Figure 5.21 Schematic of Nuismer/Tan method to predict stress-strain curves.

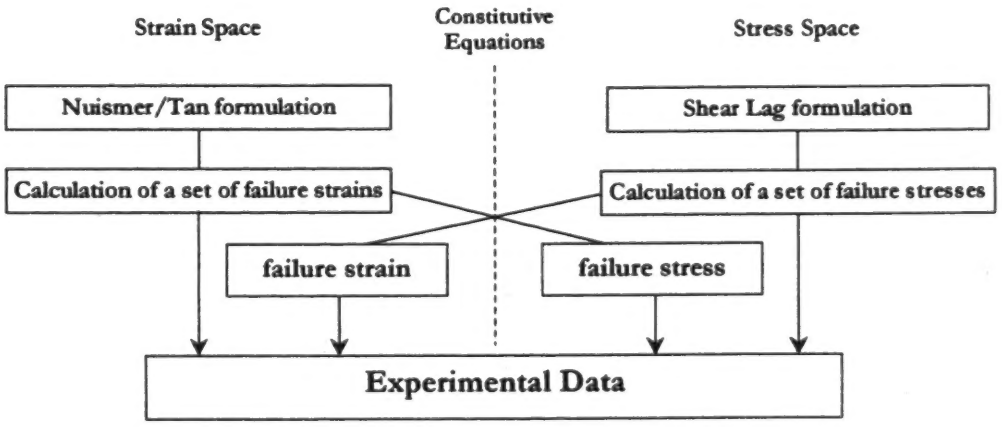

Figure 5.22 Schematic showing the experimental data and theoretical model regimes.

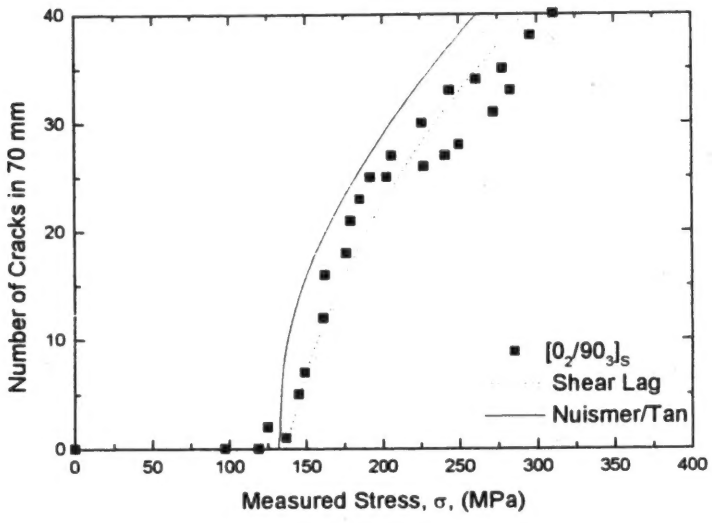

Figure 5.23 Accumulation of transverse cracks as a function of the applied stress in $[0_2/90_3]_S$ specimens showing Case 3 shear lag and Nuismer/Tan prediction.

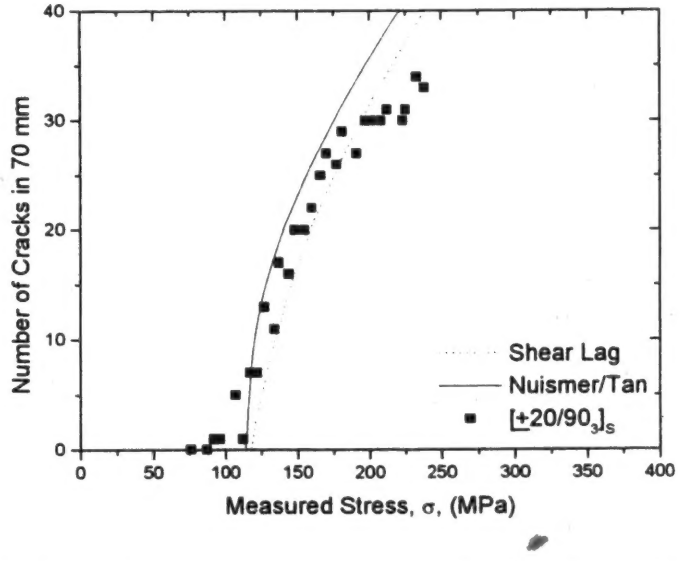

Figure 5.24 Accumulation of transverse cracks as a function of the applied stress in $[\pm 20/90_3]_S$ specimens showing Case 3 shear lag and Nuismer/Tan prediction.

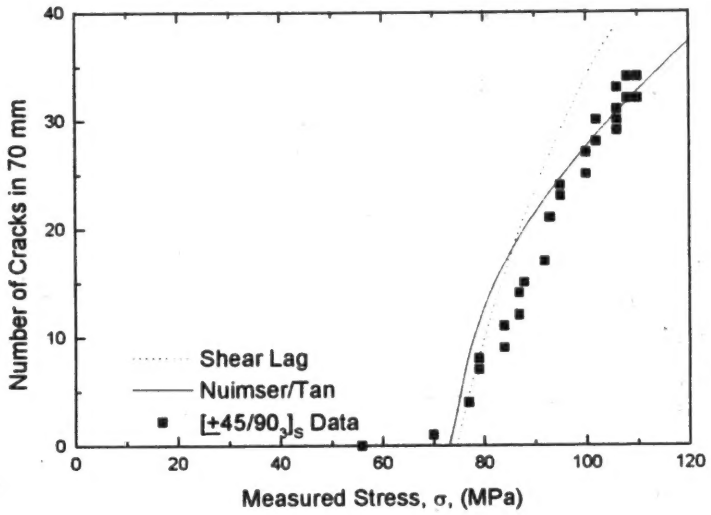

Figure 5.25 Accumulation of transverse cracks as a function of the applied stress in $[\pm 45/90_3]_S$ specimens showing Case 3 shear lag and Nuismer/Tan prediction.

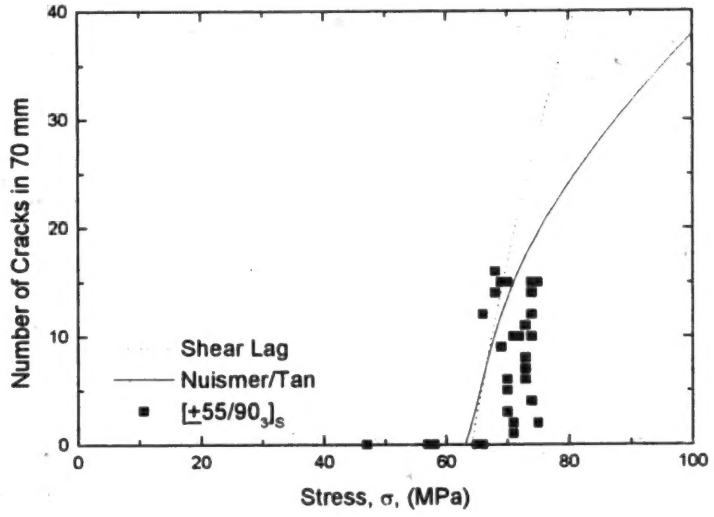

Figure 5.26 Accumulation of transverse cracks as a function of the applied stress in $[\pm 55/90_3]_S$ specimens showing Case 3 shear lag and Nuismer/Tan prediction.

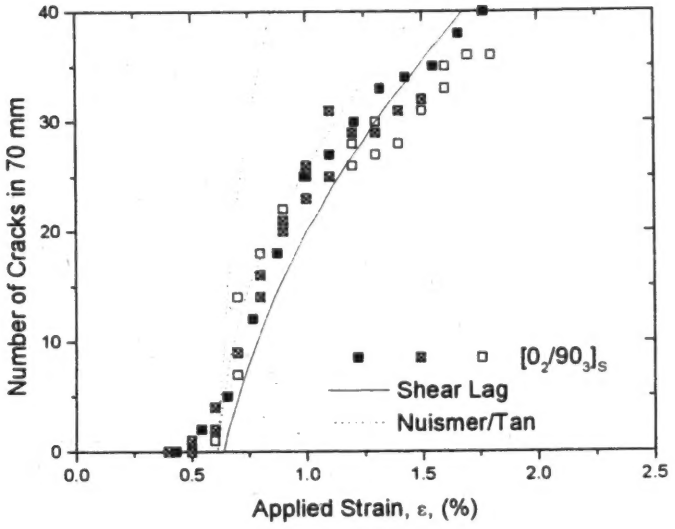

Figure 5.27 Accumulation of transverse cracks as a function of the applied strain in $[0_2/90_3]_S$ specimens showing Case 3 shear lag and Nuismer/Tan prediction.

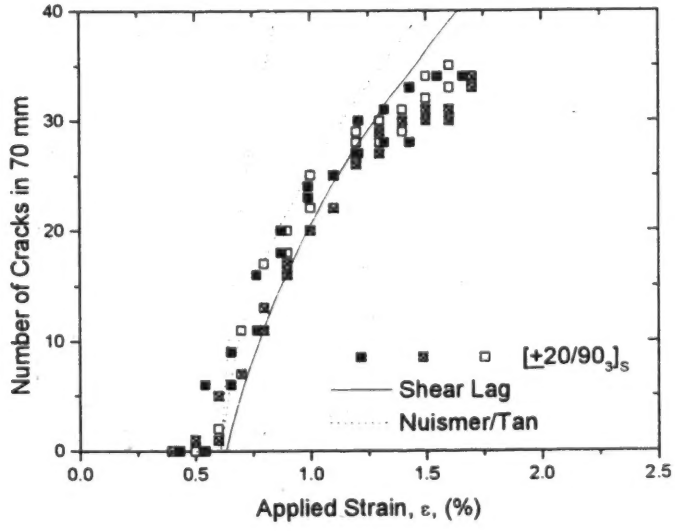

Figure 5.28 Accumulation of transverse cracks as a function of the applied strain in $[\pm 20/90_3]_S$ specimens showing Case 3 shear lag and Nuismer/Tan prediction.

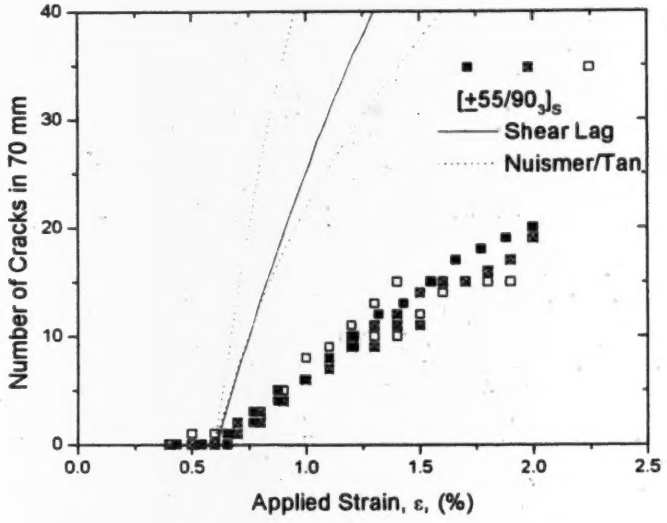

Figure 5.29 Accumulation of transverse cracks as a function of the applied strain in $[\pm 45/90_3]_S$ specimens showing Case 3 shear lag and Nuismer/Tan prediction.

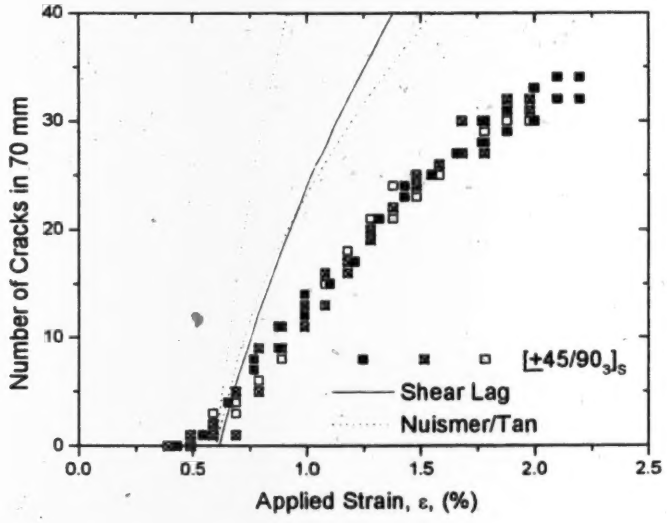

Figure 5.30 Accumulation of transverse cracks as a function of the applied strain in $[\pm 55/90_3]_S$ specimens showing Case 3 shear lag and Nuismer/Tan prediction.

6. SUMMARY AND CONCLUSIONS

Failure of composite materials is complex and much more difficult than homogeneous material failures. This study focussed on the stress analysis of cracked composite laminates and the implementation of a failure criterion to define design failure based on matrix cracking.

6.1 SPECIMEN FABRICATION AND MEASUREMENT OF ENGINEERING PROPERTIES

Detailed descriptions of the composite material, curing procedure, and specimen machining techniques were included to fully describe the material fabrication process. Significant effort was invested to develop a process that produced high quality specimens with minimal experimental variation.

The material used to fabricate all specimens in this study was 3M Scotchply Type 1003 continuous E-glass prepreg. Tensile loading, shear modulus and fracture energy experiments were carried out on this material. Coupon specimens of the type $[\pm\theta/90_3]_S$ were created to study progressive transverse cracking during tensile loading. $[90_{12}]_T$ specimens were fabricated into compact tension specimens that were tested to find the specific fracture energy of the composite material. $[(0/90)_4]_S$ and $[0_{90}]_T$ laminates were made into Iosipescu specimens and were tested to determine the in-plane and out-of-plane shear modulii.

A diamond blade saw was used to machine the specimens to the correct dimensions for each of the three specimen geometries listed above. The saw produced edges free from notches, fiber pullouts, and edge delaminations that have been shown to negatively affect material performance.

Residual stresses were calculated using Classical Laminate Theory. The results showed that the post-cure cooldown process produced residual hygrothermal tensile strains

in the matrix. These strains were a significant portion of the experimentally determined failure strains.

6.2 MECHANICAL RESPONSE AND STRESS-STRAIN PREDICTIONS

For the purpose of this study, 26 coupon specimens were tested: six $[\pm\theta/90_3]_S$ specimens with θ=0°, 20°, 45°, 55° and two $[\pm 70/90_3]_S$ specimens. Each $\pm\theta$ specimen set was tested for rate effects at three monotonic strain rates: 10^{-4}, 10^{-5}, and 10^{-6} s^{-1}. To overcome the limitations of existing observation techniques, a computer based crack detection system was developed. The system recorded the stress, strain and number of transverse cracks at any time in the loading process.

The dominant phenomenon observed in every laminate was a bilinear stress-strain curve. Transverse cracking caused this behaviour and began when the strain reached approximately 0.5%-0.6% (depending on the laminate geometry). The number of transverse cracks increased until ultimate specimen failure and no crack saturation density was observed. The presence of delaminations was noticed only immediately before failure (ε>1.5%). The ultimate failure strain ranged from 1.4% to 2.4%. The causes of this large range were grip failures and failure locations beyond the measurement range of the extensometer.

The stress-strain curve was linear until first ply failure at which point the stiffness dropped. This observation was important because it validated the theoretical approach linking stiffness reduction to transverse crack density. It was also justifies the use of Classical Laminate Theory to determine the residual thermal stresses because the residual strains were well within the elastic range

The orientation of the constraining plies was found to affect specimen behaviour. The maximum stiffness loss was 20% for the θ=0° specimens and 45% for the θ=45°. In addition, the effect of matrix cracks on the overall laminate behaviour is greater as the constraining ply angle increases. In the $[\pm 45/90_3]_S$ and $[\pm 55/90_3]_S$ specimens, substantial

crack damage occurred in the ±45° and ±55° plies. This observation explained why theoretical models, which assume linear elastic behaviour in the constraining plies, underestimated the stiffness loss and overestimated the number of cracks which appear at any given stress or strain.

Rate effects were negligible; even for the matrix dominated ±55° specimens the rate effect was barely discernable over the experimental scatter.

6.3 STRESS ANALYSIS OF CRACKED SYMMETRIC LAMINATES

A suitable stress analysis is the first step in modeling progressive failure. This study included a literature review that defines, explored and criticized the four main methods of stress analysis: interval variable, shear lag, approximate elasticity, and the variational method. The basic equations and derivations were discussed and model predictions of the stiffness reduction of cracked laminates were calculated to compare with experimental data.

Classical Laminate Theory (CLT) and damage mechanics were the internal variable methods discussed. CLT transforms thousands of fibers dispersed in each ply into a flat homogeneous ply with orthotropic properties. Issues such as matrix cracking are impossible to discuss once this has been done. The ply discount method can be used to provide a stress-strain curve prediction but the physics involved in the process are not considered rendering this approach ineffective.

The Talreja damage mechanics approach was developed and shown to be limited to a linear stiffness reduction prediction. Four elastic stiffness parameters remain undefined after the derivation and the linear stiffness reduction must be fit manually.

The shear lag approach was formulated by determining the stress and strain distributions from the associated displacements. The shear lag parameter was found from an independent first ply failure stress calculation. The shear lag approach is the simplest approach to predict a nonlinear stiffness reduction.

The approximate elasticity approach proposed by Nuismer/Tan was preformed using only the fundamental, independently measurable, material constants. This model predicted first ply failure stress (these predictions were used to fully define the shear lag approach). The approach combined approximate elasticity and fracture mechanics and the derivations resulted in a description of stiffness as a function of crack density.

Stiffness reduction predictions of all four models above were compared to experiments. The CLT and ply discount predictions were poor and the Talreja predictions fit only the crossply data. The shear lag and Nuismer/Tan predictions were more accurate, modeling the crossply specimens very well. Both of these models underestimated the stiffness reduction of the $[\pm 45/90_3]_S$ specimens. This resulted from constraint ply cracking that was not accounted for in either of the models.

Variational methods were included in the literature review but were not developed further. An in-depth discussion of this topic is beyond the scope of this study.

6.4 PROGRESSIVE DAMAGE AND THE IMPLEMENTATION OF A FAILURE CRITERION

Intrinsic to each design is the knowledge, or assumption, of the crucial failure mechanisms. The goal of this study was to establish a design criterion to define functional failure for high-pressure containment. $[\pm\theta/90_3]_S$ specimens were loaded to develop multiple transverse cracks and two distinct failure criteria were evaluated to determine which possessed superior predictive ability and physical rigour.

Strength of material failure criteria (failure stresses, strains, or stiffnesses) were discussed and the first ply failure strain of the experimental data was calculated. The results showed that there was a constraint effect that altered the first ply failure strain between specimens. This finding agreed with previous work of other researchers. CLT with ply discount theory was used with the erroneous first ply failure strain to reproduce stress-strain

curves. The predictions were surprisingly good for $[0_2/90_3]_S$ and $[\pm 20/90_3]_S$ specimens but poor for the $[\pm 45/90_3]_S$ and $[\pm 55/90_3]_S$ specimens. The major drawback of this technique was that the knee-point could not be found without the aid of the experimentally determined stress-strain curve.

Fracture mechanics was the superior of the two failure criteria studied because it is based on physical thermodynamic principles that account for thickness and constraint effects. A Griffin failure criterion for brittle materials was used to relate crack development to available elastic strain energy.

The shear lag approach used the energy based failure criterion to find the stress required to create a crack as a function of crack spacing and energy release rate. Three possibilities were proposed for the location of new cracks and Case 3, in which the location of the crack was proportional to the stress in the transverse ply, produced the best results. The first ply failure strain required to determine the shear lag parameter was borrowed from the approximate elasticity theory of Nuismer/Tan. This allowed the shear lag approach to become fully defined and substantially improved the method presented in the original paper which relied on experimental first ply failure stresses to complete the analysis. Overall, the shear lag approach produced acceptable progressive damage results.

The Nuismer/Tan approach related the specific fracture energy to the stored elastic strain energy of a unit cell before and after fracture. The first ply failure strains calculated differed from experimental results by 15%. The cause of these errors could not be determined. The model did not provide adequate prediction of the progressive cracking behaviour. In every case, the first ply failure strain and the accumulated number of cracks at any strain value were too large. The Nuismer/Tan model was shown to have poor resolution as the number of cracks grew beyond 1 crack/cm. It was argued that the average stress postulated by the authors in the original reference disguised the limitations and actual mechanisms of the model.

Predicting the stress-strain curve combined the stress analysis with the failure criterion. Both the shear lag and Nuismer/Tan predictions were accurate for the $[0_2/90_3]_S$ and $[\pm 20/90_3]_S$ specimens. As the angle of the constraining plies increased, the post-knee prediction over-estimated the remaining stiffness due to the omission of nonlinear constraining ply effect in the theoretical models.

6.5 CONCLUSIONS

This study concluded that:

1. High quality specimens were created from a composite prepreg. Very little scatter was observed between identical laminate geometries due to the carefully controlled specimen fabrication process. A 'knee-point' was the salient experimental feature of the stress-strain curve. No saturation crack density was observed and crack density increased until catastrophic specimen failure.

2. In conjunction with this thesis project, Dr. J.D. Wolodko developed an automated method to record the appearance of cracks. The automated procedure allowed the stress, strain and crack density to be correlated very closely. This data was previously unavailable in published literature and is crucial in recording experimental data.

3. Suitable stress analyses were completed using both approximate elasticity and the shear lag approach. The analyses were acceptable for $[0_2/90_3]_S$ and $[\pm 20/90_3]_S$ specimens and correctly predicted the stiffness loss of these specimens. For the $[\pm 45/90_3]_S$ and $[\pm 55/90_3]_S$ specimens, the stress analyses were incorrect because constraint ply cracking was not accounted for.

4. Fracture mechanics criteria were preferred over strength of materials failure criteria.

5. An amalgamation of a shear lag approach (developed by Laws and Dvorak) and an approximate elasticity approach (developed by Nuismer and Tan) was formulated in this thesis project. This 'modified shear lag' fully defined the shear lag parameter and shear lag approach in terms of engineering constants. This approach produced the best predictions for the stress-strain and crack accumulation curves of the four methods studied.

7. BIBLIOGRAPHY

[1] Juvinall, R.C. and Marshek, K.M., Fundamentals of Machine Component Design, 2nd Edition, John Wiley and Sons, New York (1991).

[2] "Advanced Composites for Aerospace Applications", Report No. 86-6, Chem Systems Inc., Tarrytown NY (October 1987).

[3] Erki, M.-A. and Rizkalla, S.H., "FRP products", Advances Composite Materials in Bridges and Structures in Japan Task-Force Report. Eds. A.A. Mufti, M.-A. Erki and L.G. Jaeger, Canadian Society for Civil Engineering, Montreal, 35-57 (August 1992).

[4] Head, P.R. "Design methods and bridge forms for the cost effective use of advanced composites in bridges," In proceedings of *Advanced Composite Materials in Bridges and Structures, 1st International Conference*, Eds. K.W. Neale and P. Labossiere, The Canadian Society for Civil Engineering, Montreal, 15-30, (1992).

[5] Candelas, R., Rubio, A., and Hernando, J. "Design of an automotive body panel manufactured by resin transfer moulding," In *Proceedings of the 9th International Conference on Composite Materials (ICCM/9)*, Ed. A. Miravete, Woodhead Publishing, Cambridge, **6**, 260-267 (1993).

[6] Vennett, R., Williams, J.G., Lo, K.-H. and Ganguly, P., "Economic benefits of using composites for offshore development and operations," In *Proceedings of 2nd International Conference on Composite Materials for Offshore Operations (CEAC CMOO-2)*, Ed. S.S. Wang, University of Houston (1997).

[7] Wolodko, J.D. "Biaxial fatigue and leakage characteristics of fiber reinforced composite tubes," Ph.D. Thesis, University of Alberta (1999).

[8] Hahn, H.T. and Tsai, S.W., "On the behavior of composite laminates after initial failures," *Journal of Composite Materials*, **8**, 288-305 (1974).

[9] Chou, S.-C., Orringer, O. and Rainey, J.H., "Post-failure behavior of laminates I - no stress concentration," *Journal of Composite Materials*, **10**, 371-381 (1976).

[10] Garrett, K.W. and Bailey, J.E. "Multiple transverse fracture in 90° cross-ply laminates of a glass fibre-reinforced polyester," *Journal of Materials Science*, **12**, 157-168 (1977).

[11] Garrett, K.W. and Bailey, J.E. "The effect of resin failure strain on the tensile properties of glass fibre-reinforced polyester cross-ply laminates," *Journal of Materials Science*, **12**, 2189-2194 (1977).

[12] Parvizi, A., Garrett, K.W. and Bailey, J.E. "Constrained cracking in glass fiber-reinforced epoxy cross-ply laminates," *Journal of Materials Science*, **13**, 195-201 (1978).

[13] Parvizi, A., and Bailey, J.E. "On multiple transverse cracking in glass fibre epoxy cross-ply laminates," *Journal of Materials Science*, **13**, 2131-2136, (1978).

[14] Bailey, J.E. and Parvizi, A., "On fibre debonding effect and the mechanism of transverse-ply failure in cross-ply laminates of glass fibre/thermoset composites" *Journal of Materials Science*, **16**, 649-659, (1981).

[15] Scotchply Type 1003 Continuous E-glass Reinforced Plastic Material Data Sheet, 3M Corporation

[16] Parhizgar, Z. and Sun C.T., "Application of the principles of linear fracture mechanics to composite materials", *International Journal of Fracture*, **20**, 3-15 (1982).

[17] Manders, P. W., Chou, T.-W., Jones, F.R. and Rock, J.W., "Statistical analysis of multiple fracture in 0/90/0 glass fibre/epoxy resin laminates," *Journal of Materials Science*, **18**, 2876-2889 (1983).

[18] Hwang, W. and Han, S.W., "Statistical study of strength and fatigue life of composite materials," *Composites*, **18** (1), 47-53 (1987).

[19] Highsmith, A.L., and Reifsnider, K.L., "Stiffness reduction mechanisms in composite laminates," In *Damage in Composite Materials*, ASTM STP 775, Ed. K.L. Reifsnider, American Society for Testing and Materials, Philadelphia, PA, 103-177 (1982).

[20] Crocker, L.E., Ogin, S.L., Smith, P.A., and Hill, P.S., "Intra-laminar fracture in angle-ply laminates," *Composites Part A*, **28A**, 839-846 (1997).

[21] Hoover, J.W., Kujawski, D. and Ellyin, F. "Transverse cracking of symmetric and unsymmetric glass-fiber/epoxy resin laminates," *Composite Science and Technology*, **57**, 1513-1526 (1997).

[22] Ellyin, F. and Wolodko, J.D., "Testing facilities for multiaxial loading of tubular specimens," In *Multiaxial Fatigue and Deformations Testing Techniques*, ASTM STP 1280, Eds. S. Kalluri and P.J. Bonacuse, American Society for Testing and Materials, 7-24 (1997).

[23] Kitano, A., Yoshioka, K., Noguchi, K. and Matsui, J. "Edge finishing effects on transverse cracking of cross-ply CFRP laminates," In *Proceedings of the 9th International Conference on Composite Materials (ICCM/9)*, **5**, Ed. A. Miravete, Woodhead Publishing, Cambridge, 79-86 (1993).

[24] Boniface, L., Smith, P.A., Bader, M.G., and Rezaifard, A.H., "Transverse ply cracking in cross-ply CFRP laminates - initiation or propagation controlled?" *Journal of Composite Materials*, **31** (11), 1080-1112 (1997).
[25] Watson, J.C. and Raghupathi, N., "Glass fibers," In *Engineered Materials Handbook, Vol. 1, Composites*, Ed. Theodore J. Reinhart, ASM International, Metals Park, Ohio, 107 (1988).

[26] Anderson, T.L. Fracture Mechanics Fundamental and Applications, 2nd ed., 31-55, (1994)

[27] "ASTM standard test method for sear properties of composite materials by the v-notched beam method - D 5379/D 5379M-93", *Annual Book of ASTM Standards*, Vol. 08.01 (1993).

[28] Daniel, I.M. and Ishai, O., Engineering Mechanics of Composite Materials, Oxford University Press, New York (1994).

[29] Favre, J.-P., and Laizet, J.-C., "Amplitude and counts per event analysis of the acoustic emission generated by the transverse cracking of cross-ply CFRP," *Composites Science and Technology*, **36**, 27-43 (1989).

[30] Fine, A.S. and Springer, G.S., "Design of composite laminates for strength, weight and manufacturability," *Journal of Composite Materials*, **31** (23), 2331-2390 (1989).

[31] Shahid, I. and Chang, F.-K., "An accumulative damage model for tensile and shear failures of laminates composite plates," *Journal of Composite Materials*, **29** (7), 926-981 (1995).

[32] Renard, J., Favre, J.-P. and Jeggy, Th., "Influence of transverse cracking on ply behavior: introduction of a characteristic damage variable," *Composites Science and Technology*, **46**, 29-37 (1993).

[33] Fukunaga, H., Chou, T.-W., Peters, P.W.M. and Schulte, K., "Probabilistic failure strength analyses of graphite/epoxy laminates," *Journal of Composite Materials*, **18**, 339-356 (1984).

[34] Peters, P.W.M., "The strength distribution of 90° plies in 0/90/0 graphite-epoxy laminates," *Journal of Composite Materials*, **18**, 545-555 (1984).

[35] Peters, P.W.M. and Chou, T.-W., "On cross-ply cracking in glass and carbon fibre-reinforced epoxy laminates," *Composites*, **18** (1), 40-46 (1987).

[37] Nuismer, R.J. and Tan S.C., "Constitutive relations of a cracked composite lamina," *Journal of Composite Materials*, **22**, 306-321 (1988).

[38] Tan, S.C. and Nuismer, R.J., "A theory for progressive matrix cracking in composite laminates," *Journal of Composite Materials*, **23**, 1029-1049 (1989).

[39] Hart-Smith, L.J., "Some observations about test specimens and structural analysis for fibrous composites," *Composite Materials: Testing and Design (Ninth Volume), ASTM STP 1059*, Ed. S. P. Garbo, American Society for Testing and Materials, Philadelphia, 86-120 (1990).

[40] Hart-Smith, L.J., "A re-examination of the analysis of the in-plane matrix failure in fibrous composite laminates," *Composites Science and Technology*, **56**, 107-121 (1996).

[41] Crossman, F.W. and Wang, A.S.D., "The dependence of transverse cracking and delamination of ply thickness in graphite/epoxy laminates," *Damage in Composite Laminates, ASTM STP 775*, Ed. K.L. Reifsnider, American Society of Testing and Materials, 118-139 (1982).

[42] Flaggs, D.L. and Kural, M.H., "Experimental determination of the in situ transverse lamina strength in graphite/epoxy laminates," *Journal of Composite Materials*, **16**, 103-116 (1982).

[43] Moore, R.H. and Dillard, D.A., "Time-dependent matrix cracking in cross-ply laminates," *Composites Science and Technology*, **39**, 1-12 (1990).

[44] Talreja, R., "Transverse cracking and stiffness reduction in composite laminates," *Journal of Composite Materials*, **19**, 355-375 (1985).

[45] Talreja, R., "A continuum mechanics characterization of damage in composite materials," *Proceedings of the Royal Society of London*, **A 399**, 195-216 (1985).

[46] Talreja, R., "Damage development in composites: mechanisms and modelling," *Journal of Strain Analysis*, **24**, 215-222 (1989).

[47] Talreja, R., "Transverse cracking and stiffness reduction in cross ply laminates of different fracture toughness," *Journal of Composite Materials*, **26** (11), 1644-1663 (1992).

[48] Hashin, Z., "Analysis of cracked laminates: a variational approach," *Mechanics of Materials*, **4**, 121-135 (1985).

[49] Laws, N. and Dvorak, G.J., "Progressive transverse cracking in composite laminates," *Journal of Composite Materials*, **22**, 900-916 (1988).

[50] Zhang, J., Fan, J. and Soutis, C., "Analysis of multiple matrix cracking in $[\pm\theta_m/90_n]_s$ composite laminates. Part 1: In-plane stiffness properties," *Composites*, **23** (5), 291-298 (1992).

[51] Zhang, J., Fan, J. and Soutis, C., "Analysis of multiple matrix cracking in $[\pm\theta_m/90_n]_s$ composite laminates. Part 2: Development of transverse ply cracks," *Composites*, **23** (5), 299-304 (1992).

[52] Nairn, J.A., "The strain energy release rate of composite microcracking: a variational approach," *Journal of Composite Materials*, **23**, 1106-1129, (1989).

[53] Nairn, J.A. and Hu, S., "The initiation and growth of delaminations induced by matrix microcracks in laminated composites," *International Journal of Fracture*, **57**, 1-24 (1992).
[54] Liu, S. and Nairn, J.A., "The formation and propagation of matrix microcracks in cross-ply laminates during static loading," *Journal of Reinforced Plastics and Composites*, **11**, 158-178 (1992).

[55] Nairn, J.A., Hu, S. and Bark, J.S., "A critical evaluation of theories for predicting microcracking in composite laminates," *Journal of Materials Science*, **28**, 5099-5111 (1993).

[56] Varna, J. and Berglund, L.A., "Thermo-elastic properties of composite laminates with transverse cracks," *Journal of Composites Technology and Research*, **16** (1), 77-87 (1994).

[57] Varna, J., Berglund, L.A., and Bjomberg, H., "On the determination of transverse strain to failure in composites," In Proceedings of the *European Conference on Composite Testing and Standardization (ECCM-CTS)*, Ed. P.J. Hogg, K. Schulte and H. Wittich, Woodhead Publishing, Cambridge, 267-276 (1994).

[58] Varna, J. and Berglund, L., "Multiple transverse cracking and stiffness reduction in cross-ply laminates," *Journal of Composites Technology and Research*, **13** (2), 99-106 (1991).

[59] Varna, J. and Berglund, L.A., "A model for prediction of the transverse cracking strain in cross-ply laminates," *Journal of Reinforced Plastics and Composites*, **11**, 708-728 (1992).

[60] Motogi, S. and Fukuda, T., "Intralaminar fracture toughness of 90° layer in crossply composite laminates," *Materials Science Research International*, **2** (2), 111-116 (1996).

[61] Boresi, A.P., Schmidt, R.J., and Sidebottom, O.M. Advanced Mechanics of Materials, 5th ed., John Wiley and Sons Inc., New York (1993).

[62] Daniel, I.M. and Lee, J.-W., "Damage development in composite laminates under monotonic loading," *Journal of Composites Technology and Research, JCTRER*, **12** (2), 98-102 (1990).

APPENDIX

Shear Testing of Scotchply Type 1003 Prepreg Reinforced Plastic Performed with the Standard Test Method for Shear Properties of Composite Materials by the V-Notched Beam Method – ASTM Standard D 5379/D 5379M

The test method ASTM Standard D 5379/D 5379M [27] *was followed with two variations for Scotchply Type 1003 Prepreg Reinforced Plastic. Notches were prepared by precision grinding. The available grinding wheel prepared notches with a radius much smaller than specified. It was assumed that this small radius would not affect the measurement of the elastic modulus. Measurement of the shear modulus of the G_{12} specimens showed significant scatter which was reduced by changing the cord modulus domain from 0.1% - 0.3% strain to 0.2% - 0.4% strain.*

This appendix outlines the measurement of shear modulus of Scotchply Type 1003 Prepreg Reinforced Plastic. This material is a commercially available continuous fiber composite. The E-glass fiber diameter is 9 μm. The manufacturer does not provide the user with details regarding the sizing and matrix characteristics.

The shear modulus values of interest were G_{12} and G_{23}. The G_{12} measurements were performed on $[(0/90)_4]_S$ specimens as suggested in the standard. The average thickness of the cross-ply specimens was 3.52 mm. The specimens were made from one plate. The fabrication of the G_{23} specimens was more difficult. In order to test the out-of-plane response of the material, a thick laminate was required and the available equipment would not allow for the laminate to be cocured to the final panel thickness of 20mm. Instead, the procedure suggested in 8.3.2.2 in the standard was used. Two $[0_{10}]$ plates were symmetrically bonded to a $[0]_{70}$ specimen using 3M Scotch-Weld DP-460 Epoxy Adhesive. In this way, a 20 mm thick panel was created with a test section of 14 mm.

The fiber volume fraction was calculated for both specimens using the burn-off method. The $[(0/90)_4]_S$ specimen was 53% fiber (average ply thickness 0.220 mm) and the $[0]_{90}$ specimen was 53% fiber (average ply thickness 0.222 mm).

The specimens were prepared in the Department of Mechanical Engineering material testing laboratory and machine shop. Specimens were rough cut from plates with a gravity-feed low speed cutting saw. Final dimensions were obtained by precision grinding except for the thicknesses of the G_{23} specimens which were machined by the gravity-feed saw. The notches were machined with a high-speed precision grinding wheel. The notch diameter was much smaller than the tolerance specified within the standard. Once the notches were cut, the specimens were labeled G_{12} and G_{23} 0 through 4 respectively.

Calibration of the testing machine was done before the start of testing using an internal calibration technique. The strain gauges were not calibrated.

An Instron screw-feed hydraulic load frame was used to apply force. A constant head-speed of 0.05 inch/min was applied to the upper grip with linear bearing of the v-notched beam test

Specimen	Thickness at notch, h, (mm)	Width across notch, w, (mm)	Height, H, (mm)	Area, A, (mm^2)
G_{12}-1	3.50	11.02	20.07	38.57
G_{12}-2	3.57	10.95	20.05	39.09
G_{12}-3	3.51	11.19	20.06	39.28
G_{12}-4	3.51	11.20	20.06	39.31
G_{12}-5	3.52	11.10	20.08	39.07
G_{23}-0	3.89	11.25	20.03	43.76
G_{23}-1	4.05	11.32	20.09	45.85
G_{23}-2	3.96	11.21	20.04	44.39
G_{23}-3	3.94	11.02	20.02	43.42
G_{23}-4	3.70	11.10	20.08	41.07

Table A.1: Specimen Dimensions

fixture. No twisting of the specimens were observed. The data was collected with a digital oscilloscope sampling at a rate of 5 samples/s.

The storage and testing conditions were ambient (21°C and 50% relative humidity).

Three specimens were tested for determination both the in and out-of-plane properties. The speed of testing was a crosshead velocity of 0.05 inch/min. The strain gauges were oriented in a stacked rosette between the notch roots.

One Measurements Group, Inc. CEA-06-062WT-350 strain gauges were fixed to the specimen with M-Bond 200 cyanoacrylate. The gauges had 350 Ohms nominal resistance, a gauge factor of 2.12, and measured 5 mm by 5 mm. The gauges were wired in a half-bridge configuration. No temperature compensation was used as the gauges possessed some self-compensation. Transverse sensitivity was assumed to be negligible and the lead-wires were short to limit lead-wire resistance.

2.0 Results

The shear cord modulus of elasticity suggested in 12.3.1 was followed to determine the shear modulii. The results are tabulated in Table A.2.

The mean values of the tests are G_{12}=4.51 GPa and G_{23}=4.17 GPa. The coefficients of variance are 19% and 5.8% respectively. The variance found in the G_{12} value is of concern and was thought to arise due to uncertainties in the load cell data. In order to reduce the effect of load cell uncertainty, the shear modulii shown below were calculated over the range of 0.2 - 0.4% strain (Table A.3). The mean is G_{12}=4.49 GPa with a coefficient of variance of 8.63%.

Specimen	Measured Shear Modulus, G, (GPa)	Failure mode and location	Comments
G_{12}-0	4.90	notch roots	test
G_{12}-1	5.35	notch roots	
G_{12}-2	4.15	notch roots	poor alignment
G_{12}-3	5.40	notch roots	
G_{12}-4	3.57	notch roots	
G_{23}-0	3.86	notch roots	
G_{23}-1	4.11	notch roots	
G_{23}-2	4.32	notch roots	
G_{23}-3	4.40	notch roots	

Table A.2: Results of the shear tests using 12.3.1 procedure.

Specimen	Measured Shear Modulus, G, (GPa)
G_{12}-0	4.53
G_{12}-1	4.78
G_{12}-2	4.85
G_{12}-3	4.88
G_{12}-4	3.93

Table A.3: Shear modulii of G_{12} specimens with modified cord calculation range of 0.2% - 0.4% strain.

3.0 Figures

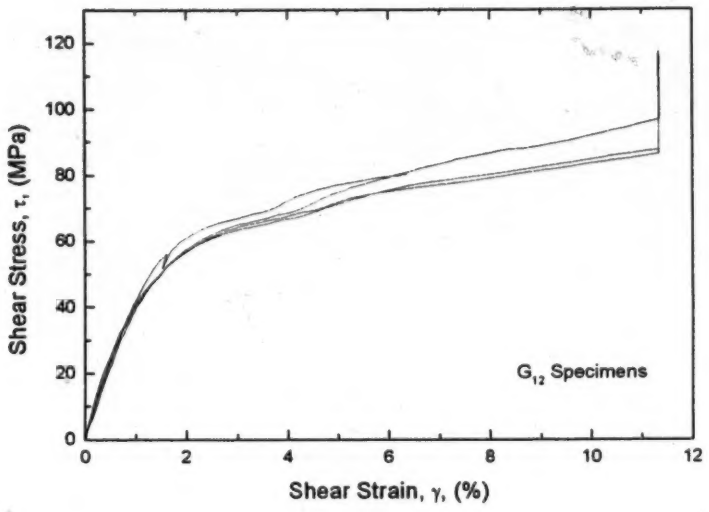

Figure A.1: Shear stress vs. shear strain for G_{12} specimens.

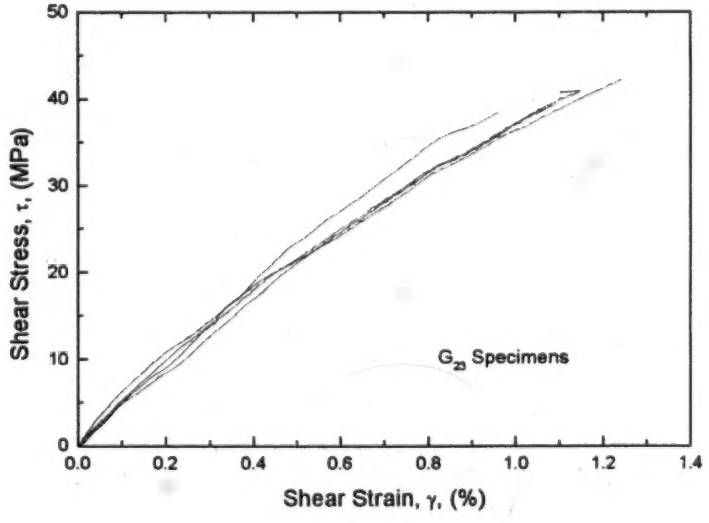

Figure A.2: Shear stress vs. shear strain for G_{12} specimens.

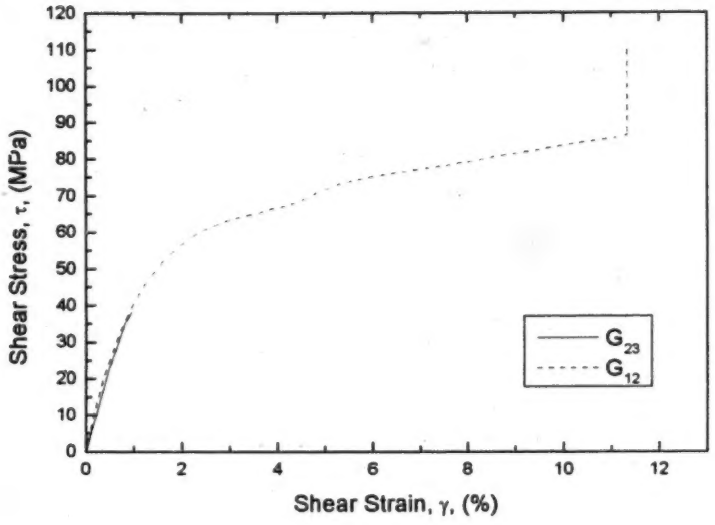

Figure A.3: Comparing shear stress vs. shear strain for G_{12} and G_{23} specimens.

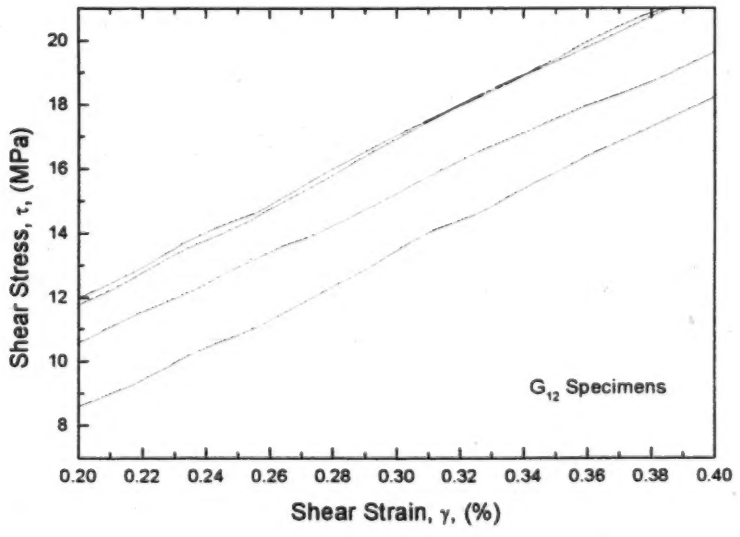

Figure A.4: Revised cord modulus domain for G_{12} specimens.